UNIVERSIDADE DE LISBOA

FACULDADE DE CIÊNCIAS

DEPARTAMENTO DE FÍSICA

Development of a cryogenic facility for the generation of space debris

Tiago David Serrano Frederico

Mestrado Integrado em Engenharia Física

Dissertação orientada por:
Professor Doutor António Amorim
Doutor Paulo Gordo

2017

UNIVERSIDADE DE LISBOA
FACULDADE DE CIÊNCIAS
DEPARTAMENTO DE FÍSICA

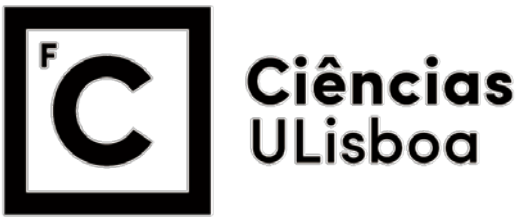

Development of a cryogenic facility for the generation of space debris

Tiago David Serrano Frederico

Mestrado Integrado em Engenharia Física

Dissertação orientada por:
Professor Doutor António Amorim
Doutor Paulo Gordo

2017

Abstract

Engineers, together with scientists, have developed advanced materials for spacecraft and satellites for a range of applications in space exploration, transportation, global positioning and communication. The materials used on the exterior of a spacecraft are subjected to many environmental threats, that can degrade many materials and components. These threats include vacuum, solar ultraviolet radiation, charged particle radiation, plasma, surface charging and arcing, temperature extremes, thermal cycling, impacts from micrometeoroids and orbital debris. To determine the impacts of a long-term exposure to space conditions, tests can be performed in space or on the ground. Since the synergy of all the elements of the space environment is difficult to duplicate on the ground, ground facilities often do not accurately simulate the combined environmental effects.

The work described in this document is part of an ESA project, denominated “Space Debris from Spacecraft Degradation Products”. The main purpose of this activity is the assessment of the amount and characteristics of space debris objects resulting from spacecraft surface degradation. The results will be used as input for future space debris population models and for the selection of materials in the context of debris mitigation measure.

The work here described is part of a system capable of expose, in synergy, Vacuum Ultra Violet and thermal cycling under vacuum. In this document, the emphasis is placed on the description of all stages of the thermal and vacuum subsystems as well as the validation and deployment of the entire system.

Keywords: Space Debris, Material Cooldown, Thermal Cycles and Space Vacuum.

Resumo

As observações óticas e de radar a partir do solo, bem como a análise de hardware recuperado, apresentaram uma quantidade considerável de detritos espaciais que parecem resultar da degradação das superfícies externas de satélites e naves espaciais. O hardware recolhido mostrou que quer as MLI, quer as tintas, podem sofrer degradação extrema quando expostas ao ambiente espacial criando um grande número de resíduos. Não existe uma descrição quantitativa do número e da distribuição de tamanhos desses objetos.

Os materiais que revestem o exterior dos satélites/naves degradam-se quando, ao longo do tempo, são expostos ao rigoroso ambiente do espaço. As principais ameaças são a radiação de partículas carregadas, a radiação ultravioleta, o oxigénio atômico para órbitas baixas, as temperaturas extremas e os ciclos térmicos, os impactos de micrometeoritos e outros detritos. O impacto relativo destas ameaças individuais depende do tipo de missão a realizar, da sua duração, dos ciclos e eventos solares e da órbita em que a nave será colocada. No entanto, uma vez que tais produtos de degradação originam uma parte notável da população de detritos, é necessária mais informação para os modelos de migração de detritos espaciais, avaliações de risco de impacto e seleção de materiais para mitigar esses efeitos.

Para compreender a degradação dos materiais das naves espaciais, podem ser realizados estudos através de exposições espaciais e em laboratórios na Terra. A oportunidade de examinar os materiais que estiveram no espaço são raras - seja através de material recuperado, ou de experiências dedicadas a simular o ambiente espacial. As diferenças entre o ambiente de uma missão e o de uma experiência realizada em Terra necessitam de uma interpretação cuidadosa dos resultados devidos às diferentes sinergias. Estudos em laboratórios no solo permitem examinar os efeitos ambientais individuais ou em conjunto. Alguns testes de laboratório podem ser executados em tempo útil usando níveis de aceleração para alguns efeitos espaciais mas, devido às dificuldades na simulação exata desses efeitos, são necessárias calibrações complexas e uma interpretação cautelosa dos resultados.

O trabalho descrito neste documento faz parte de um projeto da ESA, denominado *"Space Debris from Spacecraft Degradation Products"*. O objetivo principal desta atividade é a avaliação da quantidade e da dimensão característica dos objetos resultantes da degradação da superfície da nave. Os resultados servirão como *inputs* para futuros modelos de população de detritos espaciais e para a seleção de materiais no contexto das medidas de mitigação de detritos em órbita.

Durante a órbita, a nave espacial encontra-se no espaço – sendo, o mesmo, conhecido pelo rigor das suas condições ambientais. As temperaturas no lado exposto ao Sol do satélite podem subir até aos 100 ° C; no lado escuro, a temperatura desce abaixo de -100 ° C. Os ciclos térmicos e as condições de vácuo poderão ter um impacto relevante na vida útil da nave espacial, que pode permanecer em órbita entre dois a dez anos. Com o objetivo de medir a quantidade de detritos resultantes desta exposição é necessário um simulador de ambiente espacial.

O trabalho apresentado é parte de um sistema capaz de expor, em sinergia, VUV e ciclos térmicos em vácuo. Neste documento, todas as etapas do desenvolvimento do subsistema de ciclos térmicos em vácuo são descritas.

Foi dada especial atenção ao isolamento térmico do sistema, uma vez que opera com uma amplitude térmica de 260 ° C e com uma temperatura inferior a -120 ° C. Operar a baixas temperaturas envolve uma análise ainda mais cuidadosa dos materiais de forma a que as perdas de energia sejam mínimas.

Foi escolhida uma arquitetura que usa um cryocooler de hélio como bomba de calor, mecanismo que permite o arrefecimento da base, denominado *Mechanical Thermal Switch*. De modo a avaliar o período de arrefecimento usando esta arquitetura foi realizada uma simulação dinâmica.

Para realizar o sistema de controlo necessário de um ciclo térmico, foi desenvolvido um software de controlo baseado em LabView. Além de fornecer ao utilizador uma interface gráfica, reúne informações de vários sensores e executa o ciclo térmico de acordo com essas leituras.

Foram obtidos diversos desempenhos do sistema e, no final, foi necessária uma modificação da placa de base com a intenção de diminuir o tempo de arrefecimento para níveis mais aceitáveis. Embora a caracterização térmica do MLI seja abordada neste documento, não se pretende que seja analisado em detalhe, mas como parte das análises térmicas do sistema.

Palavras-chave: Detritos espaciais, Arrefecimento de materiais, Ciclos térmicos, Espaço e vácuo.

Table of Contents

Table of Figures

Table of Tables

Acronyms

AO	Atomic Oxygen
AF	Accelerated factor
COTS	Commercial off-the-shelf
EOS	Earth Observing Satellite
ESA	European Space Agency
GEO	Geosynchronous Earth Orbit
HTD	High Temperature Dwelling
IC	Integrated Circuit
LEO	Low Earth Orbit
LTD	Low Temperature Dwelling
MEO	Medium Earth Orbit
MLI	Multi-Layer Insulation
PEO	polar earth orbit
PSA	Pressure-Sensitive Adhesive
RSO	Resident Space Object
TVC	Thermal Vacuum Cycle
VUV	Vacuum UV (115-180nm)

1. Introduction

Optical and radar observations from the ground and the analysis of retrieved hardware, either from maintenance missions on the Hubble Space Telescope or from dedicated missions have shown an abundance of space debris objects, that seem to result from the degradation of outer spacecraft surfaces. Retrieved hardware has shown that Multi-Layer Insulation foils, as well as paint, can severely degrade in space and create a larger number of pieces creating space debris. A quantitative description of the amount and size distribution of these debris objects is lacking.

Every material on the exterior of a spacecraft is exposed to the harsh space environment, which is the cause for degradation of materials. The main threats are the charged particle radiation, ultraviolet radiation, atomic oxygen for low orbits, extreme temperature and thermal cycling, impacts of micrometeoroids and debris. The relative impact of the individual threats depends on the type of mission to be performed, the mission duration, the solar cycles, solar events and the orbit in which the spacecraft will be placed. However, such degradation products could form a considerable part of the debris population and more information is required to develop reliable space debris flux models, compute the impact on risk assessments and for the selection of materials to mitigate these effects.

To better understand the degradation of spacecraft materials, studies can be performed through space-exposures and ground experiments. The opportunity to examine space flown materials, either through recovered material or through dedicated experiments are rare. Differences between the experiment environment and the intended mission environment and synergistic environmental effects requires a cautious interpretation of results. Ground laboratory studies can be used to examine individual environmental effects or a combination of these effects. Laboratory tests can be conducted in a timely manner using accelerated levels for some environmental effects, but due to the difficulties in properly simulate the space effects and complex calibrations, a cautious interpretation of the results is required.

The infrastructure described in this document was developed as part of an ESA project, denominated “Space Debris from Spacecraft Degradation Products”. The main purpose of this activity is the assessment of the amount and characteristics of space debris objects resulting from spacecraft surface degradation. The results are to be used as input for future space debris population models and for the selection of materials in the context of debris mitigation measure.

During the orbit, spacecraft are under space conditions, known for the harshness of several factors. The temperatures on the sunny side of the satellite can rise to nearly +100 °C. On the dark side, the temperature drops below -100 °C. The thermal cycling and the vacuum conditions may have a relevant impact on the lifetime of the spacecraft, which can be in orbit for a period comprised between two and up to ten years. A space environment simulator enables the measurement of the amount of debris resulted from space exposer.

The work here described is part of a system capable of expose, in synergy, Vacuum Ultra Violet and thermal cycling under vacuum. In this document are described all development stages of the thermal vacuum subsystem.

Special attention was given to the thermal isolation of the system, since it operates with a range of 260 °C and a bottommost at -120 °C. Operating at low temperatures involves a careful analysis of the materials to have minimal losses of power.

The cryogenic architecture uses a helium cryocooler as a heat pump and a mechanism that allows the cold part to be engaged and released from the base-plate, denominated Mechanical Thermal Switch. In order to evaluate the cooldown period to be achieved using this architecture, a dynamic simulation was performed.

In order to implement the control system needed to achieve a thermal cycling, a control software based on LabView was developed. Besides providing the user with a graphical interface, it gathers information from several sensors and executes the thermal cycling according to those readings.

As a result, it was possible to achieve several system performance levels. Furthermore, a modification of the original base-plate was required with the intent of decreasing the cooldown time to values within the target time range. Although, the characterization of the Multi-Layer Insulations is addressed in the report, it is not intended to be analysed in detail but to demonstrate the thermal analyses of the system.

2. Motivation and space environment

This chapter intends to provide a contextualization on the system present later in the document. A description of space environments that have impact in spacecraft exterior is presented.

The main goal of the ESA project is to assess the characteristics and the amount of space debris objects created during the exposure of a spacecraft exterior to its operational environment. The emphasis is on Multi-Layer Insulation (MLI) and paint flakes, which are both known as surface degradation products. It is important to understand the generation processes to be able to account for those space debris sources in environmental modelling. Therefore, experimental degradation studies shall be performed under realistic, or accelerated, space environment conditions.

The results of this study will also be used to improve the MASTER (Meteoroid and Space Debris Terrestrial Environment Reference), the European reference model for the space debris environment. The current release is MASTER-2009, which is soon to be replaced by an upgraded version with updated population files. [1]

2.1. Relevant Space Environment

Every material on the exterior of a spacecraft is exposed to the harsh environment of space, which is the cause for the degradation of materials. The main threats are charged particle radiation, ultraviolet radiation, atomic oxygen, extreme temperature and thermal cycling, impacts of micrometeoroids and debris. The relative impact of the individual threats depends on the type of mission to be performed, the mission duration, the solar cycles, solar events and the orbit in which the spacecraft will be placed at.

2.1.1. Orbit Definition

The relative impact of any of the space environment effects on materials depends on the type of mission the spacecraft must perform, e.g. communication, defence, Earth observation, and more important, the orbit in which the spacecraft is placed. Figure 2.1 shows the main factors of satellite surface degradation in the space environment as a function of orbit altitude. To establish the scale, please take in mind that the Earth radius is around 6370 km.

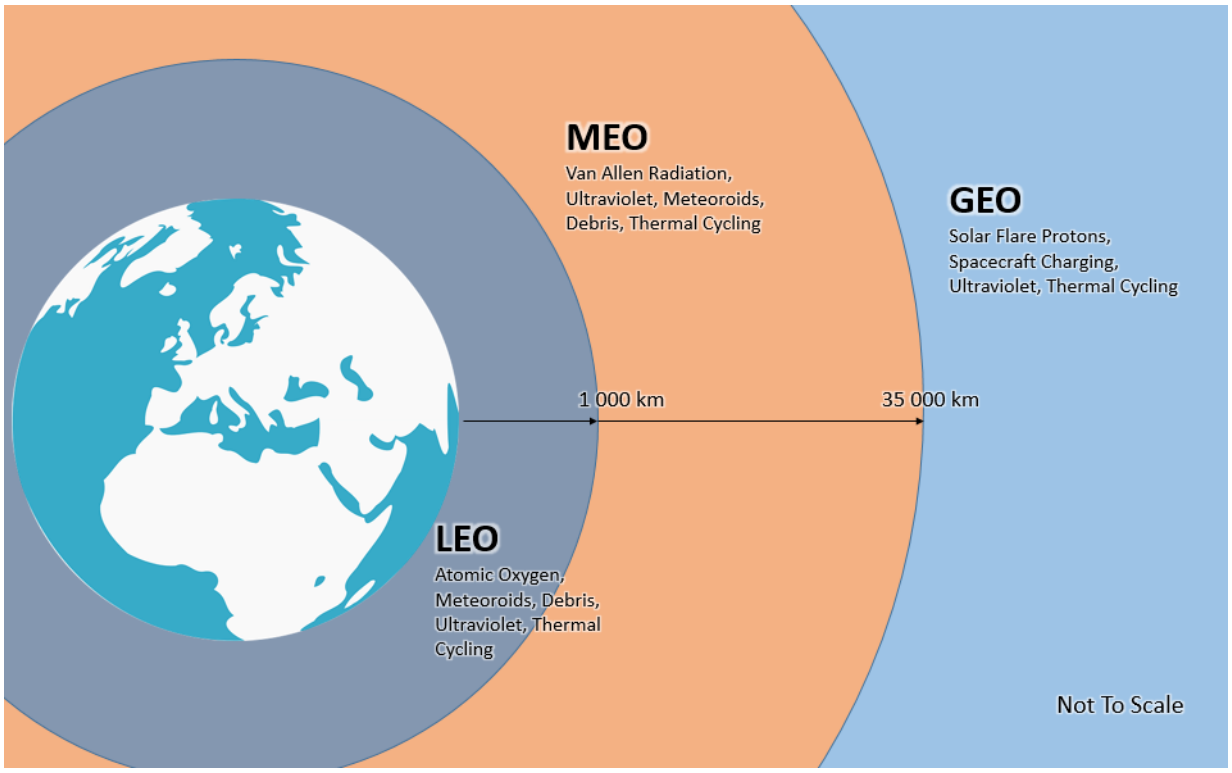

Figure 2.1 - Earth orbital definition

- Low Earth Orbit

LEO refers to orbits in the 100 to 1000km altitude range, which includes Earth-observing satellites (EOS). A particular case to be noted is the International Space Station (ISS) at about 400km. The radiation environment in LEO is rather benign, with a typical dose rate of around 0.1 krad/year. For a mission with a typical duration of 3 to 5 years the total dose is less than 0.5 krad. Most PEO (Polar Earth Orbit) are LEO with high inclinations (>55°) although more eccentric. The high inclination takes the orbit through the polar aurora regions, which can be rich in ion cosmic ray and solar flare particles. Higher radiation dose is accumulated during the passage through these regions; nevertheless, the transition time is typically small in comparison to a full orbit time. Thus, the dose rate is a few krad/year, similar to that in LEO.

A vehicle in LEO will receive radiant thermal energy from three primary sources: the incoming solar radiation (described by the solar constant), reflected solar energy (Earth albedo energy), and outgoing longwave radiation emitted by the Earth and atmosphere. The temperature range goes from -100°C to 100°C. A spacecraft in LEO moves in and out of eclipse once every orbit, as often as every 90 minutes.

- Medium Earth Orbit

The radiation environment in MEO - 1000 km to 35000 km altitude - is harsh since the satellite trajectories are confined, mostly, within the Van Allen radiation belts. Satellites are usually positioned in regions somewhat lower though, variable particle density may occur between the belts. The dose rate from both protons and electrons can be in the order of 100krad/year and it is highly variable due to strong solar cycle effects. Because of that MEO is only used if no other alternatives exist, e.g. GPS, GLONASS, Galileo constellations.

- Geosynchronous Earth Orbit

GEO is located at 35000km altitude in the high-energy plasma sheet. GEO satellites are exposed to the outer radiation belts, solar flares and cosmic rays [2,3].

2.1.2. Temperature

Temperature is a major parameter in the process of materials degradation when acting in synergy with other components of space environment, especially radiation. Regarding organic materials degradation increases with temperature due to the greater chain mobility (higher scission/x-linking ratio) [3]. In inorganic materials temperature governs annealing of coloured centres as observed in optics [4]. At low temperature, synergy with space radiation is not straightforward and depends on materials type: degradation mechanisms are “frozen” in materials sensitive at room temperature, while no significant change is observed in more resistant materials (epoxy, polyimide), silicones are more sensitive at low temperatures.

For missions with demanding temperature constraints (range and cycling), it was shown that the representative simulation of the mission profile was required to expect a reliable estimate materials degradation and prediction of End-of-Life performances [5].

A simple calculation allows to estimate the temperature of a surface facing the sun, with a 90° angle, of 115 °C. (Appendix A).

Moreover, at macroscopic level, temperature cycling alone or in synergy with space radiation induces mechanical stress that can result in enhanced overall degradation or at stress location [6,7].

2.1.3. Vacuum

The hard vacuum of space (10^{-6} to 10^{-9} mbar) will cause outgassing, which is the release of volatiles from materials. The outgassed molecules then deposit on line-of-sight surfaces and are more likely to deposit themselves on cold surfaces.

2.1.4. AO

Several forms (allotropes) of oxygen exist, while O_2 (molecular oxygen) being the most familiar since represents the breathable form on Earth. Ozone (O_3) and atomic oxygen (O_1, single atom, abbreviated AO), both occur in the upper atmosphere and pose distinct reactive allotropes. The atomic oxygen is very chemically active and it is the major atmospheric component in the low earth orbit [8,9]. The AO erodes most organic materials will react with many metals and other inorganic materials. The Atomic Oxygen only occurs on LEO.

2.1.5. VUV

Earth’s atmosphere filters out most of the sun’s damaging light, but outside this protection exterior spaceship materials bear the brunt of solar photon damage. The *Vacuum UV* (VUV) is the most damaging UV band in terms of material degradation and its wavelength is between 100 and 200 nm.

2.2. Materials and debris generations

A typical spacecraft has a payload, where the equipment for the primary mission is located and a bus or platform where the subsystems are installed. These subsystems typically include the Structures

subsystem, the Electrical power/distribution subsystem, the Telemetry, tracking, and command subsystem, the Attitude/velocity control subsystem, the Propulsion subsystem and the Thermal-control subsystem. On the Structures subsystem is assembled (among others) the external structure of the spacecraft [10,11]. The spacecraft external surface is mostly composed of either insulation blanket or radiator surface materials. Both are classified under the thermal control subsystem. As seen, for example, in Figure 2.2 or in any typical picture of a satellite, its surface looks golden in colour. The golden colour comes from the outer layer of the MultiLayer Insulation (MLI) blankets. The spacecraft exterior is mostly blanketed with MLI with cut-outs for radiator surfaces. The remaining radiator surfaces can be, for example, thermal (black body) radiators for temperature control, a second surface mirror or a more rigid blanket or tile attached to the spacecraft structure. It can also be an optical solar reflector or a paint.

Figure 2.2 - Sentinel-2B installed on its payload launcher adapter (courtesy of ESA)

2.2.1. Paint

There is only a basic understanding of the processes leading to the generation of paint flakes as surface degradation particles. The driving factors can be confined to atomic oxygen, thermal cycling and ultraviolet radiation. While paint flakes may also be generated through the impacts of meteoroids and space debris as spallation products.

A spacecraft in LEO to be subject to the influence of Earth's outer atmosphere, where atomic oxygen reacts with its surface. For many materials like silver, polymers or some metallic surfaces, oxidation processes lead to the creation of a brittle layer, which may crack and lead to the generation of spall off fragments. A more important case is when atomic oxygen is trapped between coating and substrate, which can then lead to erosion of the substrate underneath the atomic oxygen resistant coating, causing growth of cavities. This undercutting, eventually, could cause later delamination of larger coating flakes.

This mechanism would apply to susceptible substrates only and not to aluminium. The paint flake size distribution of spalls generated during such a process is difficult to model. [12]

Thermal cycling due to large temperature fluctuations during eclipse entry/exit leads to a thermal expansion of coatings and substrates at different rates, creation of cracks caused by thermal stress, growth of cracks caused by thermal stress combined with intrinsic stress, delamination[1] between a cracked coating layer and substrate leading to the shedding of flakes (µm to mm sizes). Moreover, additional UV radiation and exposure to atomic oxygen may accelerate this process. The modelling of these processes is quite complicated as the degradation processes are highly dependent on material properties, while the variety of materials used on different spacecraft and upper stages is large. Even among specific material types, like paints, there is a large diversity of properties. One of the main problems is to define the parameters describing the size distribution and the release rates for paint flakes.

In the model MASTER-2009, for example, a power law is used for the size distribution, based on validation data from returned surfaces from the Space Shuttle and LDEF[2] [13]. The release rates are based on a model published by Maclay and McKnight [14], considering releases due to the above-mentioned factors. The shape of the individual flakes in MASTER-2009 is assumed to be spherical and the density is a mean density of 4700 kg/m³, representing a mean value out of zinc, titanium and aluminium, materials typically used for paint; for the velocity distribution, a release velocity of 1 m/s is assumed for all particles [15].

2.2.2. Multi-Layer Insulation

There are two major sources resulting in the generation of MLI space debris objects:

- Thermal protections MLI from satellites/spacecraft;
- Sun-shielding MLI, which were used on radio-frequency antennas.

MLI space debris objects are generated through delamination processes. A range of surface degradations mechanisms drives the delamination process, e.g.:

- Thermal Cycling due to Sun and shade phases;
- Irradiation by the extreme ultra violet spectrum;
- Charged particle radiation and solar flare x-ray exposure;
- Atomic oxygen effects in low Earth orbits.

The ductility of the MLI material is a crucial point in the delamination process: embrittlement[3] through exposure to radiation or atomic oxygen promotes crack propagation through the material. However, atomic oxygen has also been found to increase the material ductility [16]. This occurs when carbon-carbon bonds near the surface have been severed through solar irradiation or reaction with atomic oxygen, which increases the susceptibility to foil tearing. The 'loosened' carbon chains can then be removed by, again, reacting with atomic oxygen, smoothing over the surface. Typical materials used for MLI are: Kapton®, Mylar®, Teflon® FEP and Tedlar® PVF with, typically, vapour deposited aluminium. [17]

A key aspect of MLI space debris fragment modelling is the parametrization of the area to mass ratio (A/m) of the generated fragments. The ratio depends on used materials and layer thickness. In a MLI

[1] Delamination is a mode of failure for composite materials and metals, that can occur with repeated cyclic stresses (thermal and mechanical), from oxidized metals and impacts and can cause layers to separate with significant loss of mechanical toughness.

[2] Long Duration Exposure Facility was an experiment to provide the effects of long-term exposer of materials to space environment.

[3] Embrittlement is a loss of ductility of a material, making it brittle

stack for thermal protection, the outer and inner layers are thicker than the reflector layers in between. Common thicknesses are 5 mil for the outer layers and 0.25 mil for the reflector layers (1 mil = 0.001 inch ≈ 25.4 μm). The material densities ranges are from 1.4 g/cm3 to 2.2 g/cm3.

Via a determination of a characteristic length of MLI debris parts it is possible to calculate debris part area and mass. In MASTER.2009 model the area is assumed as the square of the characteristic length. The characteristic length derives from data sets based on results of ground tests that have been performed by Kyushu University (Japan) and NASA [13] Orbital Debris Program Office, even though the available data is limited.

3. System Concept

3.1. System Requirements

Spacecraft are exposed to continuous temperature changes e.g. due to changing sun irradiation. For materials to be capable for space applications the performance under changing ambient temperatures in vacuum is an important issue. The thermal-cycling test may be used to assess materials for their space capability. The test setup used for thermal cycling of samples consists of a heating/cooling plate.

In order to simulate the space environment, the ESA Standard[4] recommends performing 100 cycles between -100ºC and 100°C under vacuum (10^{-5} Pa) with a dwell time of 5 minutes minimum and a slope of 10°C per minute.

3.2. Different approaches

Concerning the fulfilment of the requirements above mentioned several architectures were evaluated. To achieve the high temperature needed an easy solution is the use of heating resistors, they can be purchased for vacuum applications and the output power adjusted as needed.

For the low temperature requirement, the most common and widely used in cryogenic applications for temperatures from -100 to -200 °C is liquid nitrogen, with a reservoir of liquid nitrogen inside the chamber, it is possible to have a cold source at the temperature of the nitrogen's vaporization, 78 Kelvin. When speaking of applications where the temperatures are maintained constant this approach works very well, however, in cycles with a high range like the one described in the requirements, the nitrogen consumption is too high, as well as the price and there is also the question of a large enough Dewar to keep the demand.

Another solution could be based on the Peltier effect (thermoelectric cooling). It is the phenomenon that a potential difference applied across a thermocouple causes a temperature difference between the junctions of the different materials in the thermocouple. For low temperature, a commercial Peltier cell is not available and the efficiency is well below 10% [18].

An additional solution, is the Vapor-Compression Refrigeration, it is because it is easy to build a low-cost cooling device employing this method. Air conditioners in car and at home uses a vapor-compression cycle to cool the ambient air temperature. The vapor-compression refrigeration cycle is comprised of four steps: compression, condensation, throttling and evaporation. The drawback with a vapor-compression is that for the low temperatures, below -60 °C, the fluids based on Ammonia are not suitable, so an alternative fluid would be necessary. [19]

The helium based compressor/expansion cryocooler systems are normally used to achieve lower temperatures. These systems are mainly developed to cool down small material samples to enable physical studies. The heat power is however limited and we were fortunate to have already in the group a rather powerful helium compressor/expander system.

The thermal switching between the heating and cooling stages is also a challenge. One interesting technology is to use thermal switches where a small, but large area, material gap achieves variable thermal conduction by varying the pressure of a thermal conducting gas. The pressure is usually varied, inside the cryostat by including an adsorption pump in the gas reservoir. The heat flow in these systems is however highly limited [20]

[4] ESA Product Assurance ECSS-Q-70-04C, 2008

A mechanical switch between hot and cold masses had to be implemented inside the cryostat system and typically would require the usage of cryogenic motors or, at least, cryogenic mechanisms or magnetic coils to exert appreciable contact forces between the temperature coupling parts.

Another option was to use an external mechanical system that would directly exert the mechanical contact forces tough a mechanical connection inside a vacuum bellow. Thermal isolation and careful vacuum wall design are still a challenge.

Those were the first ideas about this subject while presenting their advantages and weak points. In the next section, the chosen architecture is presented and explained in detail.

3.3. Design Description

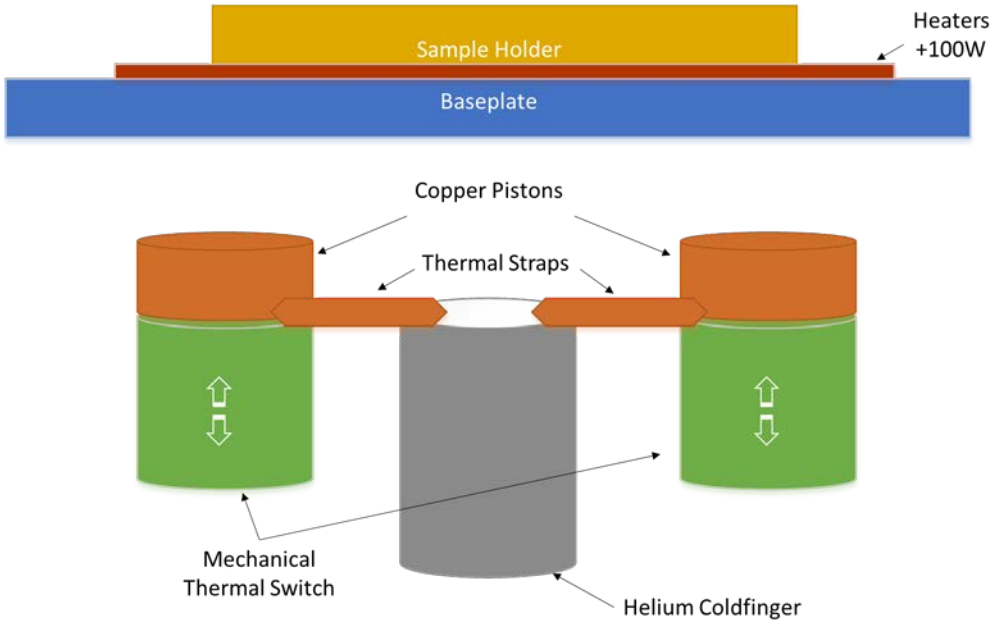

Figure 3.1 – Thermal Vacuum Cycle Conceptual Design

The chosen architecture is based on the use of a Helium cryocooler as a cold source and the resistors as heaters. From the conceptional point of view, the cold source must have a thermal interface that disengages when the heaters are working, preventing unnecessary heat flowing to the cryocooler. This concept architecture allows the operation to work unattended for extended periods.

The Figure 3.1 shows the conceptual design of the TVC system. In particular, the Thermal Mechanic Switches which implements the thermal interface between the cold finger and the base-plate.

The thermal cycling will be performed on a vacuum chamber with 10^{-5} mbar of pressure and a temperature range from -150 to 150°C. This higher temperature range is used in order to create accelerated test conditions over the operation conditions. Usually, the term acceleration factor (AF) is used to refer the ratio of the acceleration characteristic between the operation level and a higher test level. A calculation of the AF is provided in chapter 8.4, as part as the performance of the system.

The main vacuum chamber had already been developed in the group [21] and was available for these studies. The overall dimensions are of a 1m long cylinder that has an inner dimeter of about 60cm.

The sample holder (where the MLI and the paints are to be assembled) will be assembled on top of an aluminium base plate[5] that will be heated/cooled. During cool down, the cold finger will be put in contact with the baseplate by means of mechanical thermal switches.

The thermal switching, i.e. hot to cold and vice-versa, is achieved with the use of three pneumatic pistons connected to the cold source. When disconnected, the heaters are turned on to reach the top temperature and to perform a cooldown, the heaters are turned off and the pneumatics are engaged. The thermal connection between the cold finger and the pistons is made with copper straps.

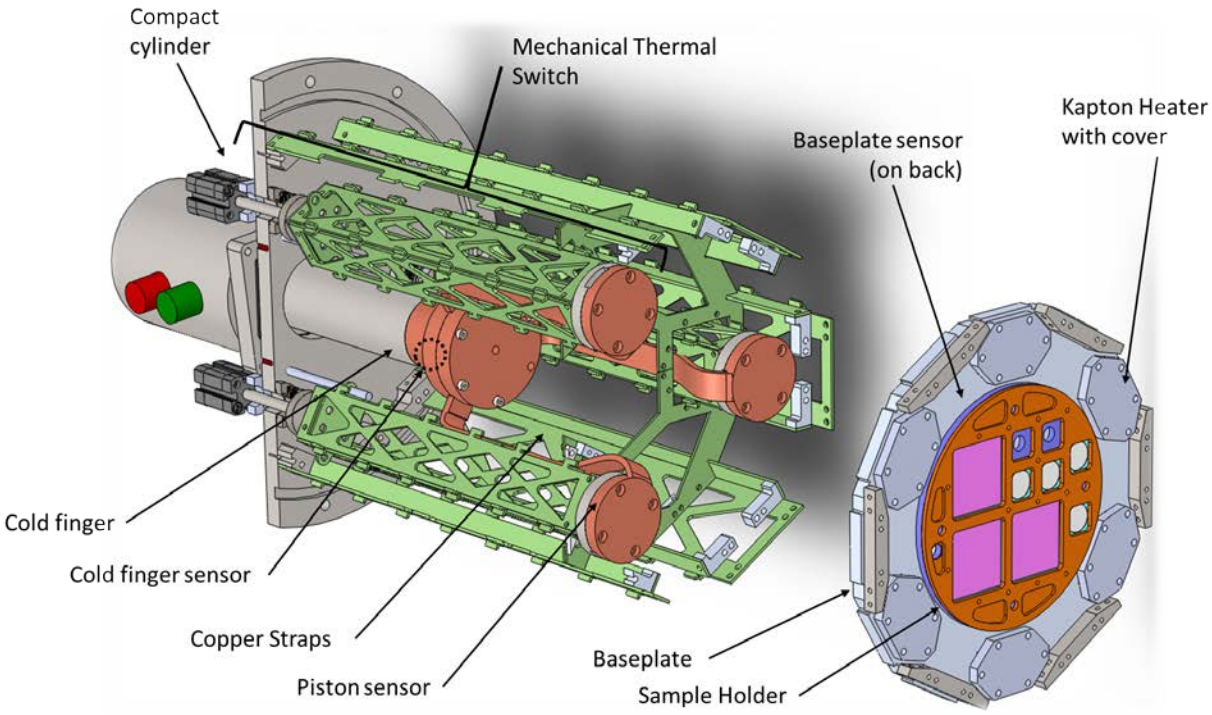

Figure 3.2 – Detail model of the chosen design

Below there is a description of the items presented in Figure 3.2:

- Mechanical Thermal Switch

The mechanical switches consist in compressed air pneumatic system using a flexible bellow as a linear vacuum feedthrough. The cold part is isolated by an epoxy with low thermal conductivity, used in cryogenics and vacuum applications. This system allows to disconnect the cold source from the hot source mechanically.

[5] Referred as *baseplate* in the document

- Baseplate

The baseplate is the part of the system where the resistors are attached, and the thermal connection with the cold finger is made on its back. And where the samples to be tested will be placed.

- Heater

For heater, we selected Kapton flexible foils [22] because they have a wide operational temperature and we have used them in the past for this kind of application. The Kapton foil heaters will be positioned between the sample holder and the baseplate.

- Heat Pump

A helium cryocooler is used to cool down the baseplate. The cryocooler [23], at -150 ℃, is able to remove 90 watt. The section area of the copper strip can be customized to fit the desired power flux.

- Thermal Isolation

Besides the isolations provided by the epoxies, a MLI blanket is used to shield from the radiation emitted by the chamber walls, at room temperature.

In order to fulfil the ESA standard requirements there will be 4 stages: Warm Up, High Temperature Dwelling (HTD), Cool Down and Low Temperature Dwelling (LTD). The temperature control will be achieved by:

a) Monitoring the sample holder with PT100 temperature sensors, due to low voltage measurements, Omega controllers [24]will be used;
b) Heating procedure:
    i. During heating, the thermal switch will disconnect thermally the cold finger from the back plate;
    ii. The Kapton resistors will be tuned on up to achievement of the top temperature (e.g. 150 °C);
c) During cool down:
    i. The resistors will be turned off and the mechanical thermal switches will be turned on, connecting thermally the cold finger to the back plate. This situation will endure up to minimum temperatures (e.g. -150 °C);
    ii. Temperature stabilization will turn on the resistors.

4. Material selection

Materials for the different parts of the system were selected based on part function and their mechanical/thermal proprieties. Previous experiences with some materials, in terms of machining and procurement, were fundamental during the process of selection.

The thermal conductivity of a material, gives its ability to transfer the heat. In a material with a high thermal conductivity will have a heat flux higher than a material with a low thermal conductivity.

- **Aluminium**

The 5083 aluminium is known for exceptional performance in extreme environments. The 5083 aluminium is a lightweight, strain hardened, corrosion resistant and high strength alloy is commonly used in high strain rate applications such as those experienced under shock loading [25].

Table 4.1 – Properties of aluminium 5083, at 25 °C

Physical Property	Value
Density	2660 kg/m³
Tensile Strength	290 MPa
Elastic Modulus	70 GPa
Thermal Expansion	24 x10^{-6} /K
Thermal Conductivity	121 W/m.K
Specific Heat	900 kJ/kg.K

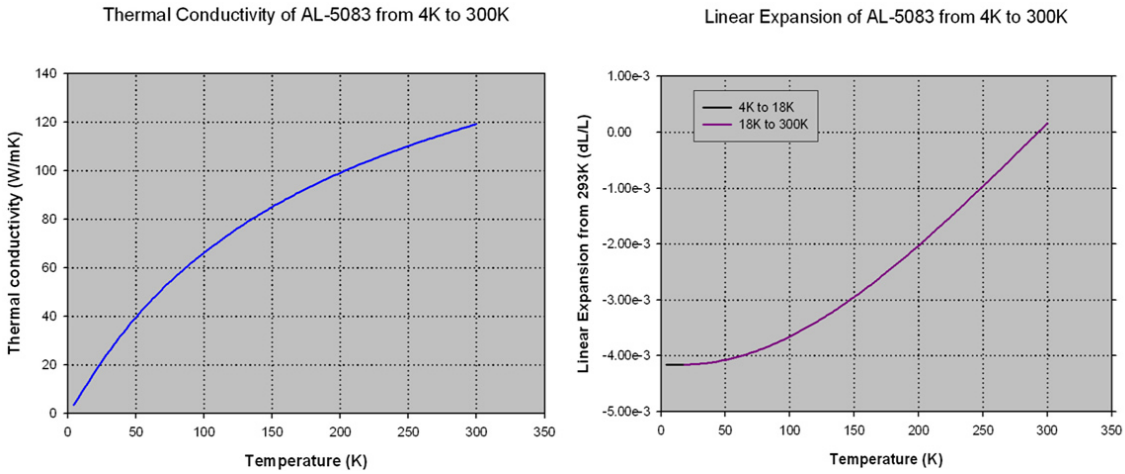

Figure 4.1 – Variation of the thermal conductivity and linear expansion of the aluminium [6]

[6] Data provided by Cryogenic Technology Group at NIST

- **Stainless Steel**

Austenitic stainless steels are the most common choice for high vacuum and ultra-high vacuum systems. The 304 stainless steel is a common choice of a stainless steel.

Table 4.2 – Properties of stainless steel, at 25 °C

Physical Property	Value
Density	8000 kg/m³
Tensile Strength	517 MPa
Elastic Modulus	190 GPa
Thermal Expansion	18 x10^{-6} /K
Thermal Conductivity	16 W/m.K
Specific Heat	500 kJ/kg.K

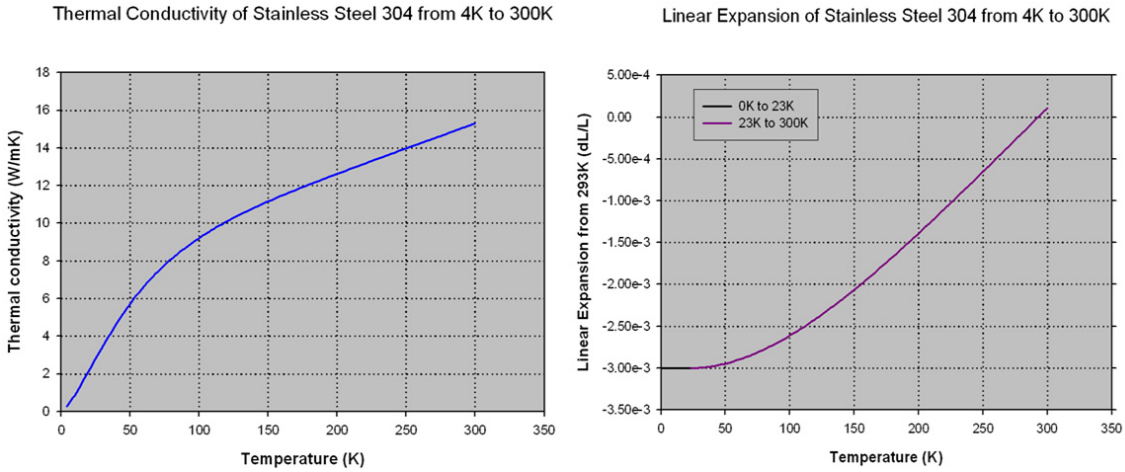

Figure 4.2 – Thermal conductivity and linear expansion of the 304 stainless steel.

- **Copper**

Oxygen-free high thermal conductivity (OFHC) copper is widely used in cryogenics. Due to its high purity, 99.99%, it is expensive. The copper is a good heat exchanger due to its good thermal conductivity. The copper is used in the thermal straps and where they attached, namely, the cold finger and the pistons.

Table 4.3 – Properties of copper, at 25 °C

Physical Property	Value
Density	8900 kg/m³
Tensile Strength	395 MPa
Elastic Modulus	110 GPa
Thermal Expansion	24 x10^{-6} /K
Thermal Conductivity	390 W/m.K
Specific Heat	900 kJ/kg.K

- **Epoxy**

The ISOVAL® FR4-HF is a halogen free epoxy glass laminate with a limiting temperature of 180 °C. Epoxy glass laminates are even usable for cryogenic applications at temperatures close to absolute zero. Also for these laminates an increase in mechanical strength and modulus of elasticity can be observed but also at very low temperature for example, in liquid nitrogen or liquid helium they do not show vitreous embrittlement as rubber or thermoplastics do.

Table 4.4 – Properties of Epoxy, at 25 °C

Physical Property	Value
Density	2000 kg/m³
Tensile Strength	374 MPa
Elastic Modulus	18.9 GPa
Thermal Expansion[7]	30 x10^{-6} /K
Thermal Conductivity	0.36 W/m.K

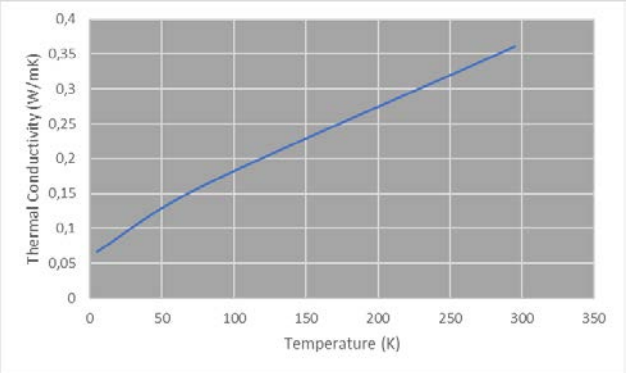

Figure 4.3 – Thermal conductivity of Isoval Epoxy.

[7] A thermal expansion is not available from the manufacture datasheet. A conservative value was used.

5. Thermal Simulations

In this case, as in any other engineering problem, the analysis of mechanical systems has been addressed by deriving differential equations relating the variables of through basic physical principles such as, conservation of energy and the laws of thermodynamics. However, once formulated, solving the resulting mathematical models is often impossible, especially when the resulting models are nonlinear partial differential equations. In this chapter, the thermal analysis of the chosen architecture, using both analytical lumped circuit and numerical finite element methods are presented.

5.1. Approximated Lumped Network Analysis

In Figure 5.1 a simplified scheme of the thermal system is shown. As a rough approximation, the thermal contact resistance between the Sample Holder and the Pistons is considered insignificant, however the heat flux is limited by the area and length of the copper part of the piston. The thermal straps also add a resistance to the heat flux.

As a convention, the heat flows from the Sample Holder (at a higher temperature) to the Cryocooler (at a lower temperature).

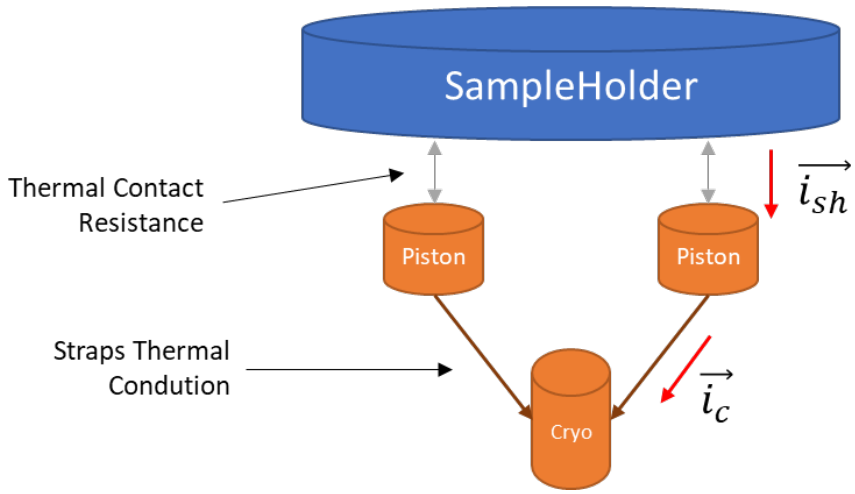

Figure 5.1 - Simplified scheme of the thermal system for lumped network analysis

An effective way to better understand the thermal problem is to use the analogy between thermal and electrical networks. The voltage (rather than temperature) at various nodes can be calculated together with the current (rather than heat) flow between nodes. For transient analysis, electrical capacitances (rather than thermal capacitances) are added to account the change internal energy of the body with time. The thermal resistances are resultant from geometric dimensions, thermal properties of the materials and heat transfer coefficients. [26,27]

The equivalent circuit diagram that relates the heat path from the Sampler Holder to the Cryocooler is depicted in Figure 5.2. Where the generator, V_c, is the temperature in the cryocooler, R_T is the sum of the internal resistance of the cryocooler and the thermal conduction of the copper straps, C_p is the heat capacity of the pistons, R_c is the contact resistance between the pistons and the sample holder and C_{sh} is the heat capacity of the sample holder.

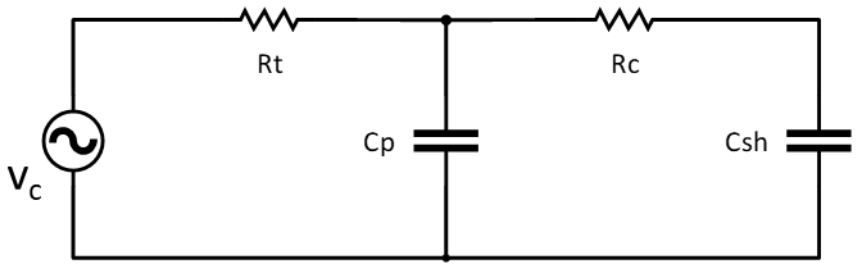

Figure 5.2 – Electrical transmission line equivalent circuit diagram for modelling heat conduction properties; the physical variables are specified in their thermal equivalents.

Table 5.1 - Corresponding physical variables

Thermal		Electrical	
Temperature	K	Voltage	V
Heat flow	W	Current	A
Thermal resistance	K/W	Resistance	V/A
Thermal capacitance	Ws/K	Capacitance	As/V

For the circuit in Figure 5.2, the following equation system that describes it is retrieved.

$$\begin{cases} i_{sh} = -C_{sh}\dfrac{dV_{sh}}{dt} & (1) \\ V_{sh} - V_p = R_c i_{sh} & (2) \\ i_{sh} - i_c = C_p\dfrac{dV_p}{dt} & (3) \\ V_p - V_c = R_T i_c & (4) \\ i_c = k_0 V_c + k_1 & (5) \end{cases}$$

Particular solutions are in the form of:

$$\vec{X} = \overrightarrow{C^0} a e^{-at} \tag{6}$$

$$\begin{bmatrix} 0 & 0 & C_{sh}a & 1 & 0 \\ 0 & -1 & 1 & -R_c & 0 \\ 0 & -C_p a & 0 & 1 & -1 \\ -1 & 1 & 0 & 0 & -R_T \\ -k_0 & 0 & 0 & 0 & 1 \end{bmatrix} \begin{bmatrix} V_c^0 \\ V_p^0 \\ V_{sh}^0 \\ i_{sh}^0 \\ i_c^0 \end{bmatrix} = \begin{bmatrix} 0 \\ 0 \\ 0 \\ 0 \\ k_1 \end{bmatrix} \tag{7}$$

To determine the exponential argument, the determinant must be set to zero.

There are two solutions for a are given by:

$$a = \frac{k_o[C_pR_T+C_{sh}(R_c+R_T)]+C_{sh}+C_p}{2C_pC_{sh}R_c(k_oR_T+1)} \pm \frac{\sqrt{(k_o[C_pR_T+C_{sh}(R_c+R_T)]+C_{sh}+C_p)^2-4k_oC_pC_{sh}R_c(k_oR_T+1)}}{2C_pC_{sh}R_c(k_oR_T+1)} \quad (8)$$

The constants R_T and R_c were calculated as the inverse of the thermal conductivity. For R_T was used the length of the copper straps and it section. The lack of studies about surface-to-surface contact in vacuum, between aluminium and copper, R_c was assumed to be limited by the thermal conductivity of the copper part of the pistons. C_{sh} was determined by the heat capacity of the sample holder, made entirely of aluminium. C_p was calculated by adding the heat capacity of the stainless steel and copper of the piston. Table 5.2 shows the determined constants.

Table 5.2 – Parameters used in the lump model

Parameters	Value
C_p	832.5
C_{sh}	291.35
R_T	4.867
R_c	6.64E-03

Replacing equation (8) with the constants in the previous table two solutions for a are obtained. The solutions are:$a \rightarrow \{6.979 \times 10^{-01}, 1.396 \times 10^{-04}\}$,meaning the solution is a linear combination of two exponential. This result was expected since there are two mechanisms involved in the cooling process, one from the thermal mass of the pistons, a very quick process, and a second form the conduction on the straps. The typical curve of this cooldown is shown on Figure 5.3

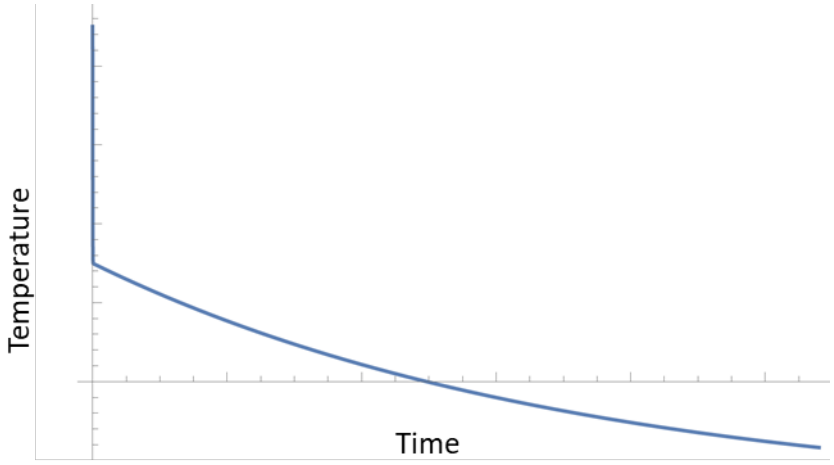

Figure 5.3 – Typical curve of the cooldown.

5.2. Finite Element Method

The finite element method (FEM) is the dominant discretization technique in structural mechanics. The basic concept in the physical interpretation of the FEM is the subdivision of the mathematical model into disjoint (non-overlapping) components of simple geometry called finite elements or elements for short. The response of each element is expressed in terms of a finite number of degrees of freedom characterized as the value of an unknown function, or functions, at a set of nodal points.

The response of the mathematical model is then considered to be approximated by that of the discrete model obtained by connecting or assembling the collection of all elements. All analyses were performed using the Simulation Add-in in SolidWorks.

For the TVC system the main concern was the thermal conductivity, either from the hot base-plate to the flange, dissipating needed power to raise the base-plate temperatures or from the flange to the cold base-plate. These simulations are referred as *Static Analyses*.

A dynamic Simulation was also accomplished in order to assess the time needed for a full cooldown of the system, from 150 to -150 °C.

5.2.1. Static Analyses

A static simulation was performed on the fiberglass epoxies, both inner and outer, in order to determine the quantity of heat transfer during a thermal cycle. To assess those quantities, the extreme temperatures were considered as a worst-case scenario.

- Outer Epoxy

  The outer epoxy experiences both high and low temperatures at one end and the other is attached to the flange, which gives a good thermal connection, so it stays always at room temperature.

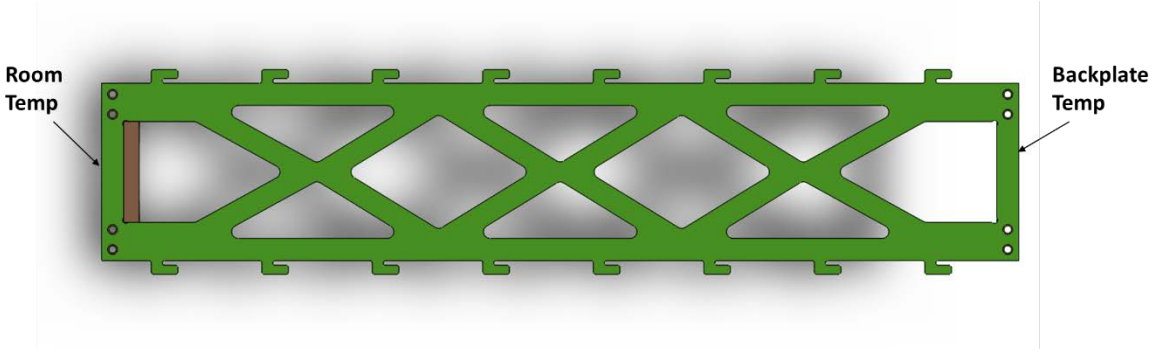

Figure 5.4 – CAD model used to simulate the applied thermal loads. On the base-plate, the thermal loads applied for this simulation are -150 and 150 °C.

A mesh is a discretization of the CAD model. Finite elements and nodes define the basic geometry of the physical structure being modelled, splitting the geometry into relatively small and simple geometric entities, called finite elements. The use of the term “finite” is to emphasize the fact that those elements infinitesimally small, but only reasonably small in comparison to the overall model size.

Each element in the model represents a discrete portion of the physical structure, which is, represented by many interconnected elements. Shared nodes connect these elements to one another.

The greater the mesh density (that is, the greater the number of elements in the mesh), the more accurate the results will be. As the mesh density increases, the analysis results converge to a unique

solution, increasing the computer time required for the analysis. The solution obtained from the numerical model is generally an approximation to the solution of the physical problem being simulated.

A good quality mesh is important for obtaining accurate results from simulations, having different quality check criteria to measure the quality of the mesh. An important parameter in the assessment of the mesh quality is the Aspect Ratio Checks. [28] The simulation accuracy is best achieved by a mesh with uniform size elements whose edges are equal in length. So, by definition, the aspect ratio of a perfect tetrahedral is 1.0.

The Table 5.3 summarizes the mesh used in this simulation. Since 89% of the elements have an aspect ratio below 3.0, the mesh is considered of good quality. Figure 5.5 shows the mesh obtained.

Table 5.3 – Mesh description

Mesh information	
Mesh type	Standard mesh
Total Nodes	36158
Total Elements	18379
% of elements with Aspect Ratio < 3	89 %
% of elements with Aspect Ratio > 10	0.0326 %

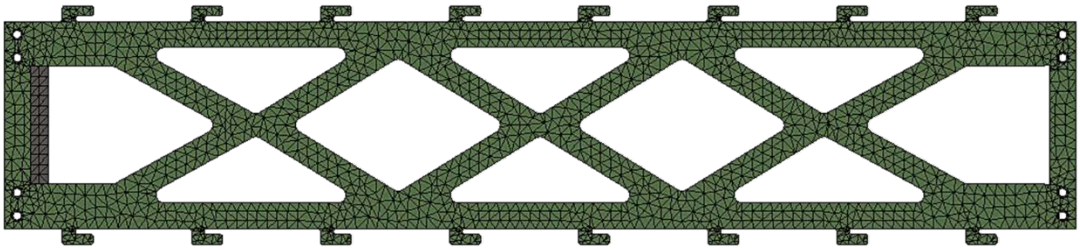

Figure 5.5 – Representation of the mesh used in this simulation.

In these simulations only thermal conductivity was considered, a good approximation since in vacuum there is no convection and assuming that all thermal radiation from the wall of the chamber, at room temperature, are shielded by the MLI blankets.

These simulations are driven by the following heat balance equation

$$Q - \frac{\partial q_x}{\partial x} - \frac{\partial q_y}{\partial y} - \frac{\partial q_z}{\partial z} = c\rho \frac{\partial T}{\partial t} \tag{9}$$

where q_x, q_y and q_z are the heat flux in the x, y and z directions, Q is the internal heat generated/absorbed by the body (volume), c is specific heat, ρ is mass density and T is temperature.

The Fourier's law of heat conduction relates heat flux and temperature and is proportionality constant to k, the thermal conductivity. For an orthotropic body (volume element), with the axes of orthotropy coinciding with the coordinate axes the Fourier heat conduction equation is

$$\vec{q} = -k\vec{\nabla}T \tag{10}$$

Joining (9) and (10)

$$Q = c\rho\frac{\partial T}{\partial t} - k\vec{\nabla}^2 T \tag{11}$$

The analysis of steady-state heat conduction problems involves setting the term $^{\partial T}/_{\partial t}$ equal to zero and with Q assumed to be independent of time.

Taking this into account, in the first simulation the baseplate is considered at 150 °C. As described in Figure 5.4, the temperature applied on the left side is the flange temperature, at room temperature, so 25 °C, and on the right the 150 °C is applied.

In Figure 5.6, there are plotted the results of this simulation. The top plot shows the temperature gradient on the epoxy and on the bottom the heat flux. The important result here is the total power transferred throw the epoxy, which should be the minimum. The simulation shows 0.02 watts being transferred.

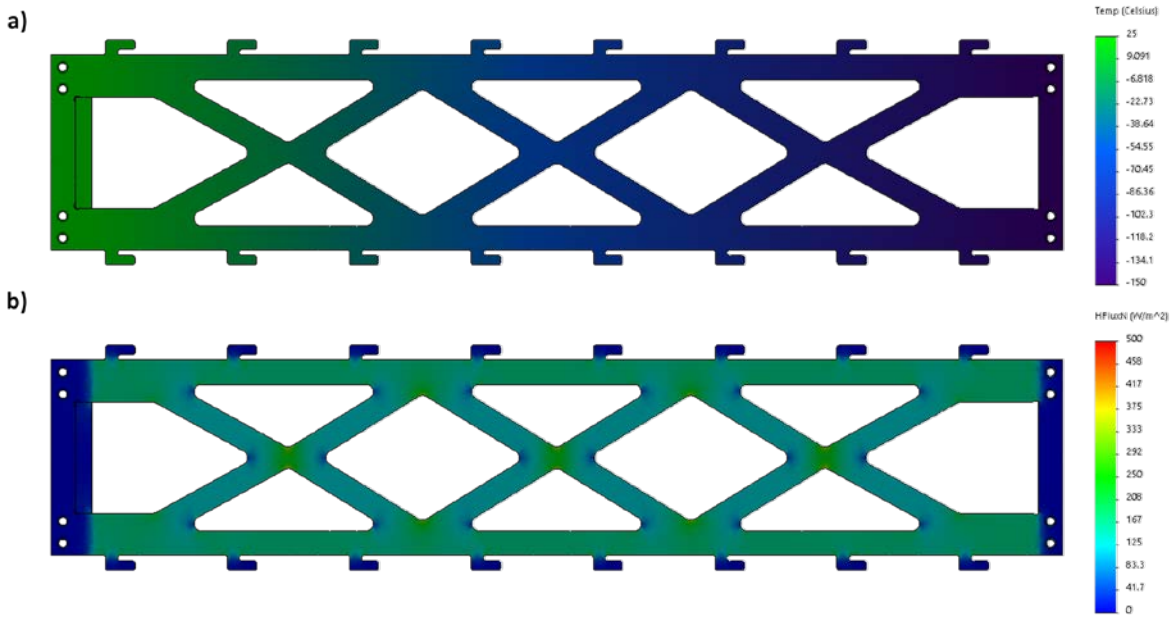

Figure 5.6 – Thermal analysis to outer epoxy support when large clutch is at -150°C.
In a) is plotted a temperature map and in b) the heat flux. The power transferred in this simulation was about 0.02 watt.

Since the model is the same, it was used the same mesh to simulate it with a different temperature in the extremity, the result is as plotted below. Again, the top plot of Figure 5.7, shows the temperature gradient on the epoxy and on the bottom the heat flux. The power transferred was 0.015 watt.

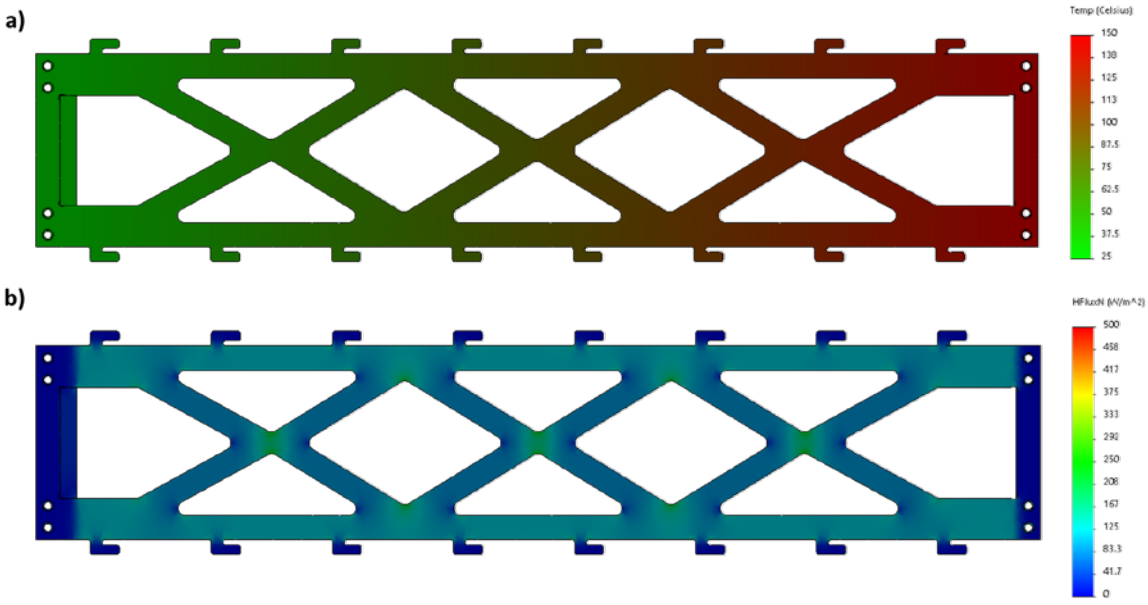

Figure 5.7 – Thermal analysis to outer epoxy support when large clutch is at -150°C.
In a) is plotted a temperature map and in b) the heat flux. The power transferred in this simulation was about 0.015 watt.

- Inner Epoxy

The inner epoxy is connected at one end to the flexible bellows, so one can assume it at room temperature, while the other end is attached to the copper strips. The temperature of the strips for the purpose of this simulation is considered to be at -150 °C, at all times.

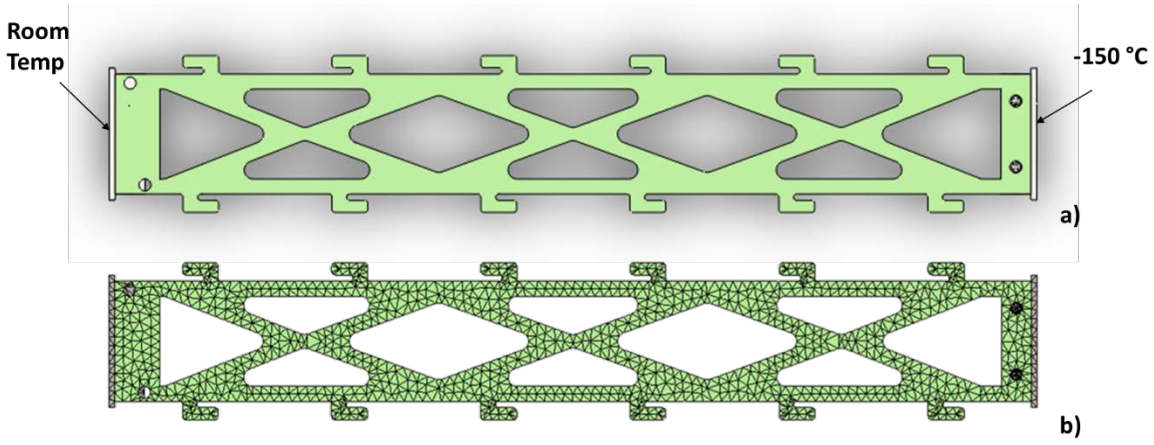

Figure 5.8 –a) CAD model used in inner epoxy simulation; b) Representation of the mesh used in this simulation.

By analysing the Table 5.4, one can conclude that the mesh is good since 91% of the elements have an aspect ratio smaller than 3.

Table 5.4 – Mesh description

Mesh information	
Mesh type	Standard mesh
Total Nodes	45214
Total Elements	25606
% of elements with Aspect Ratio < 3	91.5 %
% of elements with Aspect Ratio > 10	0.133 %

In Figure 5.9, the results of the simulation are plotted. The top plot shows the temperature gradient on the epoxy and on the bottom the heat flux. The important result here is the total power transferred throw the epoxy, which should be the minimum. The simulations show that 0.02 watts are transferred.

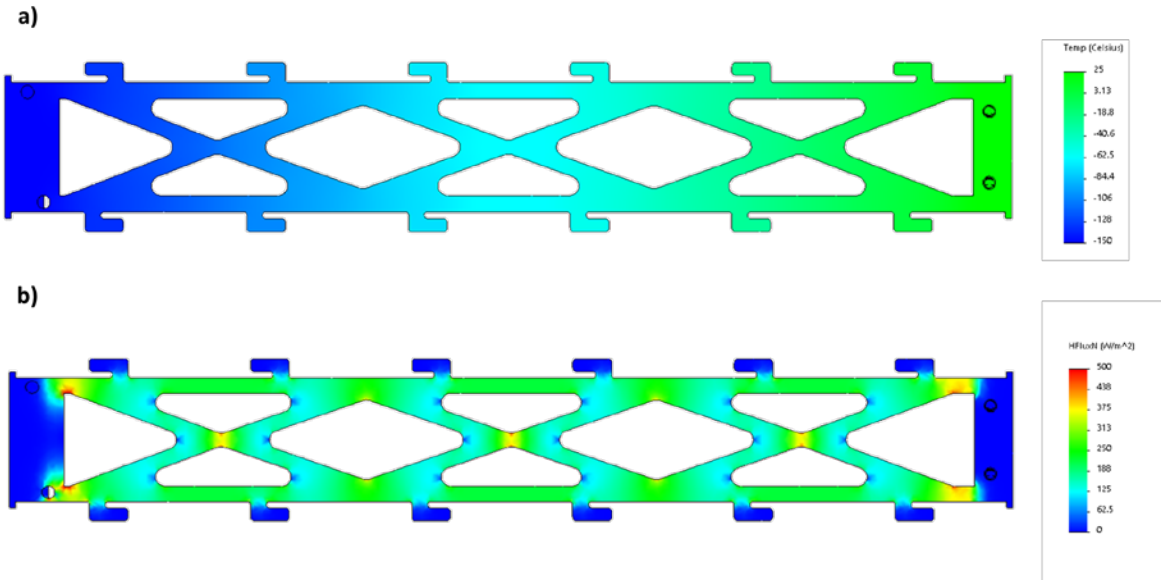

Figure 5.9 – Thermal analysis to inner epoxy support.
In a) is plotted a temperature map and in b) the heat flux. The power transferred in this simulation was about 0.02 watt.

5.2.2. Dynamic Simulation

The dynamic simulations were performed in order to assess the time needed for a cooldown. A simplified CAD model was used for this simulation. It is shown in Figure 5.10, the CAD model used for this simulation. The output power of the cryocooler is depended of its temperature and that dependency was used in the simulation and the base plate was set to 150 °C, as initial temperature.

The results of this dynamic simulation are shown in the plot Figure 5.11.

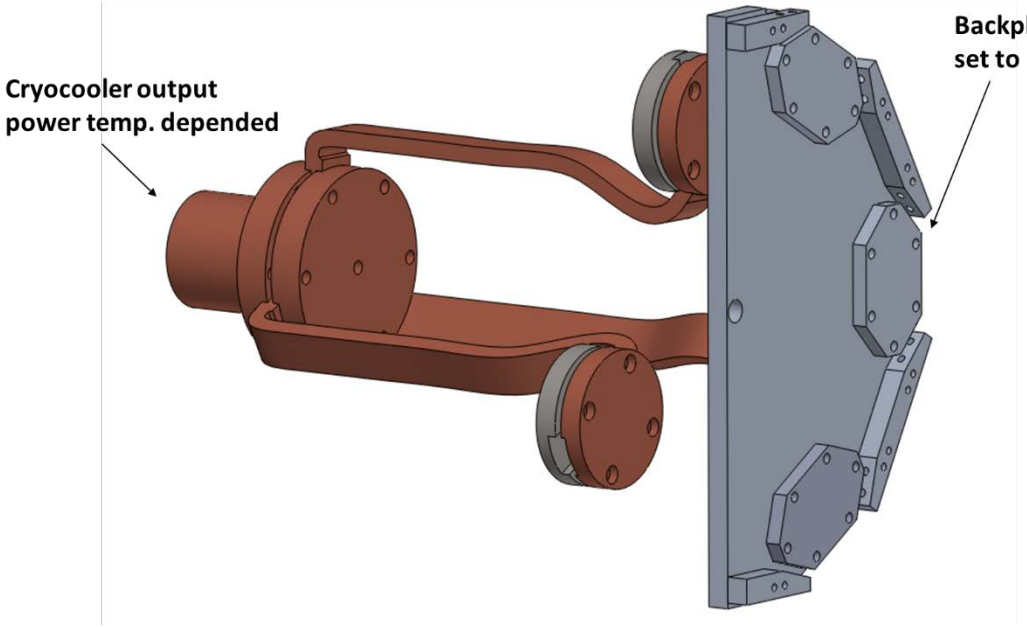

Figure 5.10 – Section view of the CAD model

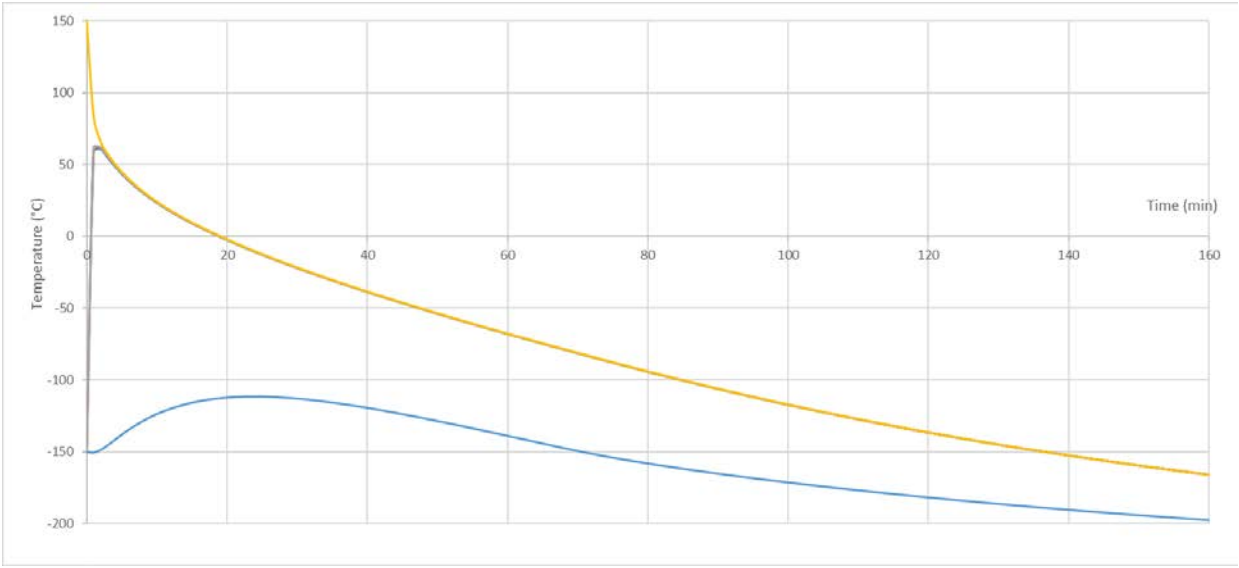

Figure 5.11 – Cool down time simulation.

A cool down rate of 4°C/min in the 150 to -150 °C range can be measured from Figure 5.11 . In blue, it is represented the temperature of the cold finger and the outer represent 3 sensors placed on the top of the sample holder. It's possible to see that the sample holder can reach the temperature of -150 °C in 80 minutes.

In order to compare this result with the one obtained from the lumped model in 5.1, it is necessary to perform a non-linear fitting on the temperature of the sample holder. A two-phase exponential decay function with time constant parameters model was used. The equation for the two-phase exponential decay function is:

$$T_{sh} = A_1 e^{-t/\tau_1} + A_2 e^{-t/\tau_2} + T_{sh}^0 \quad (12)$$

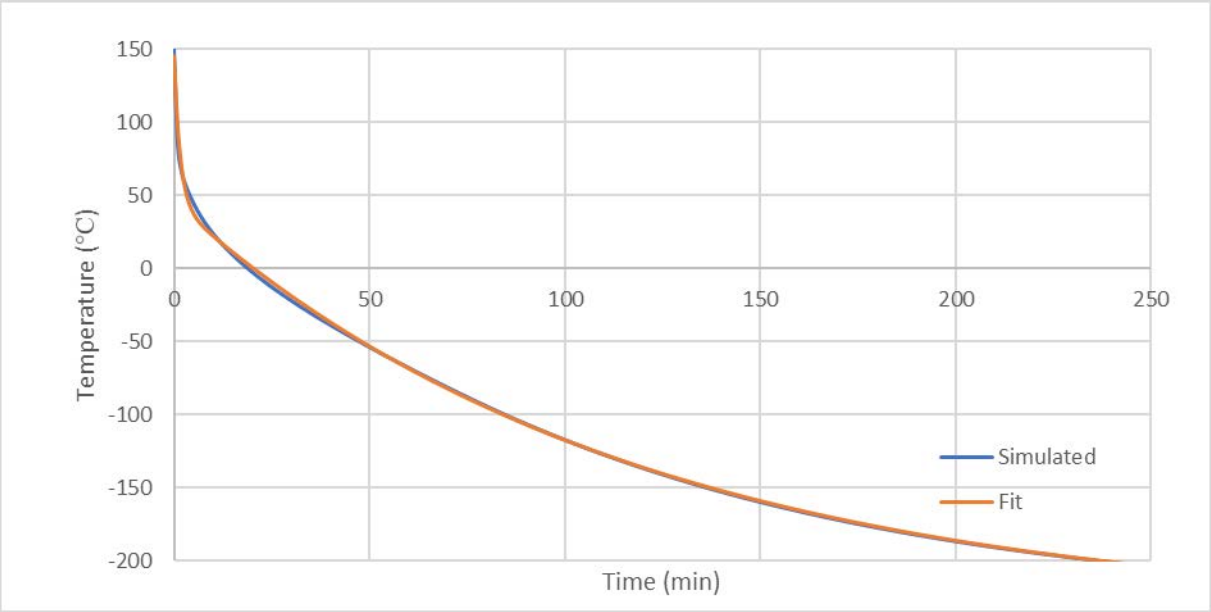

Figure 5.12 – Cool down fit

For the fit of the temperature on the sample holder over time, it is possible to determine the two-time constant parameters, a_1 and a_2. The following table shows the parameters calculated:

Table 5.5 - Parameters determined for the fit of the dynamic simulation result

Variable	Value	Standard Error
T_{sh}^0	-236.735	0.693
A_1	99.960	1.576
τ_1	93.728	2.992
A_2	281.677	0.541
τ_2	6974.883	44.291

Inverting τ parameters to get the a_1 and a_2 to compare with the ones in section 5.1, it became:

$$\vec{a} \rightarrow \{1.067 \times 10^{-02}. 1.434 \times 10^{-04}\}$$

For the first exponential, the one with higher decrease in velocity, it represents a difference of a decrease of 98% over the initial estimated in lumped model. This means that the thermal contact between the Base Plate and piston was over estimated in the lumped model, making this process slower. The second exponential term was increased by 3%.

5.3. Thermal Expansion

This is only a brief discussion about thermal expansion since it does not play a major role in this system. Even with the temperature ranges expected for this system, the expansion is in the order of a few micrometres. For instance, the expanse of the stainless steel in the parallelepiped (see Figure 5.13) is 0.135 mm and in the epoxy, is 0.266 mm (Appendix B) . This means that alignment pins are not an option, but the use of screws is acceptable.

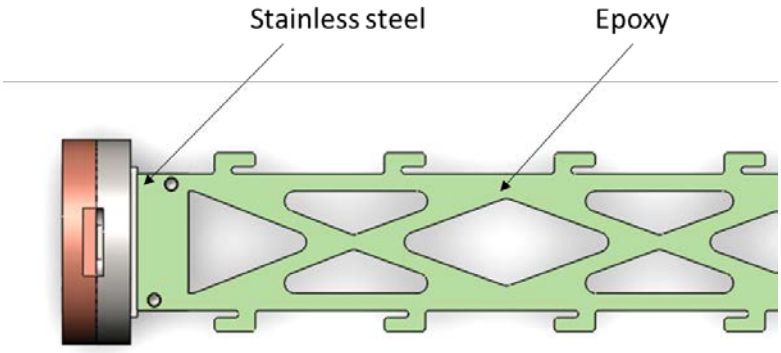

Figure 5.13 – Mechanical switch expansion

6. System Development

After the validation of the design. the parts needed to be manufactured (in-house or from external companies) and the COTS obtained. In this chapter. the manufacture processes are described. as well. as the assembly process.

6.1. Manufacture

All parts in aluminium and epoxy were produced in the Department of Physics' workshop with the aid of a 3D milling machine. The parts drawn in SolidWorks were converted in g-code file using SolidCam[8]. Afterwards. the CNC software interprets the g-code and reproduces the 3D models.

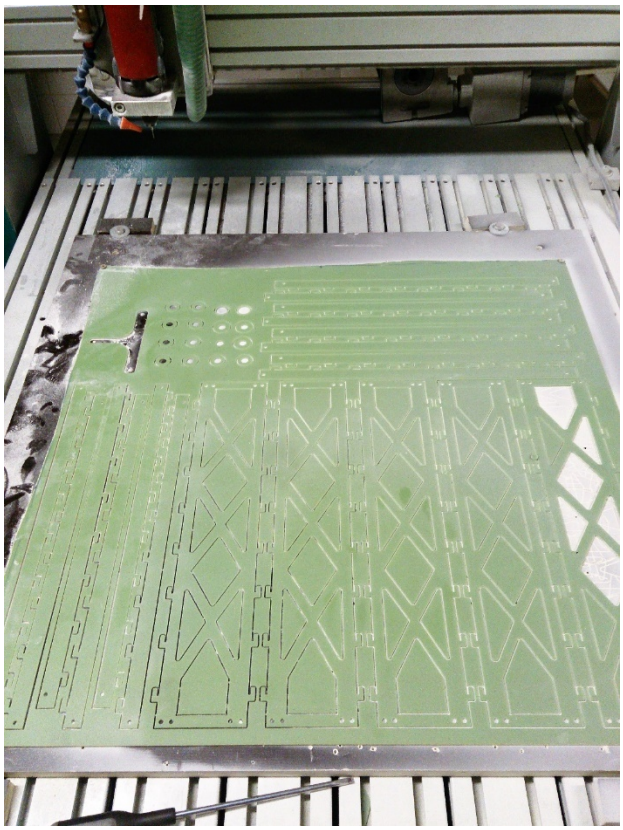

Figure 6.1 – Epoxy after the CNC milling process.

[8] SolidCam is a plug-in that is fully associative with the SolidWorks design model, so that is possible to program a CNC's directly inside SolidWorks.

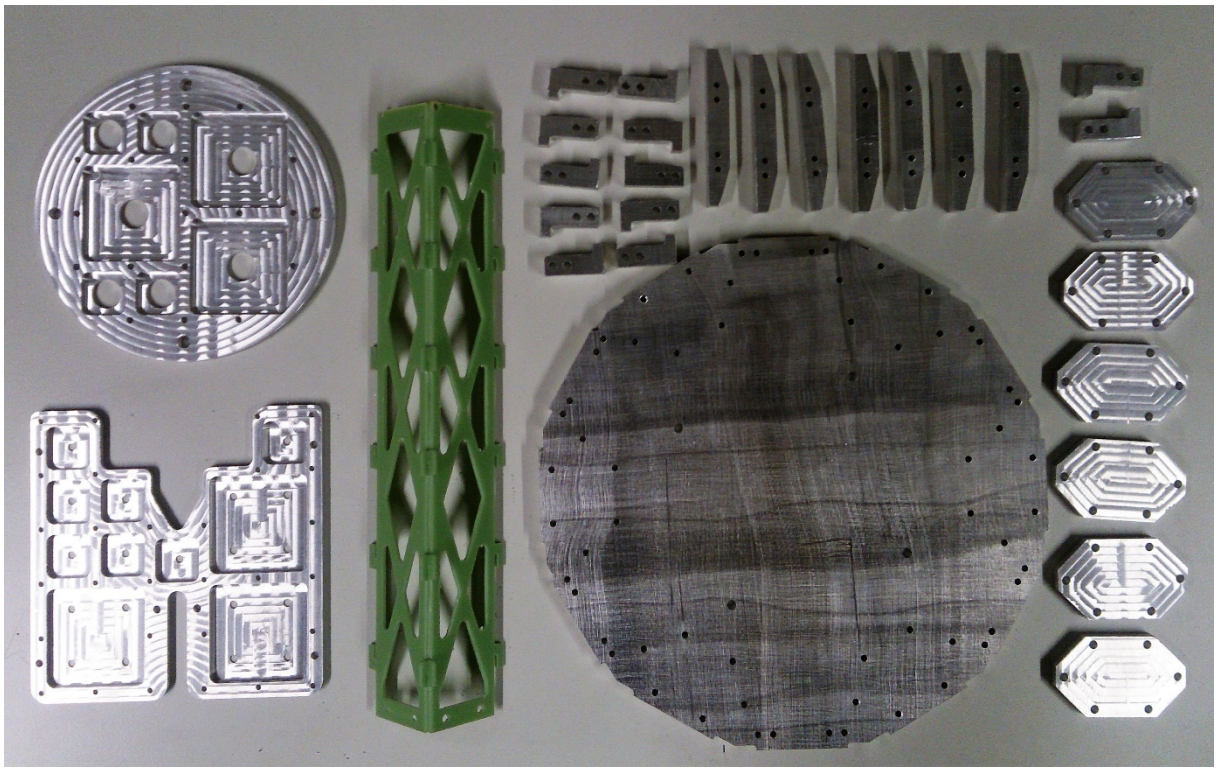

Figure 6.2 – Display of most parts produced using the CNC machine at the workshop.

The Inox and copper parts were outsourced. since their milling process are a much more time-consuming process and the level of proficiency needed is higher. In Appendix D , the mechanical drawings send to manufacture are displayed.

6.2. Assembly

The TVC is assemblied in a vacuum chamber with a cylindrical. with 986 mm of length and a 321 mm radius of base and stainless steel. The vacuum pumping mechanism consists on a turbomolecular vacuum pump and it is used to obtain and maintain a pressure inside the chamber under 10^{-6} mbar monitored by a vacuum sensor.

The vacuum chamber used was built in 2012 and it had been a part of two other projects. The GRAVITY. an ESO project. the Gravity is a second-generation instrument at VLTI. which combines the four beams from the VLT. The near-infrared wavelength implies the need of cryogenic operation temperatures. The MAGDRIVE is a FP7 project and aimed the development of superconductors' gearbox with the purpose of reducing the friction between moving parts.

Below. Figure 6.3 to Figure 6.5 show in detail the assembly process.

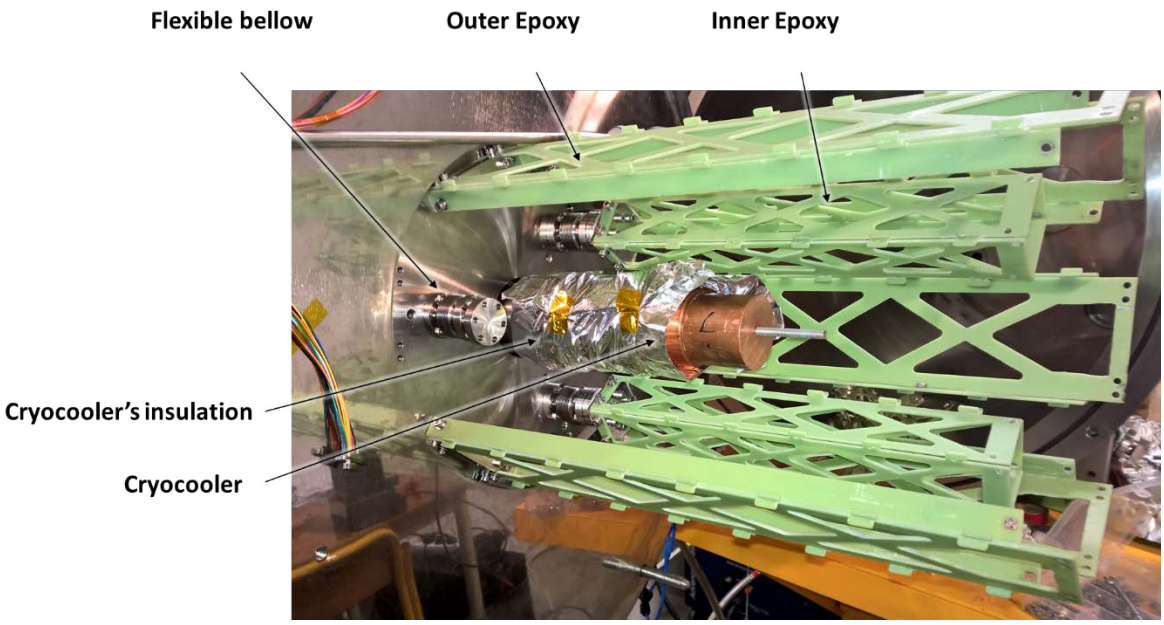

Figure 6.3 – Assembly of the outer epoxy, showing the details of the Mechanical Thermal Switch (flexible bellow and inner epoxy)

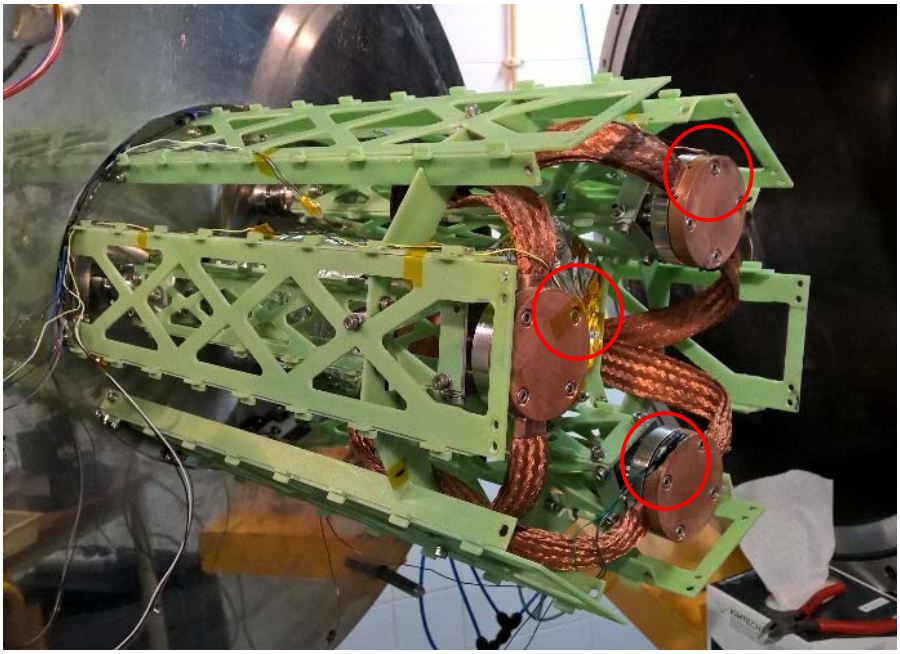

Figure 6.4 – System without the aluminium base-plate. showing the copper thermal interface of the pistons. Inside the red circles it can be seen the position of the temperature sensors.

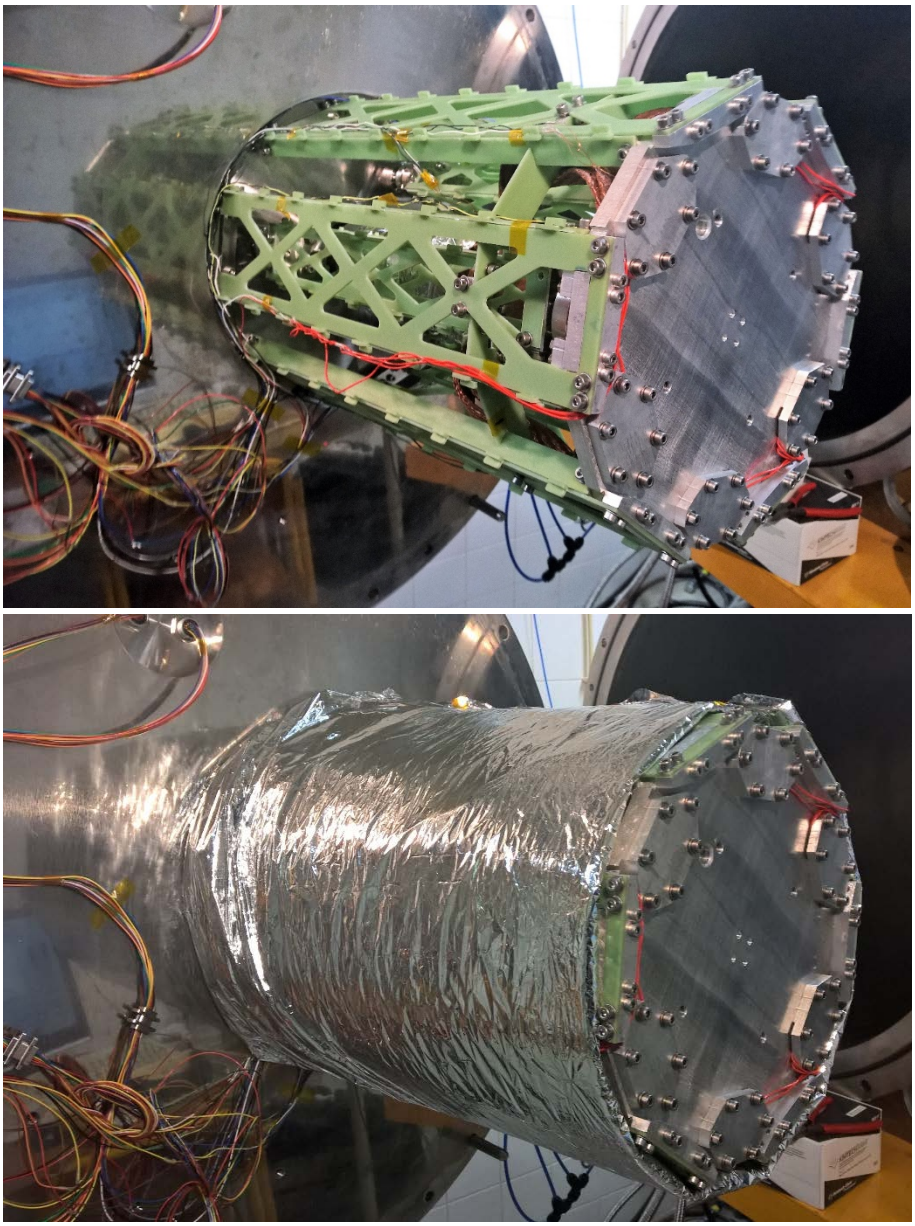

Figure 6.5 – The top picture shows the system assembled. On the bottom, a MLI blanks was placed around the outer epoxy as a thermal radiation shield.

7. Data Acquisition and Control

The data acquisition and control for the thermal cycling was performed through a LabVIEW program using a USB DAQ form LabJack and a SERIAL protocol.

7.1. LabJack U12

The LabJack U12 is a measurement and automation peripheral that is USB based. The LabJack has eight analogue input signals, which can operate as eight single/ended channels or four differential channels. Each input has a 12-bit resolution and the input range for a single-ended measurement is ±10 volts.

The DB25 connector provides connections for 16 digital I/O lines, numbered from D0 to D15. It also has connections for ground and +5 volts

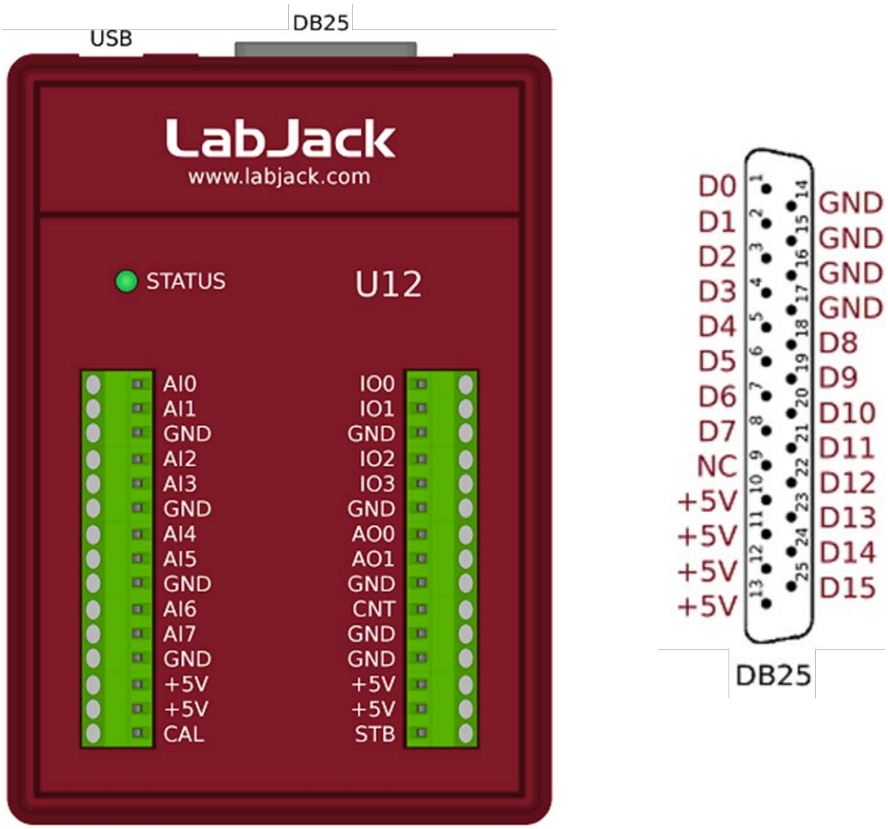

Figure 7.1 – LabJack pinout schematic.
(Right) LabJack U12 top surface with pin out. USB and DB25 plugs shown on the top edge. (Left) Plug DB25 with pin out.

Due to the need of 9 digital output pins and an analogue voltage reader, the LabJack U12 was chosen as the control unit to completely monitor and control the thermal cycles in this project.

7.2. Heaters

The heater chosen was a patch heater. which consists of an electrical resistance element between two flexible insulating materials, such as Kapton. The one used for this project was a Kapton Heater from OMEGA Engineering. Inc model number KHLV-102/10 [22].

Due to the high temperatures achieved a patch heater without PSA must be used. Therefore, the need to use a fixation method, that uses small aluminium caps. In Figure 7.2 a patch heater is attached to the aluminium cap before installation.

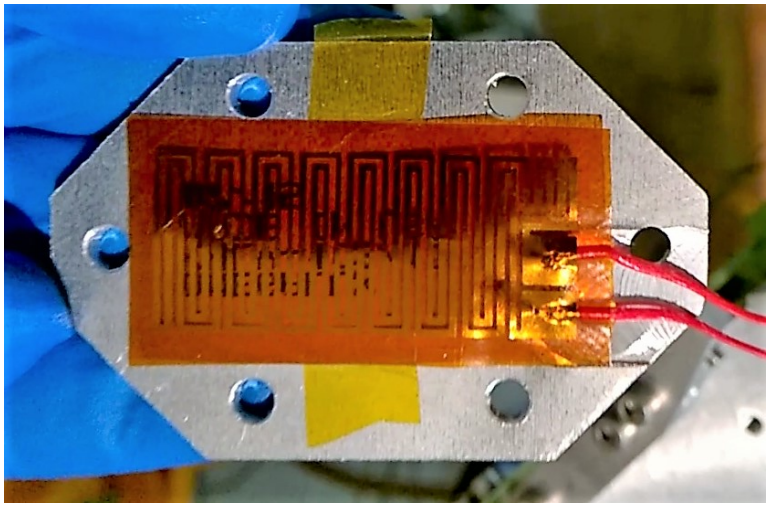

Figure 7.2 – Omega patch heater attached to the thermal fixation before installation.

This patch heater has 3x5 cm^2, operating at 28V and with a power of 20 Watts. A total of six heaters were installed, with a combined power of 120 W, each heater can be control independently through the Control Board (complete description in section 7.4) in order to allow a fine control of the backplate temperature.

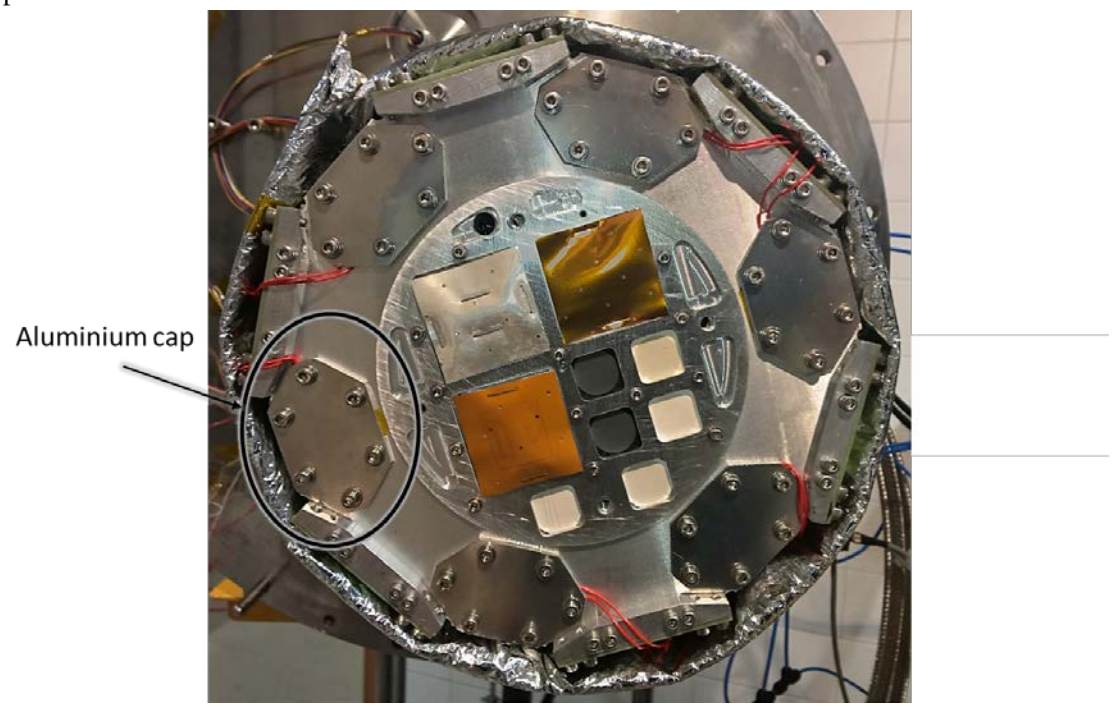

Figure 7.3 – Location of the heat patches on the back plate

7.3. Mechanical switches control

The mechanical switches use air operated cylinders in order to create a linear movement. The air compact cylinder option was chosen over a, for example, a stepper motor, because in order to achieve a good thermal contact, it is needed a good pressure (as well as, a roughness, a waviness and a flatness surface). So controlled variable is the pressure and not the position.

The pressurized air direction is controlled by solenoid valve. The circuit diagram is depicted in Figure 7.4. For this application, the ADN-16-10-I-P-A compact cylinder form FESTO was used [29]. it has a piston diameter of 16 mm and a stroke of 10 mm. The valve is single solenoid with a 90 l/min flow rate and operates at 24 V. Both the cylinder and the valve have a maximum operation pressure of 10 bar.

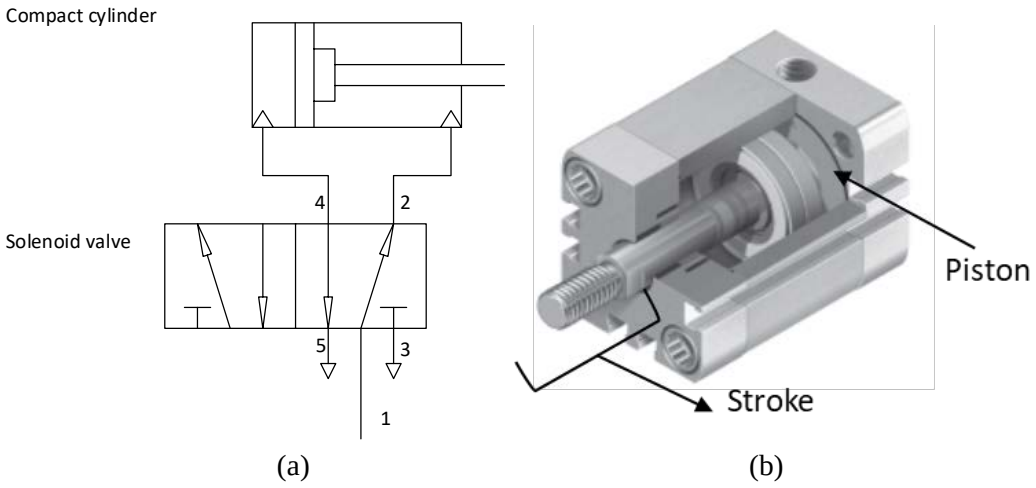

Figure 7.4 – Compact cylinder and solenoid operation description.
(a) Circuit diagram of the solenoid valve and the compact cylinder. (1) – Air input; (2) – Air output to push the piston; (3) (5) – Venting ports with silencers; (4) Air output to pull the piston; (b) Section view of the compact cylinder.

There are three mechanical switches in the TVC system; each one is composed with a compact cylinder and a solenoid valve. The control of each solenoid is made through the Control Board (description in the section below).

7.4. Control Board

The digital signals from the control unit (LabJack U12) needed to be converted to operating voltage of the heat resistors and the pneumatics. Also, solid-state relays were employed in order to electrically isolate the circuits. A solid-state relay consists on an infrared LED input stage optically coupled to an output detector circuit. The detector consists of a high-speed photovoltaic diode array and driver circuitry to switch on/off two discrete high voltage MOSFETs.

To control the pneumatics driver, a low current and dual channel solid-state relay was used. the Avago ASSR-1228. Alongside, for driving the heat resistors. the VO14642AT from Vishay Semiconductors was used. providing a maximum load up to 2A in DC.

Envisaging the independent control of the heating resistors and the pneumatics, six solid state relays from a Vishay and two from Avago were used, respectively. Figure 7.5 shows the schematic of the Control Board.

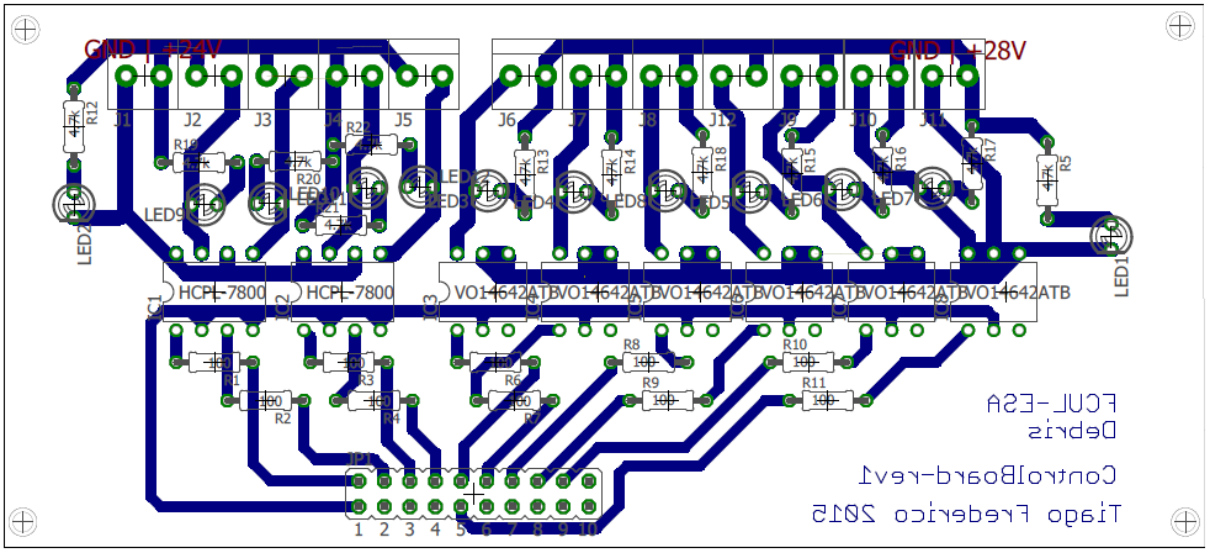

Figure 7.5 – Schematic of the Control Board.

The Control Board was designed using CadSoft Eagle with pcb-gcode, a freeware plugin that converts the Eagle design into g-code, so it can be interpreted by a CNC milling machine. This technique doesn't use a chemical process, as in the UV lithography, instead, areas of copper are removed from the sheet to create pads, traces and patterns according to the layout file. After the milling process a very thin layer of tin is deposited, for the purpose of protecting the copper from oxidation.

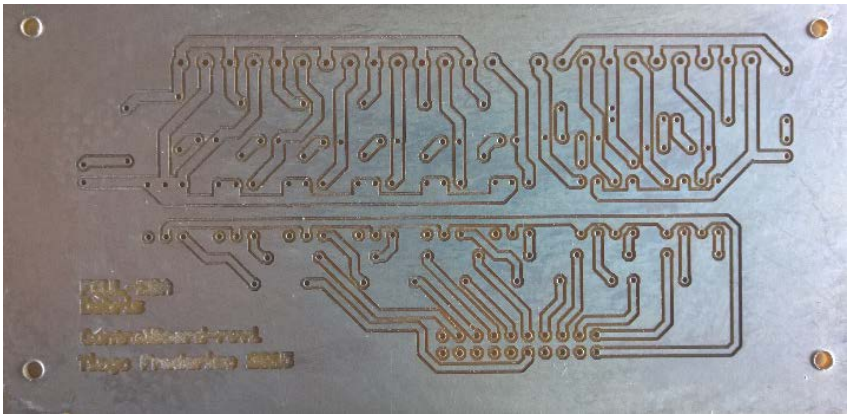

Figure 7.6 – PCB after the milling and after depositing a very thin layer of tin.

Figure 7.7 – Board Control final result. All components soldered and operational.

The Figure 7.7 displays the Board Control already fully operational. On the left side of the board, the six solid state relay for the heater resistors, each green LED represents the logical state of the relay. The two IC on the right side are the 4 relays for the pneumatic control (only three are in use). As in the left side, the four blue LEDs represent the logical state of each relay. The red and yellow LEDs are the power indicator of the 24 and 28 volts power supplies, respectively.

7.5. Temperature Acquisition

A PT100 platinum resistance thermometer was used instead of a standard temperature sensor, such as the LM35, due to the low temperatures reached in a normal thermal cycle. A PT100 is a sensor with a temperature-dependent electrical resistance, which increases with the temperature and therefore is known as a PTC (positive temperature coefficient). Platinum resistance thermometers offer excellent accuracy over a wide temperature range from –200 to +650 °C. For a PT100 sensor, a 1 °C temperature change causes a 0.384 Ω change in resistance, so even a small error in measurement of the resistance (for example, the resistance of the wires leading to the sensor) can cause a large error in the temperature measurement. For precision, a four wire scheme is usually used - two to carry the sense current, and two to measure the voltage across the sensor element.

Figure 7.8 –OMEGA CN7800 front side.

The CN7800, from OMEGA Engineering. Inc [24] was used as an off the shelf temperature monitor since it measures the PT100 resistor using the four wires. The acquired temperature readings were transmitted through RS-485 protocol. All data is send and received in the ASCII HEX character format

using 10 bits. It is necessary to add a checksum to the end of the message; this checksum is calculated by adding all the ASCII characters in HEX.

Each OMEGA controller had his own SERIAL port, which meant that the command for reading the cloud to be the same thus. changing only the communication port. In Figure 7.9 is the LabVIEW program developed to read temperature. Also, with the possibility for using the other functions of the OMEGA controller, a checksum program was developed (Figure 7.10).

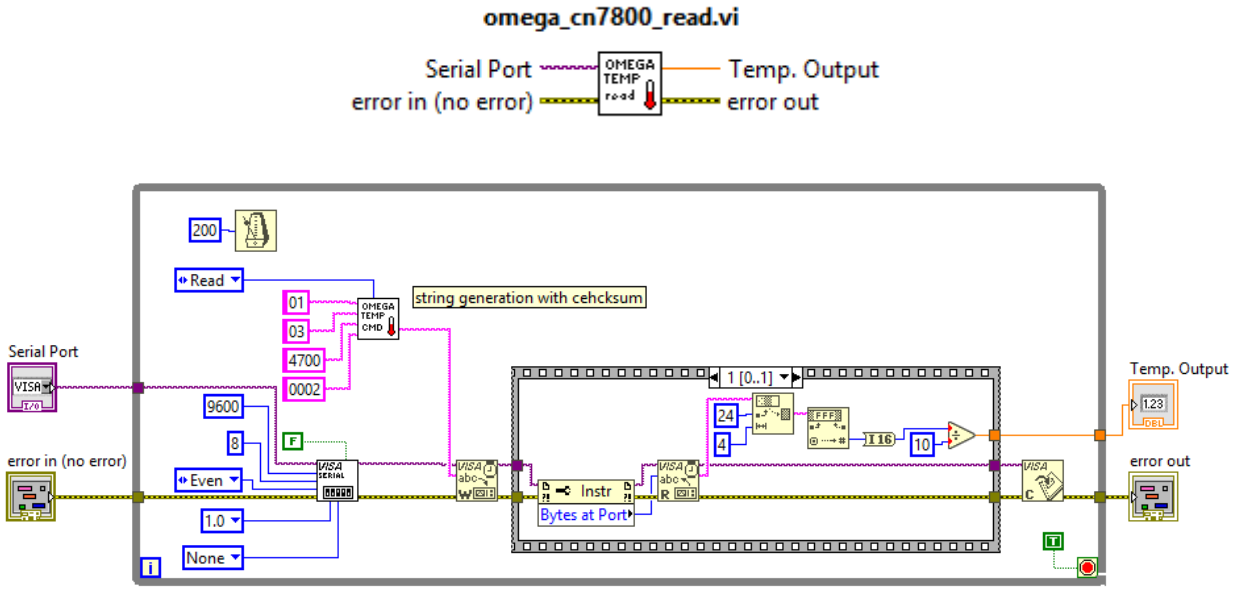

Figure 7.9 –OMEGA CN7800 read temperature LabVIEW block diagram.

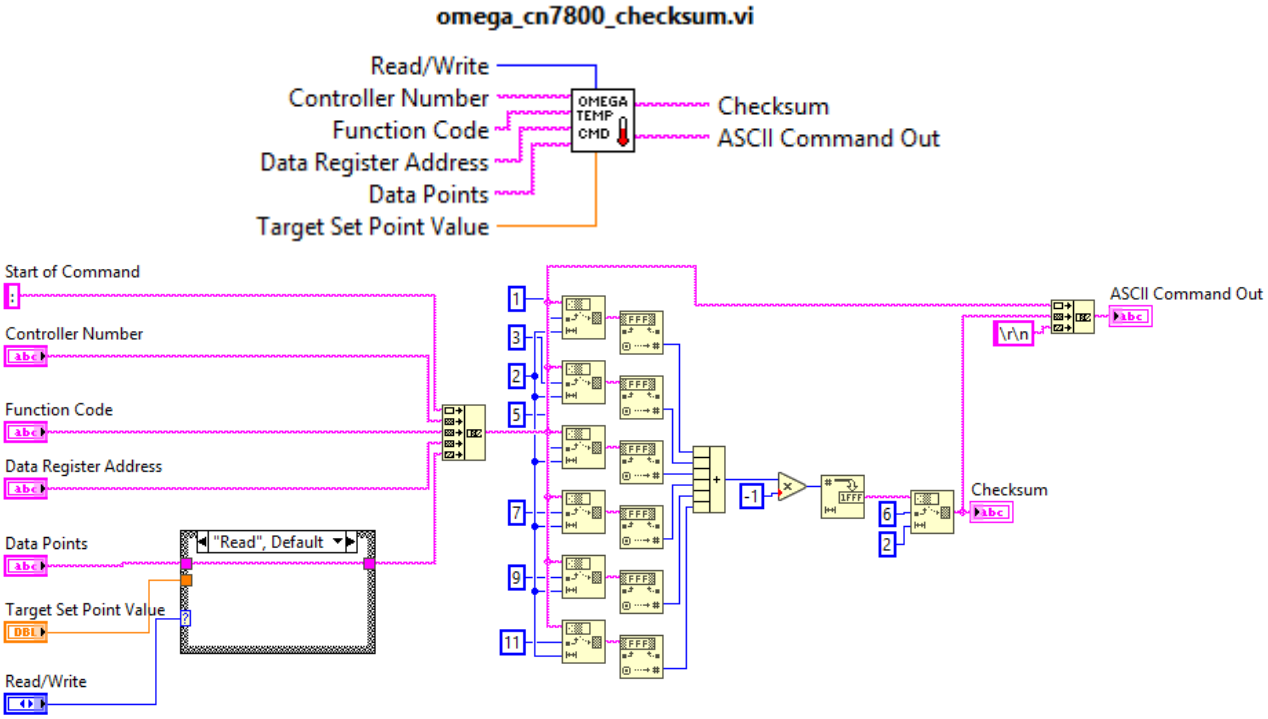

Figure 7.10 –OMEGA CN7800 checksum calculator LabVIEW block diagram.

7.6. Vacuum Pressure

The monitorization of the pressure inside the chamber is essential for any vacuum related experiment. In this case, even more essential due to the existence of moving bellows and a high possibility of outgassing due to high temperatures in the thermal cycle.

The Edwards WRG-S vacuum gauge, which was used, has an analogue output with pressure proportional voltage. The LabJack analogic channel measures the output voltage and it is converted into mbar pressure units through the following expression:

$$P = 10^{(1.5V-12)}$$

7.7. Cryocooler and Cryocooler Monitor

The cryocooler used was from *Advanced Research Systems* (ARS) company with a ARS-4HW compressor and a DE-104(T) cold head [23]. The cooling capacity of the cryocooler is temperature depended as shown in Figure 7.11.

During the thermal cycles, the heat load on the cold head goes from about 40 W, when the temperature at the clod head is minimum (around 60 K), to 70 W at the maximum temperature of about 115 K.

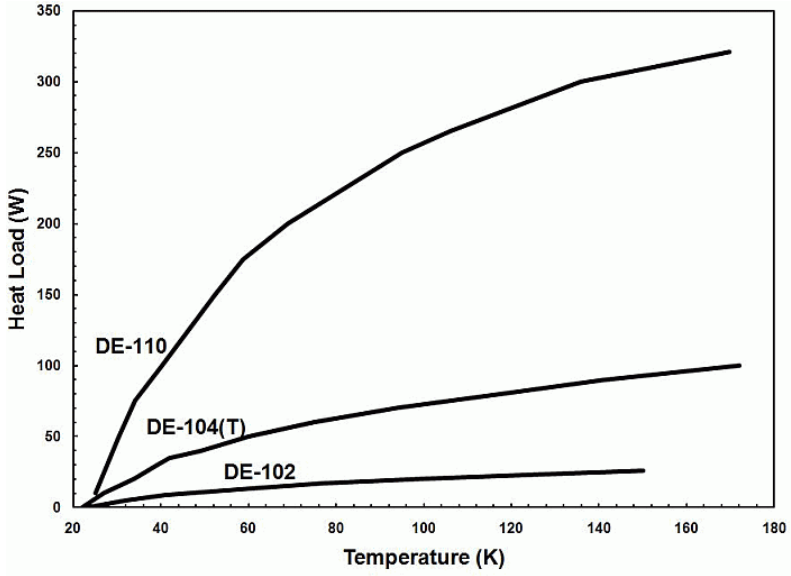

Figure 7.11 – Heat map load of the cold head DE-104(T) from ARS.

For long running-time systems a remote monitor solution is needed to ensure the smooth operation of the experiment. Since this cryocooler does not have any supervisor system for the water flux and temperature, a custom solution was developed. The water used to cool the compressor must not be over 35 °C at the output.

The water flow sensor is a plastic valve body with rotor that provides a Hall effect sensing when water flows through the motor. As liquid passes through the valve and the magnetic rotor spins, at a rate proportional to flow, the resulting magnetic field stimulates the hall effect sensor, producing a series of voltage pulses. An NTC 10k was used to read temperature since the water temperature's range goes from 20ºC to 50°C and consequently falling into the working range of the sensor.

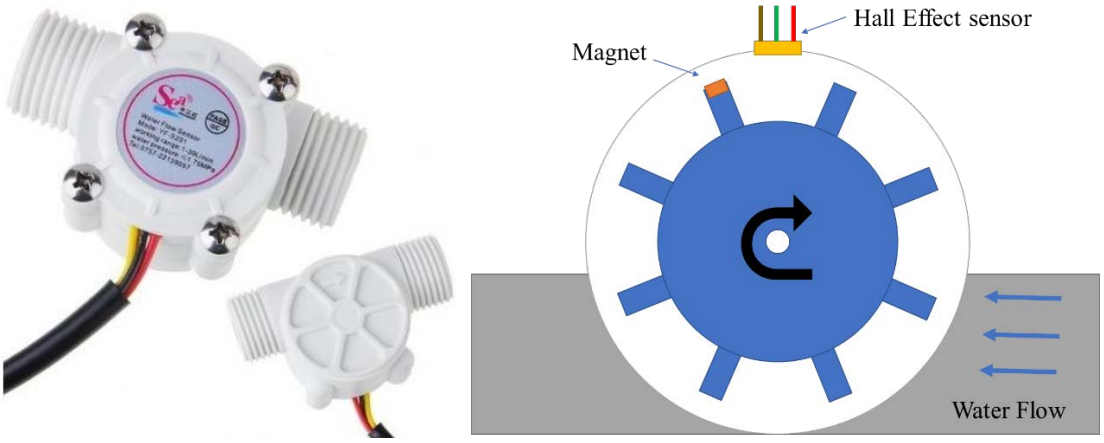

Figure 7.12 – (Left) Water flow sensor exterior (Right) Water flow sensor internal mechanisms

The best option in terms of firmware developing time and availability was to use an ATmega328 microcontroller on a development board. The ATmega328 accepts external interruptions, which are essential to count the number of pulses from the water flow sensor and it has several ADC ports for analogue readings, such as, the temperature signal. The acquired data is sent through UART to be displayed in the control station or to send warnings.

Besides the data sent through UART another three warning lights were also installed: a green, a yellow and a red LED. The green is associated with the flow, the yellow and red to temperature. The following table describes the warning lights system.

Table 7.1 –Warning lights system description

Code	Description
3 lights flashing four times	Initializing
3 lights flashing continuously	No water flowing
Green fix	Water flow within 2.4 and 2.6 L/min
Yellow and Red off	Water temp. bellow 30 °C
Yellow on and Red off	Water temp. within 30 and 35 °C
Yellow off and Red on	Water temp. within 35 and 37 °C
Yellow and Red altering	Water temp. over 37 °C

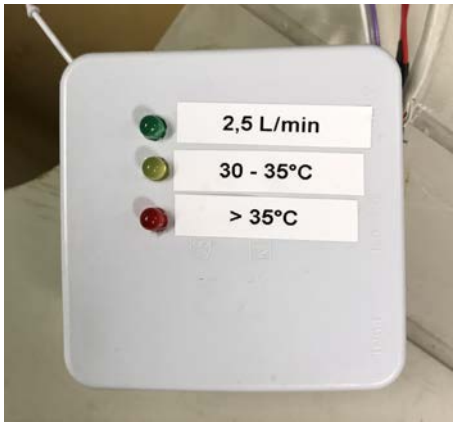

Figure 7.13 – Warning lights system

The code used for the firmware of the ATmega328 is on Appendix C.

7.8. LabVIEW Interface

The user interface was developed in LabVIEW, to display the information gathered from the sensors above mentioned and the status of the actuators, i.e. the patch heaters and the pneumatic actuators.

The Figure 7.14 shows a complete view of the Control Panel. The complete LabVIEW block diagram is displayed in Appendix F.

A. This panel displays the current temperature in each one of the five PT100 installed.
B. Actuators Control Panel. This panel consists in an *Override* and a matrix of buttons that allows to control and to know the state (ON/OFF) of an actuator. The matrix is divided into 3 columns: the first with red buttons, the second with blue buttons and the third with green ones, representing respectively:
    i. User manual input. that can override the automatic control if the *Override* button is toggled ON;
    ii. The automatic control input;
    iii. The state of the output to the Control Board.
C. Display the temperature over time.
D. Stage Control Panel. As mention on section 3.3, there are four stages on a normal thermal cycle. Although, due to functionality reasons two more were added. An *OFF* stage where all automatic controls are disabled and a *Warnup - 45 °C* stage, which is used to ensure a secure temperature for opening the system without formation of ice inside the chamber. Those two stages are only assessable through the *Stage Override* button. In this panel. it is also possible to define the Upper and Lower temperature limits, as well as the Dwelling times for each one individually.
E. Displays the current pressure inside the chamber.
F. Displays the data capture from the Cryocooler and Cryocooler Monitor, described in section 7.7.
G. System Alert Panel. Advises the user if some parameters, i.e. the cryocooler temperature, water flow, cold finger temperature and vacuum pressure, are outside normal values. This warning is represented by the red-light present in this panel, as well by sending a text message to a pre-defined cell phone number and it also displays the number of cycles already done.
H. Reading from a UV sensor.[9]

[9] Not in the scope of this thesis. See more on [39]

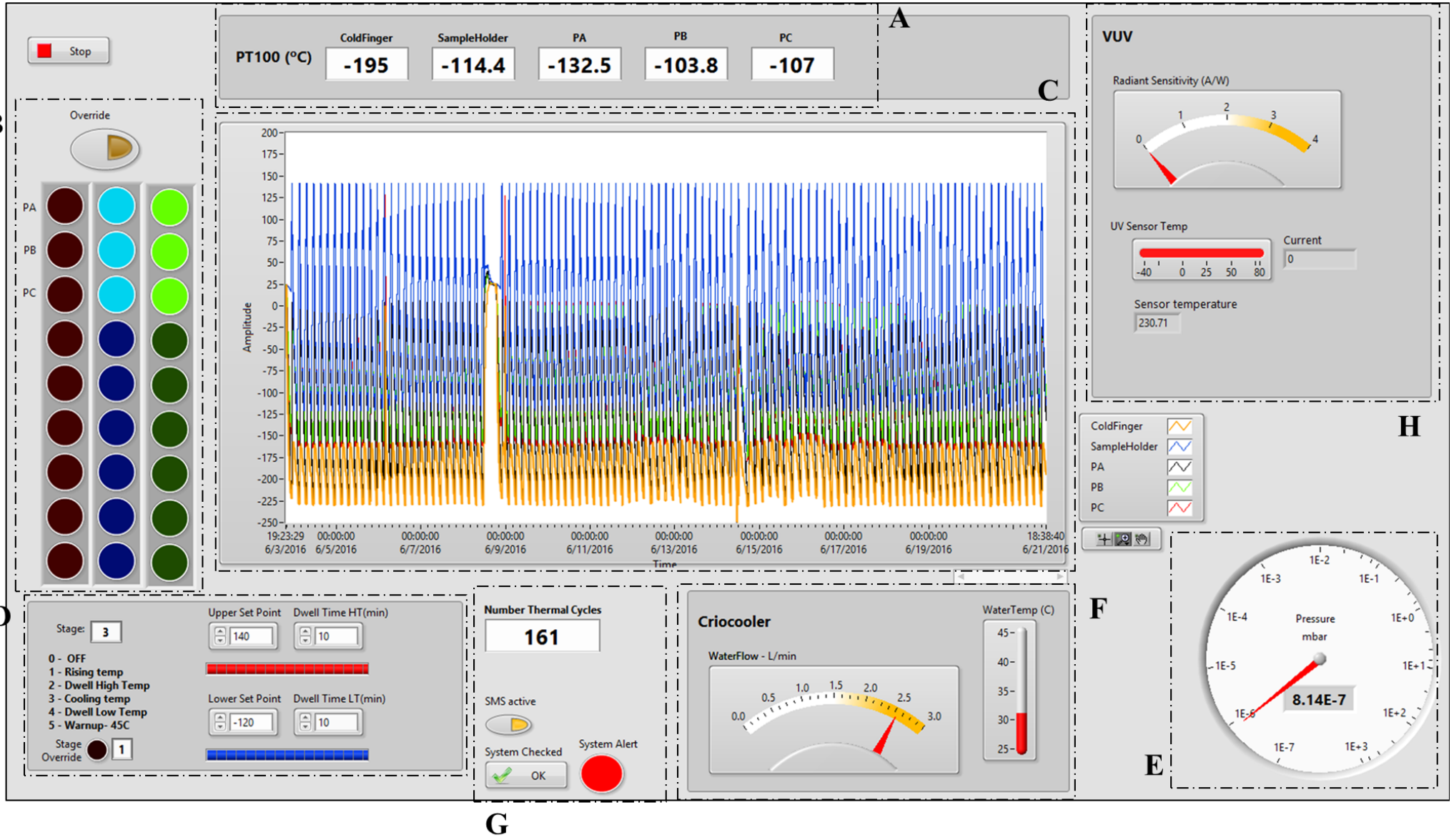

Figure 7.14 – Interface of the Control Panel

7.9. Data logger

In order to keep all the information collected and stored over long periods of time, the data from all sensor and all actuators is saved into a file with the starting of the program as a timestamp filename.

- Time;
- Pressure;
- PA (temperature on piston A);
- PB (temperature on piston B);
- PC (temperature on piston C);
- SampleHolder (temperature on the back of the baseplate);
- ColdFinger (temperature on the cold finger);
- Piston (a binary representation of the state of the three pistons);
- Resistor (a binary representation of the state of the six resistors);
- UVCurrent;
- Water Temp;
- Water Flow.

8. Performance and Optimization

8.1. Thermal Characterization

In Figure 6.4, it is possible to see the location of the temperature sensors in the tip of the pneumatics, on the cold finger and on the sample holder.

To execute the thermal characterization. several full cycles are performed. in which the temperature of the sensor is recorded. The beginning of the HTD stage is the start of a new cycle.

Figure 8.1, is represented a full cycle with a temperature range from +150 to -150 °C. In yellow is the temperature of the base plate and in blue, the cryocooler. The other three lines, PA, PB and PC. in green, orange and grey, respectively, are the temperatures of the pistons during the cycles. These last three sensors display different values due to a variety of factors, including different wire length, meaning the compensation of the PT100 is off, bad thermal connection between the piston and the sensor.

A better look at the Cooldown, represented by ***B*** in Figure 8.1, it is possible to, roughly, create two linear zones, representing two different mechanisms of cooling. In ***b1***, the cooling process is dominated by the thermal mass of the copper pistons, and in ***b2***, the heat transfer is depending on the copper straps. The cooling down rates are -5.8 °C /min and -0.8 °C/min to ***b1*** and ***b2***, respectively.

The Warn Up, ***D*** in Figure 8.1, has a heat rate of +5.6 °C /min. The heating of the system is achieved only with the 100 W kapton resistors.

It is possible to observe that each cycle with this temperature range takes about 7 hours to complete. Those tests were not performed with the full mass load, i.e. the sample holder and the samples were missing, meaning the times per cycle would only increase Other temperatures ranges were tested. The following table resumes the time per cycle in the different temperatures range.

Table 8.1 – Summary of the time need to complete each cycle with different temperature ranges

Temperature Range	Cycle Duration
+150/-150 °C	6h51min
+120/-120 °C	3h36min
+100/-100 °C	2h48min

The system suffered some changes between the conceptual part and this characterization. Due to some an adjusts needed in the VUV subsystem. The epoxy isolators were extended from 158 to 308 mm in the inner and 240 to 415 mm in the outer. The rest of the system remains the same. This is the reason the why the simulated times differ from the tested. Other options needed to be considered.

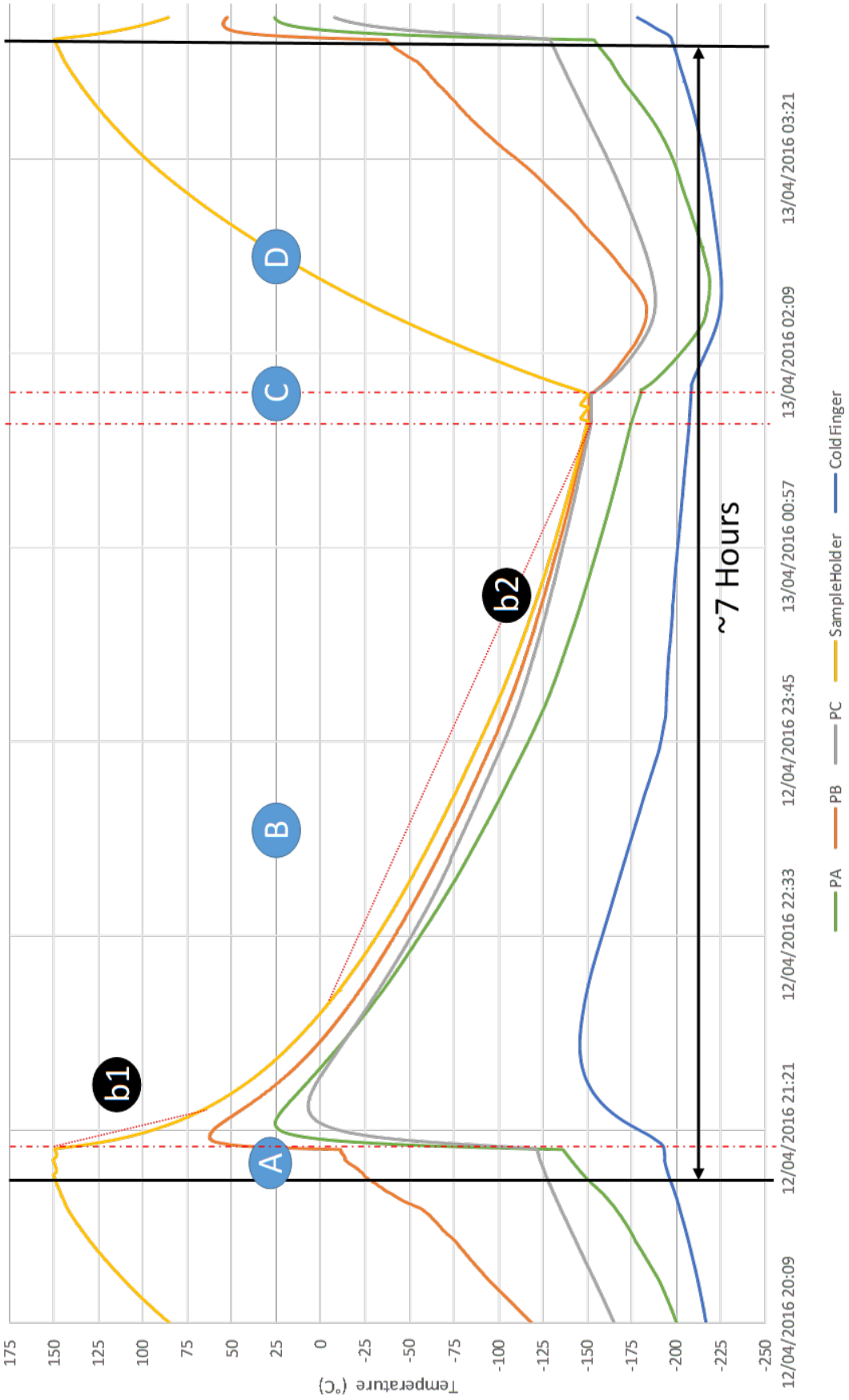

Figure 8.1 – Thermal cycle with temperatures from +150/-150 °C.
A - High Temperature Dwelling; B- Cool Down; C - Low Temperature Dwelling; D - Warn Up

8.2. Optimization

Concerning the number of cycles necessary and the time required to execute the project, a solution where the sample holder was merged with the baseplate was achieved, resulting in mass reduction. Also, the thickness of the aluminium piece that hold the kapton resistors was reduced. The total mass, of the sample holder merged with the baseplate, is now less 1.37 kg, when it was 2.14 kg. Meaning a 40% reduction.

In Figure 8.2 is a 3D representation of the baseplate, in which pockets were made, with different depths.

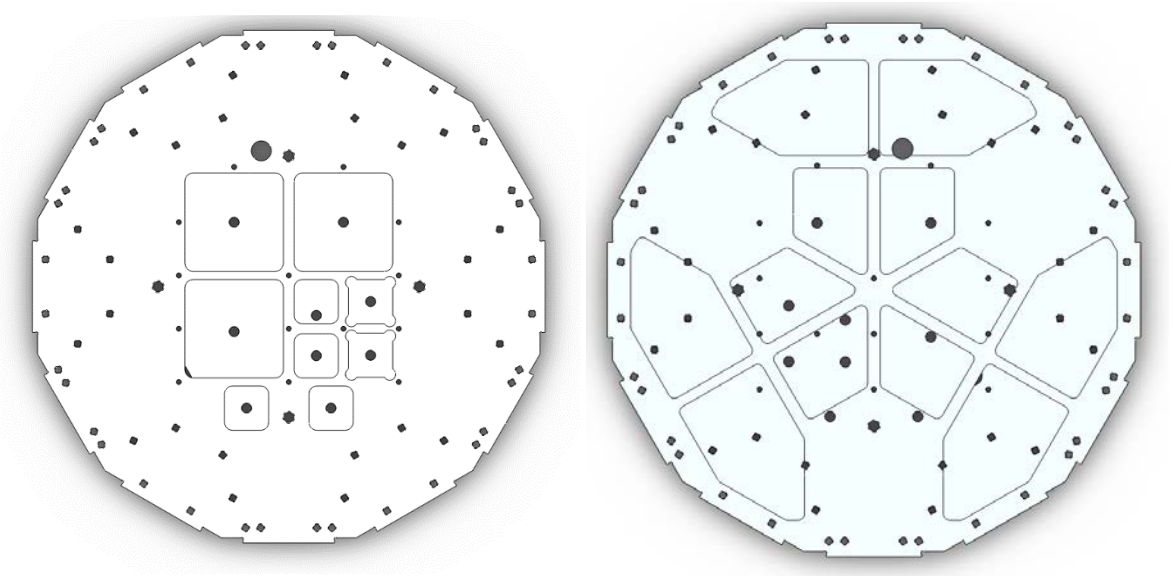

Figure 8.2 – On the left side is the front side of the base plate. in which the samples will be places. as well as the heat resistors. On the right. are shown the pockets on the back side.

In the process of reducing the mass, there are compromises between the extract material, the thermal conductivity and deformation of the material due to the temperature ranges. To address this concern, two finite element analyses were performed, one to observe the thermal gradient and the other the displacement. Both studies were retrieved from a transient study, where the whole base plate was at +150°C and then was applied -150°C to the areas where the pistons touch the base plate. In Figure 8.3, on the top plot, it is possible to see that the thermal gradient appears to be uniform despised the reduction on the section area. On the bottom plot. the maximum displacement is less than 200 µm.

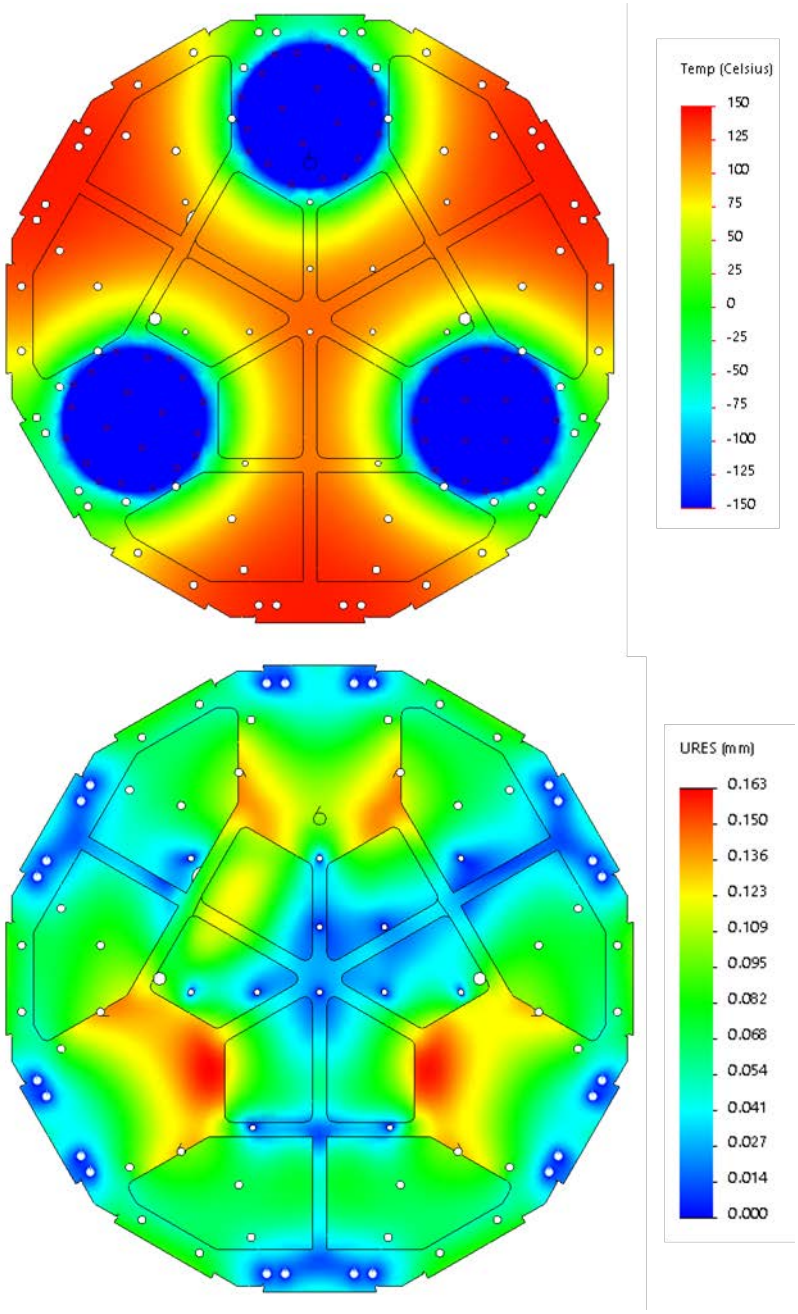

Figure 8.3 – On top. plot temperature gradient on the base plate. On bottom. deformation based on the same temperature gradient as the top plot.

Base on this simulation, a new base plate was produced. It is shown already assembled on the vacuum chamber for a new characterization in Figure 8.4

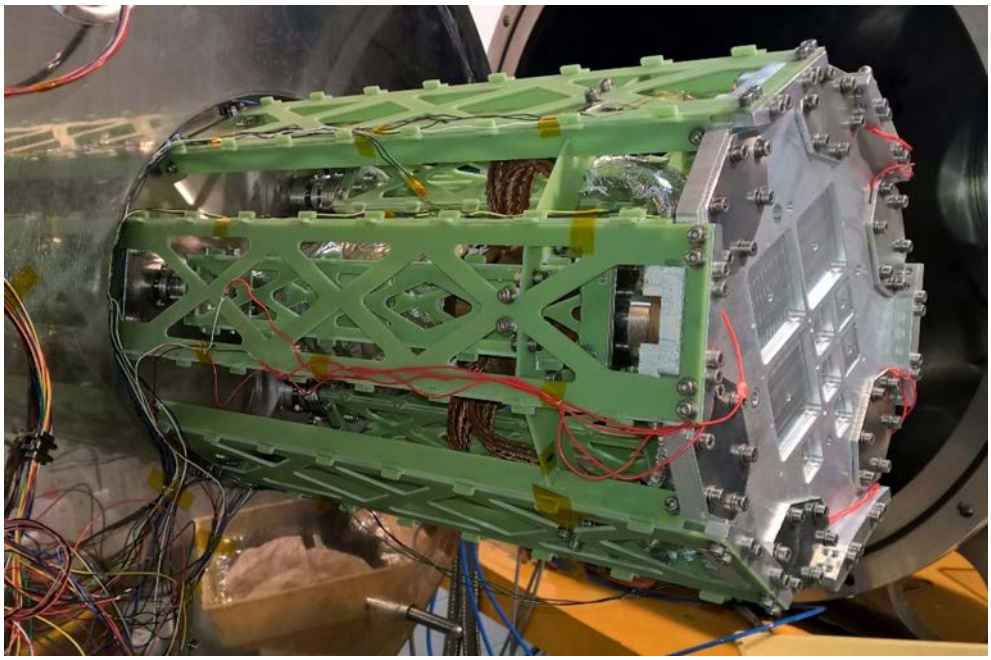

Figure 8.4 – Section view of the final design for the thermal vacuum cycle sub-system.

The process used in the first characterization and with a similar set of temperatures ranges was repeated with the new base plate. The Figure 8.5 shows a plot analogous to the one in Figure 8.1 but with a smaller period. The results are summarized in the table below.

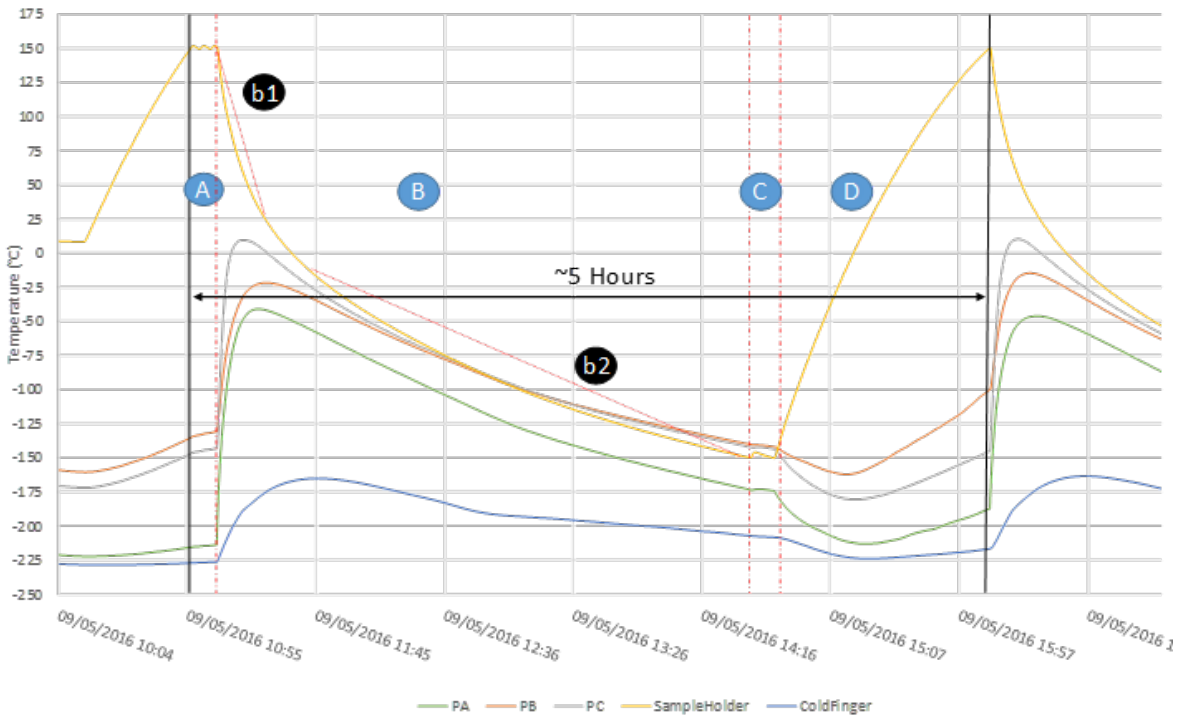

Figure 8.5 – Thermal cycle with temperatures from +150/-150 °C.
A - High Temperature Dwelling; B- Cool Down; C - Low Temperature Dwelling; D - Warn Up

Table 8.2 - Summary of the time need to complete each cycle with different temperature ranges

Temperature Range	Cycle Duration
+150/-150 °C	6h09min
+140/-140 °C	3h56min
+120/-120 °C	3h18min

8.3. MLI Thermal Characterization

Since the purpose of this project is to simulate the space condition on a LEO, it is essential to know the temperature that the samples are exposed, which may not be the same as the base plate.

The thermal characterization of the system was performed in the same time as the characterization of the MLI thermal characterization. In this test, the PT100 from the pistons were replaced by PT100 in some of the layers of the MIL, as described in Figure 8.6. The purpose of these characterizations is to assess the temperatures that different layers' experience during the cycles.

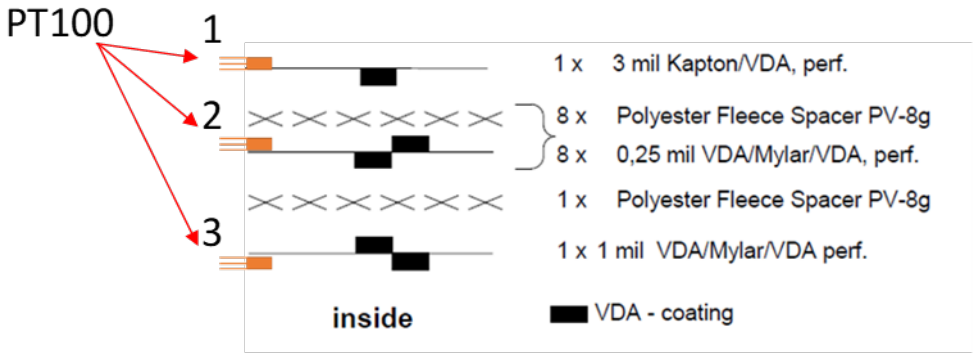

Figure 8.6 – Distribution of the temperature sensor on the MLI sample.
1 – Cover layer; 2 - On the 5th layer (i.e. after the cover + 4th polyester/Mylar set) counting from the top; 3 – In the middle of the Velcro or PSA adhesive depending on the fixation method

This test was the most representative so far. All components were assembled, which meant that all the mass that experience the thermal cycles was present. In the picture below, the MLI samples with the PT100 are already mounted on the base plate.

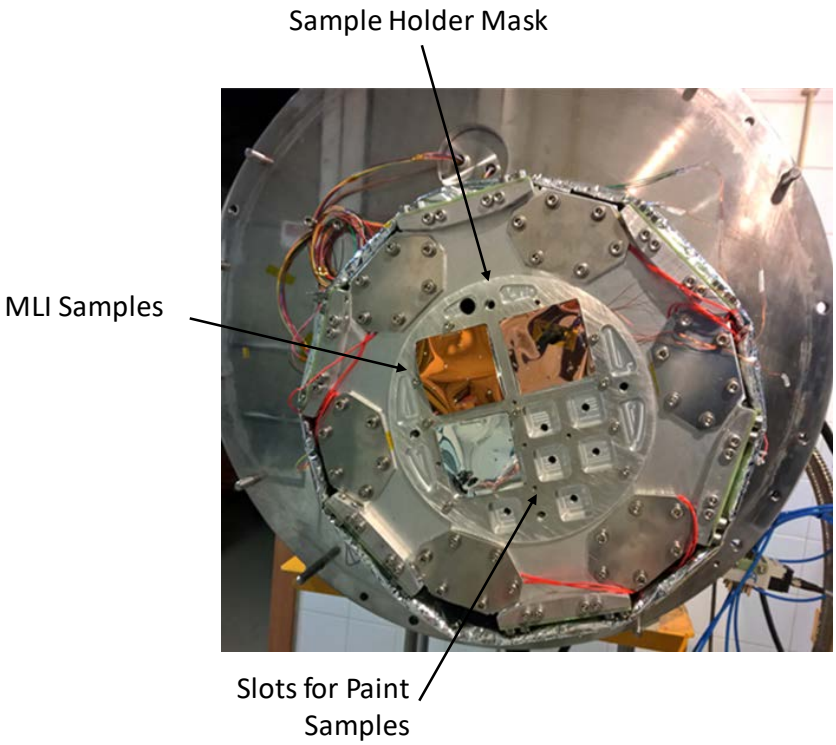

Figure 8.7 – MLI test samples assembled in the sample holder for thermal characterization of the layers

In this characterization, new temperature ranges were tested. Previous results show that lower temperatures (i.e. -140°C or -150°C) can take up to 2 hours more than a limit of -120°C. The different temperature tested are displayed in Table 8.3. It was agreed that +140 to -120 °C would be the best option in terms of period and temperature.

Table 8.3 - Summary of the time need to complete each cycle with different temperature ranges

Temperature Range	Cycle Duration
+150/-120 °C	4h18min
+140/-120 °C	***3h54min***
+140/-100 °C	3h45min

In the figure below, is a plot of the thermal cycle with the chosen temperature range. As this was also a MLI characterization, now the plot shows the 3 PT100 place on the different layers of the sample.

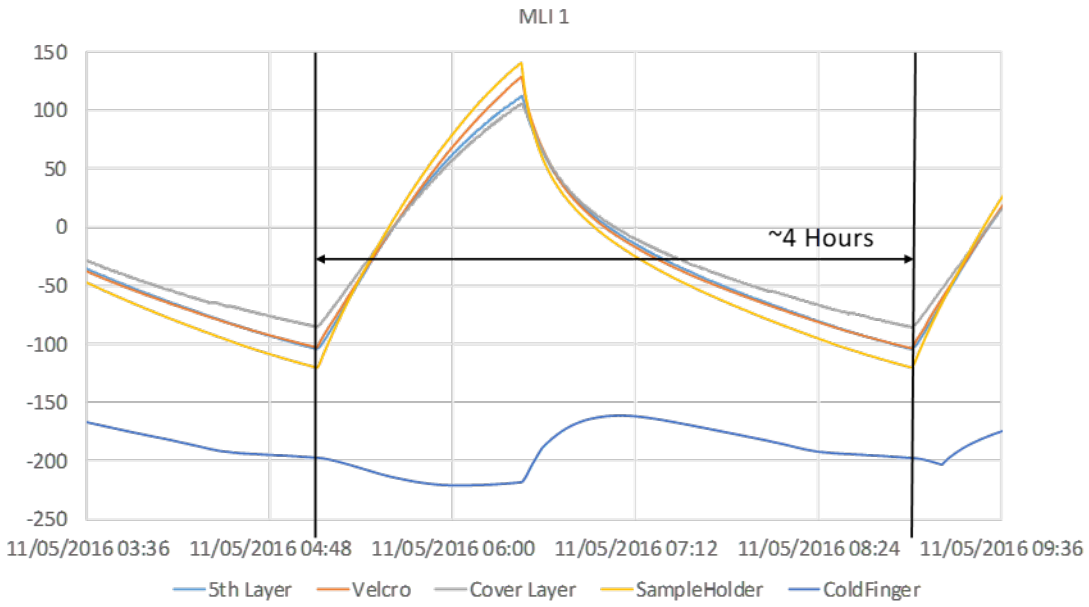

Figure 8.8 – Chosen temperature range. from 140 to -120 °C.

8.4. Acceleration factor

The Coffin-Manson equation [30] is a simple relationship in which cycles to failure is inversely proportional to strain. A modified version of the Coffin-Manson, Landzberg-Norris equation, also includes effects from the frequencies and the maximum temperatures.

The acceleration factor AF for the TVC is dependent on the material selection. This dependency is expressed as material parameter b. m and C:

$$AF = \frac{N_O}{N_t} = \left(\frac{t_O}{t_t}\right)^b \left(\frac{\Delta T_t}{\Delta T_O}\right)^m \exp\left[C\left(\frac{1}{T_{O.Max}} - \frac{1}{T_{t.Max}}\right)\right] \quad (13)$$

The used variables are:

- N_O – Number of cycles survived under operating conditions;
- N_t – Number of cycles survived under test (laboratory) conditions;
- b – Cycling frequency exponent (material specific);
- m – Temperature range exponent (material specific);
- C – Constant coefficient (material specific);
- t_O – Period of thermal cycles under operating conditions;
- t_t – Period of thermal cycles under test (laboratory) condition;
- ΔT_t – Max. change in temperature during the cycle under operating conditions;
- ΔT_O – Max. change in temperature during the cycle under test (laboratory) conditions;
- $T_{O.Max}$ – Maximum temperature experienced under operating conditions;
- $T_{t.Max}$ – Maximum temperature experienced under test (laboratory) conditions.

The parameters b. m and C are empiric values for different materials. For SnPb typical values lie around $b \approx -\frac{1}{3}$ $m \approx 2$ and $C = \frac{E_a}{K}$ where E_a is the activation energy of the subject material and K the

Boltzmann constant. [31,32,33,34,30]. If the testing maximum test temperature ($T_{t.Max}$) is close the real scenario ($T_{O.Max}$). the exponential in (13) is equal to 1.0 regardless of C.

So, for the operation parameter, a typical LEO mission is considered, with 90 minutes orbiting period, a maximum temperature of 100 °C and a range of 200 °C. For the test parameters, the cycle duration is 240 minutes, the maximum temperature of 140 °C and a range of 260 °C. These parameters are summarized in the following table.

Table 8.4 - Summary of the parameters used in the Acceleration Factor calculation.

Parameter	Operation	Test
Period of thermal cycles (min)	90	240
Maximum temperature (°C)	100	140
Max. change in temperature (°C)	200	260

Assuming the above scenario, the Acceleration Factor obtained is, approximately, 2.384.

9. Conclusion and future developments

Spacecraft materials exposed to Earth orbit environments have been found to undergo degradation or damage due to environmental threats including atomic oxygen, contamination, radiation, temperature effects and temperature cycling, and micrometeoroids and orbital debris. The degree to which the space environment degrades or damages materials depends upon the unique conditions of an individual spacecraft environment and the susceptibility of the material to being altered by these environmental exposures. Accurately predicting the behaviour of materials in these complex space environments is important to the success of space missions yet can be difficult to accomplish.

A spacecraft on a low Earth orbit experiences thermal cycles form -100°C to 100°C, within a period of 90 minutes. The thermal cycling under vacuum conditions have a relevant impact on the lifetime of the spacecraft materials, and to studies those impacts a space environment simulator is needed.

The main purpose of this work was to design, to develop and to test a system that would be able to simulate the thermal cycles that the materials on the surface of a space vehicle experience, while in low Earth orbit, performing within the time and temperatures proposed to ESA.

The architecture of this space simulator is based on a helium cryocooler as a heat pump and a mechanism that allows the cold part to be engaged and released from the base-plate, denominated Mechanical Thermal Switch. A custom made electronic control box was developed, allowing the control of the heating resistors and the solenoid that controls air flow into the pneumatic of the Mechanical Thermal Switch. To governor the environment simulator, a control software based on LabView was developed. It implemented the control needed to achieve a thermal cycling, besides providing the user with a graphical interface, it gathers information from several sensors.

A fully working thermal vacuum cycling system was constructed. Although, the initial -150 to +150 °C was not possible, due to long duration cycles, a compromise between range/duration was achieved. With the optimization of the base plate and the exchanging temperature range it was possible to reduce about 3 hours of its initial 7 hours. The final temperatures were -120 °C for the lower limit and 140 °C for the higher limit.

To make this feasible in a realistic time frame, an accelerating factor 2.3 was introduced by enlarging the temperature variation. A major constrain comes from the copper brads that limited the heat transfer, increasing the duration of a cycle. A bigger section of the brads or a short length could not be implemented due to systems constrains.

A complementary solution to decrease the thermal load on the cryocooler and the cooldown duration would be using a closed circuit with water. A capillary tube with water would circulate in the back of the baseplate and the warm water would be transferred to a large reservoir to thermalize at room temperature. This system would be used immediately after the high temperature dwelling and would take the heat until the base plate temperature be around 30 °C, then the water would be extracted and the pistons engaged continuing the cooldown until reaching the lower temperature limit.

Nevertheless, with a lower limit of -120 °C and a higher limit of 140 °C and a duration of, approximately, 4 hours, the system has executed the 500 thermal cycles proposed to ESA in three months.

10. References

[1] Flegel S et al., "THE MASTER-2009 SPACE DEBRIS ENVIRONEMENT MODEL ," in *5th European Conference on Space Debris*, Darmstadt, Germany , 2009.

[2] Edwar M. Silverman, *M.,"Space Environmental Effects on Spacecraft: LEO Materials Selection Guide*.: NASA, 1995.

[3] R.L. Kiefer et al., "Space environment effects on polymeric materials,".

[4] V. I. Pavlenko, "EFFECT OF RADIATION ON GLASSES IN BOROSILICATE AND BORON-LEAD-SILICATE SYSTEMS," *Glass and Ceramics*, vol. 59, 2000.

[5] L.B. Fogdall et al, "Space Radiation Effects of simulated venus-mercury fly-by on solar absorptance and transmittance properties of solar cells, coverglasses and adhesives,".

[6] M. Moser et al., "Telescope Solar Arrays Surface and Bulk Degradation of Teflon® FEP Retrieved from the Hubble Space," *High Performance Polymers 2008.*

[7] Townsend J. et al., "Degradation of Teflon FEP Following Charged Particle Radiation and Rapid Thermal Cycling," in *20th Space Simulation Conference: 201-209 (NASA/CR- 1998-208598-Preprint)*.

[8] Joseph W. Chamberlain, *THEORY OF PLANETARY ATMOSPHERES, An Introduction to Their Physics and Chemistry*, ACADEMIC PRESS, Ed. Houston, Texas, USA: Department of Space Science and Astronomy , Rice University.

[9] Richard L. Kiefer and Robert A. Orwoll, "SPACE ENVIRONMENTAL EFFECTS ON POLYMERIC MATERIALS," 1987.

[10] David G. Gilmore, *Spacecraft Thermal Control Handbook, Volume I: Fundamental Technologies*. El Segundo, California: The Aerospace Press.

[11] Devarakonda Angirasa and Portonovo S. Ayyaswamy, "Review of Evaluation Methodologies for Satellite Exterior Materials in Low Earth Orbit," 2013.

[12] Anvari A, Farhani F, and K.S. Niaki, "Comparative Study on Space Qualified Paints Used for Thermal Control of a Small Satellite," *Iranian Journal of Chemical Engineering*, vol. 6, no. 2, 2009.

[13] A.Horstmann and E.Stoll, "Investigation Of Propagation Accuracy Effects With In The Modeling Of Space Debris," in *7th European Conference on Space Debris, Darmstadt, Germany*, 2017.

[14] National Research Council, Division on Engineering and Physical Sciences, Aeronautics and Space Engineering Board, Committee for the Assessment of NASA's Orbital Debris Programs, *Limiting Future Collision Risk to Spacecraft: An Assessment of NASA's Meteoroid and Orbital Debris Programs*.: National Academies Press, 2011.

[15] Paula Krisko, Sven Flegel, M.J. Matney, D.R. Jarkey, and Vitali. Braun, "ORDEM 3.0 and MASTER-2009 modeled debris population comparison," *Acta Astronautica*, vol. 113, 2015.

[16] Sven K. Flegel, Johannes Gelhaus, Marek Mockel , Carsten Wiedemann, and Holger Krag, "Multi-layer insulation model for MASTER-2009," *Acta Astronautica*, 2011.

[17] RUAG, Space Division, Thermal Insulation Products.

[18] Rowe D. M. and Bhandari C. M., *Modern Thermoelectrics*.: Reston Publisinhg Company, INC.

[19] Heat pipes Operating Temperature Range. [Online]. https://www.1-act.com/operating-temperature-range/

[20] M. Dietrich, A. Euler, and G. Thummes, "A compact thermal heat switch for cryogenic space applications operating near 100 K," *Cryogenics*, 2013.

[21] Pedro Carvas de Sousa, "A infra-estrutura de teste da câmara multi-telescópio do GRAVITY," 2012.

[22] Kapton Insulated Flexible Heaters. [Online]. http://www.omega.nl/pptst/KHR_KHLV_KH.html

[23] [Online]. http://www.arscryo.com/single-stage-cryocoolers.html

[24] CN7800 Series. [Online]. http://www.omega.com/pptst/CN7800.html

[25] Leslie Lamberson, Jamie Kimberley Dan Casem, *Dynamic Behavior of Materials, Volume 1: Proceedings of the 2016 Annual Conference on Experimental and Applied Mechanics*.: Springer, 2016.

[26] Harrie Tilmans, "Equivalent circuit representation of electromechanical transducers: I. Lumped-parameter systems," *Journal of Micromechanics and Microengineering* , vol. 6, no. 157, 1996.

[27] John J. D'Azzo and Constantine H. Houpis, *LINEAR CONTROL SYSTEM ANALYSIS AND DESIGN WITH MATLAE*.

[28] Tony Abbey. Accuracy and Checking in FEA, Part 1. [Online]. http://www.digitaleng.news/de/accuracy-and-checking-in-fea-part-1/

[29] Compact cylinders ADN. [Online]. https://www.festo.com/cat/pt_pt/products_ADN_AEN?CurrentIDCode1=ADN-16-10-I-P-A%20&CurrentPartNo=536227

[30] André Horstmann, "TVC acceleration factor - parameters," 2015.

[31] J. Arnold, N. Blattau, and C. and Hillman, "eliability testing of Ni-modified SnCu and SAC305 accelerated thermal cycling.," 2008.

H. Cui, 2005.

[32]

W. Engelmaier, "BGA and CGA solder attachments: Results of low-acceleration reliability
[33] tests and analysis,".

J. Mi, "hermal cycling life prediction of Sn-3.0Ag-0.5Cu solder joint using type-i censored
[34] data.," 2014.

Paulo Gordo, Sophie Duzellier, André Horstmann, and Tiago Frederico, "Technical Note 1
[35] - Review of Space Materials," 2015.

Paulo Gordo, Sophie Duzellier, André Horstmann, and Tiago Frederico, "Technical Note 2
[36] - Test Plans," 2015.

D.L., & Kelso, TS Oltrogge, "Getting to Know Our Space Population from the Public
[37] Catalog AAS 11-416, 2011," in *AAS/AIAA Astrodynamics Specialist Conference*, Girdwood, AK, 2011.

Paulo Gordo, Sophie Duzellier, André Horstmann, and Tiago Frederico, "Full proposal -
[38] Space Debris from Spacecraft Degradation Products," 2014.

Diana Pascoal, "Desenvolvimento e Validação do Sistema de Iluminação de Luz
[39] Ultravioleta (UV e VUV) da Infraestrutura de Simulação de Deterioração de Coberturas de Satélites," 2016.

Appendix A – Surface temperature calculation

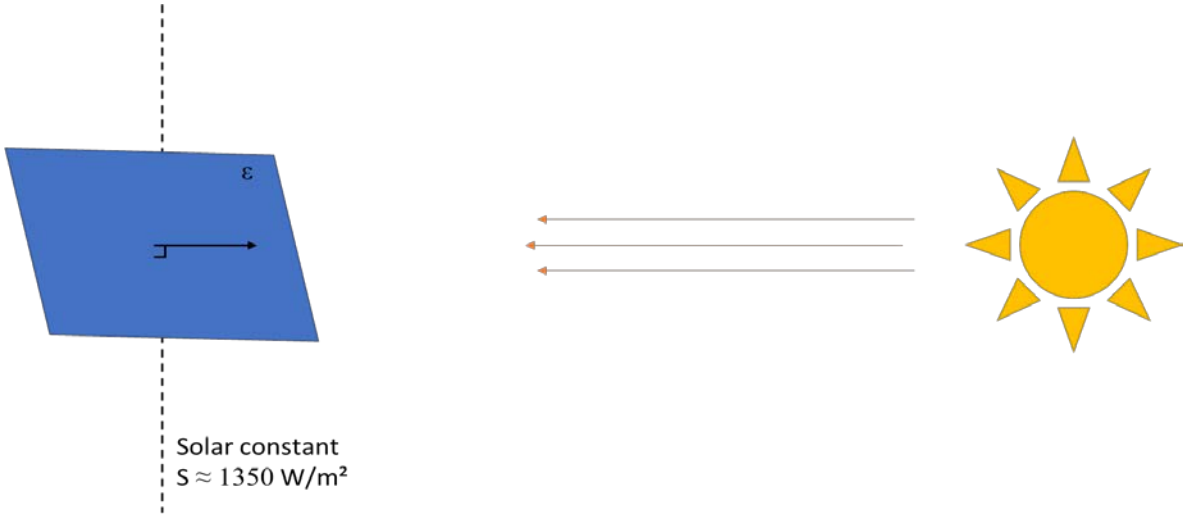

Figure A.1 – Schematic of the sun radiation on a perpendicular surface

At Earth's distance from the Sun, about 1350 watts of power in the form of electromagnetic radiation from the Sun fall on an area of one square meter. Where ε is the emissivity of the surface.

Total power absorbed: εS

Total power emitted: $\varepsilon\sigma T^4$

When we set the power absorbed and the power emitted equations equal to each other, we got:

$$\varepsilon S = \varepsilon\sigma T^4 \Leftrightarrow T = \sqrt[4]{\frac{S}{\sigma}} \cong 115\ °C$$

Appendix B – Linear Thermal Expansion

The change in the linear dimension can be estimated to be:

$$\frac{\Delta L}{L} = \alpha_L \Delta T$$

where α_L linear expansion coefficient.

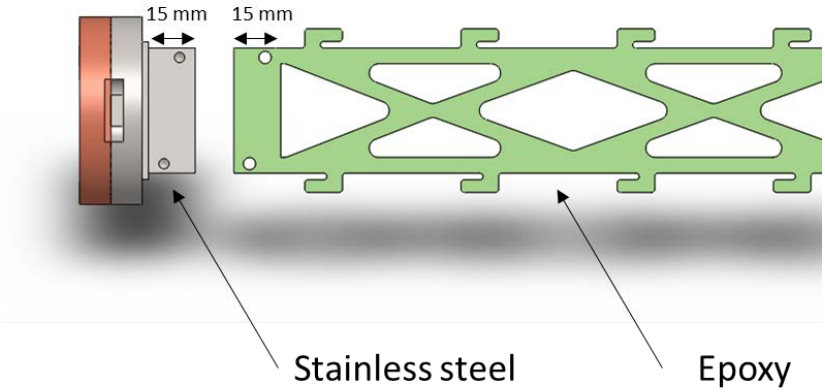

Figure B.1 – Exploded view

So, using $\alpha_L^{ST} = 1.8 \times 10^{-5}$ for the linear expansion of stainless steel and $\alpha_L^{Ep} = 3.0 \times 10^{-5}$ for the epoxy. Assuming a 300 °C of temperature range, it's is to calculate the linear expansion for each material. The expansion for the stainless steel is $\Delta L^{ST} = 81\ \mu m$ and for the epoxy $\Delta L^{Ep} = 135\ \mu m$.

Appendix C – Water Flow and Temperate Monitor

```
#define MaxTemp 35
#define AveTemp 30
#define AveFlow 2.5
#define Red 9
#define Yellow 8
#define Green 7
#include <math.h>

volatile float PullseFqy;
float FlowRate. Temp;
int ledState;

void start_Seq(){
  ledState = HIGH;

  for(int i=0;i<4;i++){
    digitalWrite(Red. ledState);
    digitalWrite(Yellow. ledState);
    digitalWrite(Green. ledState);
    delay(250);
    ledState=!ledState;
  }

  ledState = LOW;
  digitalWrite(Red. ledState);
  digitalWrite(Yellow. ledState);
  digitalWrite(Green. ledState);

}

double Thermistor(int RawADC) {
  /*
  (Ground) ---- (10k-Resistor) -------|------- (Thermistor) ---- (+5v)
                                     |
                                Analog Pin 0
   */
  double Temp;
  //Temp = log(10000.0*((1024.0/RawADC-1)));
Temp =log(10000.0/(1024.0/RawADC-1)); // for pull-up configuration
  Temp = 1 / (0.001129148 + (0.000234125 + (0.0000000876741 * Temp * Temp ))* Temp )-2;
  Temp = Temp - 273.15;            // Convert Kelvin to Celsius
  return Temp;
}

void rmp()
{
/*
 *   The circuit:
    Red pin of Water Flow Sensor connect to +5V
    Black pin of Water Flow Sensor connect to GND
    Yellow pin of Water Flow Sensor connect to D2(int.0)
 */

  PullseFqy ++ ;
}

void warning_ligths(float water_temp.float water_flow){
```

```
 if(water_flow > 0){
  if( water_temp < AveTemp){
   digitalWrite(Red. LOW);
   digitalWrite(Yellow. LOW);

  }
  else if(water_temp > AveTemp && water_temp < MaxTemp){
   digitalWrite(Red. LOW);
   digitalWrite(Yellow. HIGH);

  }
  else if(water_temp > MaxTemp){
   digitalWrite(Red. HIGH);
   digitalWrite(Yellow. LOW);

  }
 else if(water_temp > 37){
   digitalWrite(Red. ledState);
   digitalWrite(Yellow. !ledState);

  }
  if(water_flow > 2.4 && water_flow < 2.6)digitalWrite(Green. HIGH);
  else digitalWrite(Green. LOW);

 }
 else{

 digitalWrite(Red. ledState);
 digitalWrite(Yellow. ledState);
 digitalWrite(Green. ledState);
 }

ledState=!ledState;
}

void setup()
{
   Serial.begin(9600);
   attachInterrupt(0.rmp.RISING);
   pinMode(Red. OUTPUT);
   pinMode(Yellow. OUTPUT);
   pinMode(Green. OUTPUT);
   start_Seq();

}

void loop()
{
   PullseFqy = 0;
   delay(250); // Wait 1/4 second pulse frequency calculation
   FlowRate = 4*PullseFqy/73 ; // f = 73*Q. Q = L\MIN
   Temp=Thermistor(analogRead(0));
   Serial.print(FlowRate.2);
   Serial.print(";");
   Serial.println(Temp);

   warning_ligths(Temp.FlowRate);

}
```

Appendix D – Mechanical Drawing

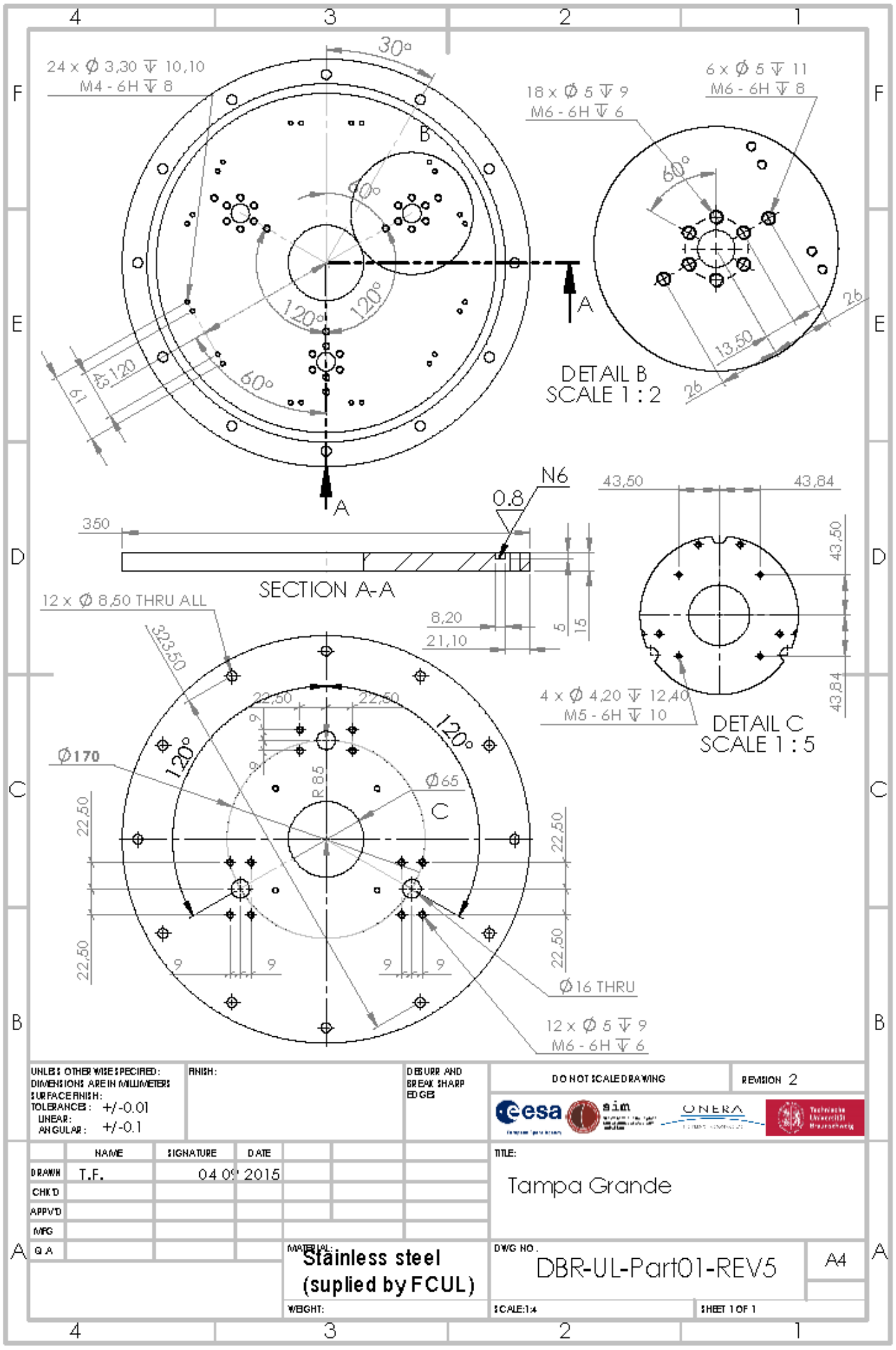
24 x Ø 3,30 ↧ 10,10
M4 - 6H ↧ 8
30°
18 x Ø 5 ↧ 9
M6 - 6H ↧ 6
6 x Ø 5 ↧ 11
M6 - 6H ↧ 8
60°
90°
120°
120°
120°
43,120
61
26
13,50
26
DETAIL B
SCALE 1 : 2
A
B
N6
0.8
350
SECTION A-A
43,50
43,84
43,50
43,84
12 x Ø 8,50 THRU ALL
8,20
21,10
5
15
4 x Ø 4,20 ↧ 12,40
M5 - 6H ↧ 10
DETAIL C
SCALE 1 : 5
323,50
22,50
22,50
9
9
120°
120°
Ø170
R 85
Ø65
C
22,50
22,50
22,50
22,50
9
9
9
9
Ø16 THRU
12 x Ø 5 ↧ 9
M6 - 6H ↧ 6
UNLESS OTHERWISE SPECIFIED:
DIMENSIONS ARE IN MILLIMETERS
SURFACE FINISH:
TOLERANCES: LINEAR: +/-0.01
ANGULAR: +/-0.1
FINISH:
DEBURR AND BREAK SHARP EDGES
DO NOT SCALE DRAWING
REVISION 2
NAME
SIGNATURE
DATE
DRAWN T.F. 04 09 2015
CHK'D
APPV'D
MFG
Q.A
TITLE:
Tampa Grande
MATERIAL:
Stainless steel
(suplied by FCUL)
DWG NO.
DBR-UL-Part01-REV5
A4
WEIGHT:
SCALE:1:4
SHEET 1 OF 1

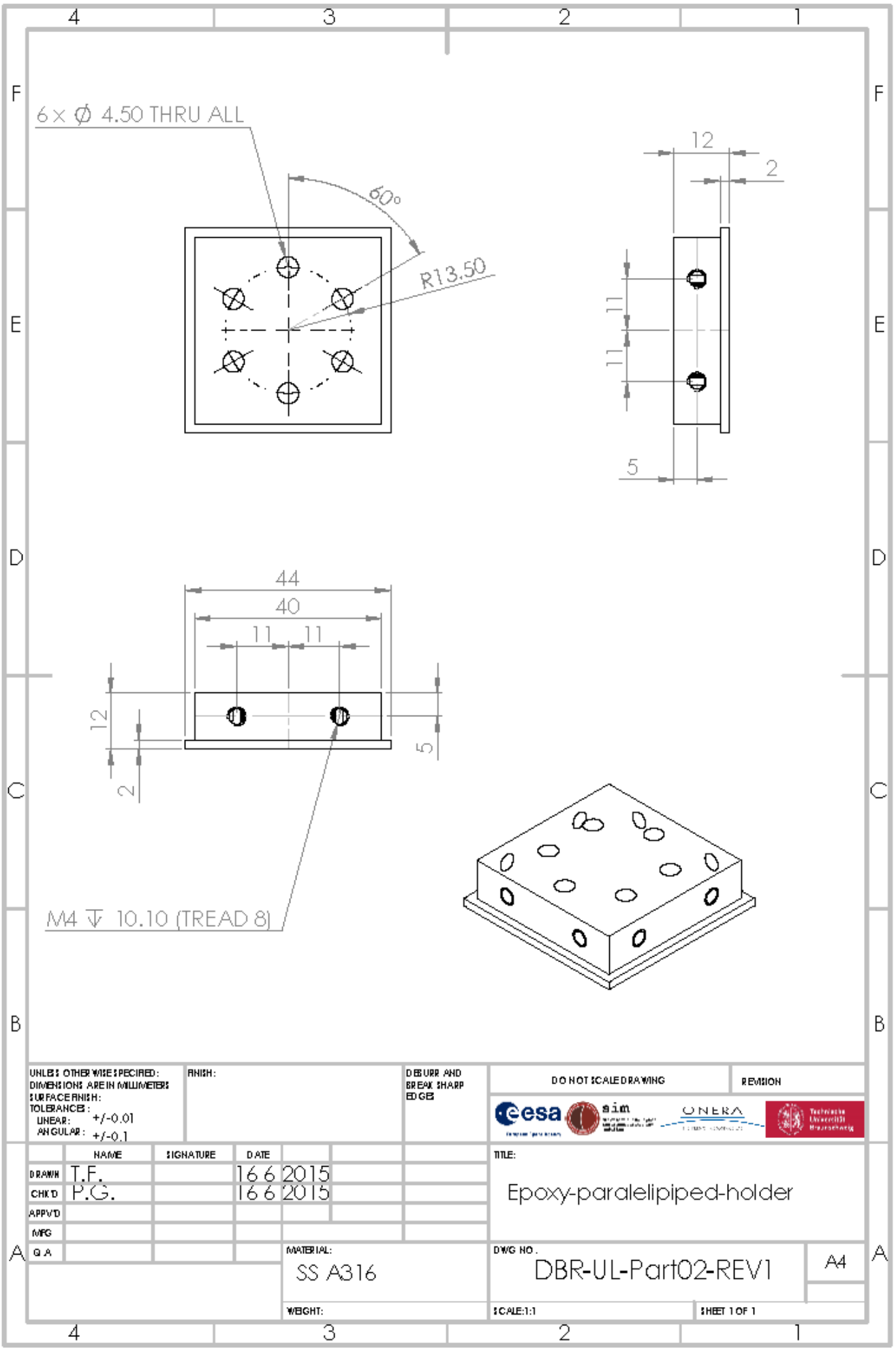
6 x Ø 4.50 THRU ALL
60°
R13.50
12
2
11
11
5
44
40
11
11
12
2
5
M4 ↧ 10.10 (TREAD 8)
UNLESS OTHERWISE SPECIFIED:
DIMENSIONS ARE IN MILLIMETERS
SURFACE FINISH:
TOLERANCES:
LINEAR: +/-0.01
ANGULAR: +/-0.1
FINISH:
DEBURR AND BREAK SHARP EDGES
DO NOT SCALE DRAWING
REVISION
NAME
SIGNATURE
DATE
DRAWN T.F. 16 6 2015
CHK'D P.G. 16 6 2015
APPV'D
MFG
Q.A
TITLE:
Epoxy-paralelipiped-holder
MATERIAL:
SS A316
DWG NO.
DBR-UL-Part02-REV1
A4
WEIGHT:
SCALE:1:1
SHEET 1 OF 1

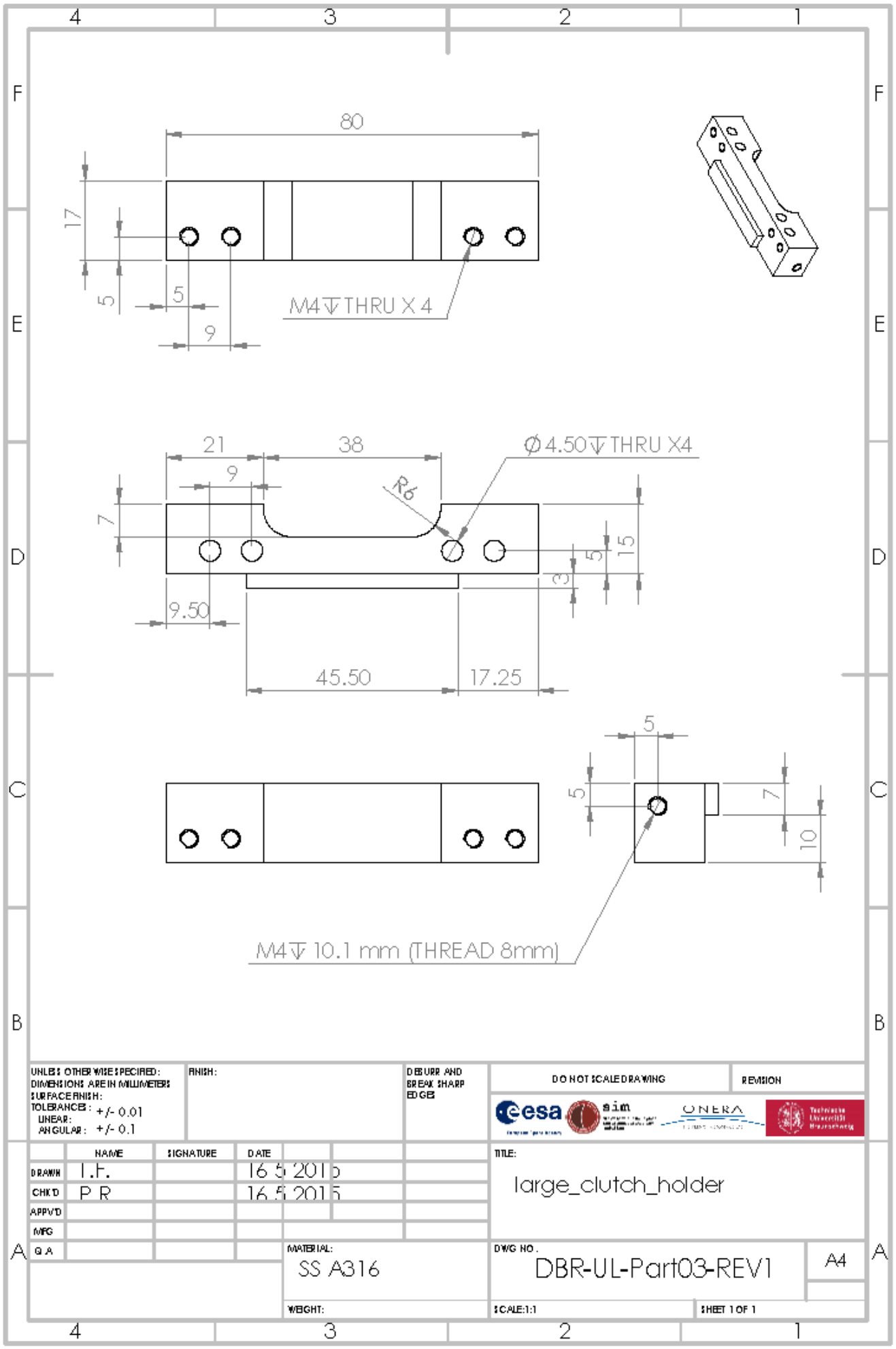
80
17
5
5
9
M4 ↧ THRU X 4
21
38
9
R6
Ø 4.50 ↧ THRU X4
7
5
15
3
9.50
45.50
17.25
5
5
7
10
M4 ↧ 10.1 mm (THREAD 8mm)
UNLESS OTHERWISE SPECIFIED:
DIMENSIONS ARE IN MILLIMETERS
SURFACE FINISH:
TOLERANCES: LINEAR: +/- 0.01
ANGULAR: +/- 0.1
FINISH:
DEBURR AND BREAK SHARP EDGES
DO NOT SCALE DRAWING
REVISION
NAME
SIGNATURE
DATE
DRAWN I.F. 16 5 2016
CHK'D P R 16 5 2016
APPV'D
MFG
Q A
TITLE:
large_clutch_holder
MATERIAL:
SS A316
DWG NO.
DBR-UL-Part03-REV1
A4
WEIGHT:
SCALE:1:1
SHEET 1 OF 1

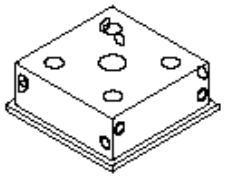

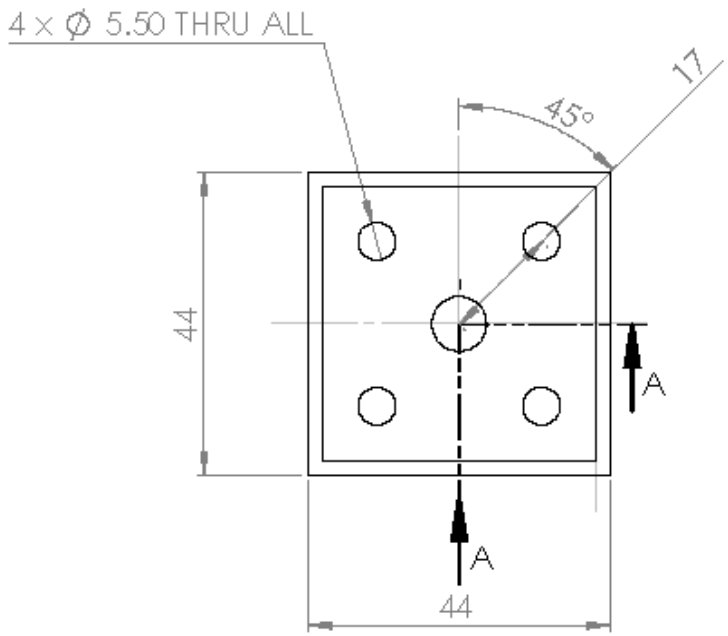

SECTION A-A

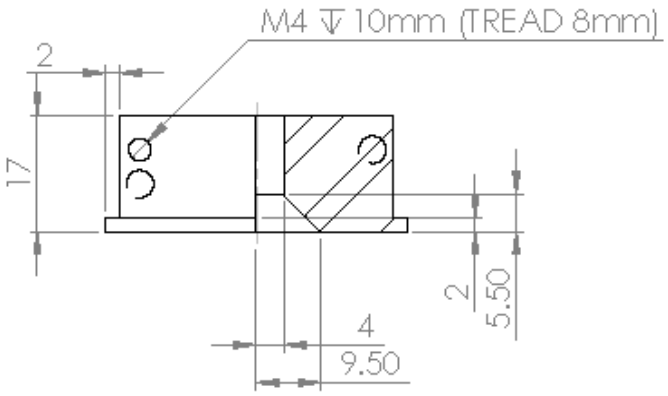

UNLESS OTHERWISE SPECIFIED: DIMENSIONS ARE IN MILLIMETERS SURFACE FINISH: TOLERANCES: LINEAR: +/- 0.01 ANGULAR: +/- 0.1	FINISH:		DEBURR AND BREAK SHARP EDGES	DO NOT SCALE DRAWING	REVISION
	NAME	SIGNATURE	DATE	TITLE:	
DRAWN	I.F.		16 6 2015	Epoxy-paralelipiped-holder2	
CHK'D	P.G.		16.6.2015		
APPV'D					
MFG					
Q.A					
	MATERIAL: SS A316			DWG NO. DBR-UL-Part05-REV1	A4
	WEIGHT:			SCALE:1:1	SHEET 1 OF 1

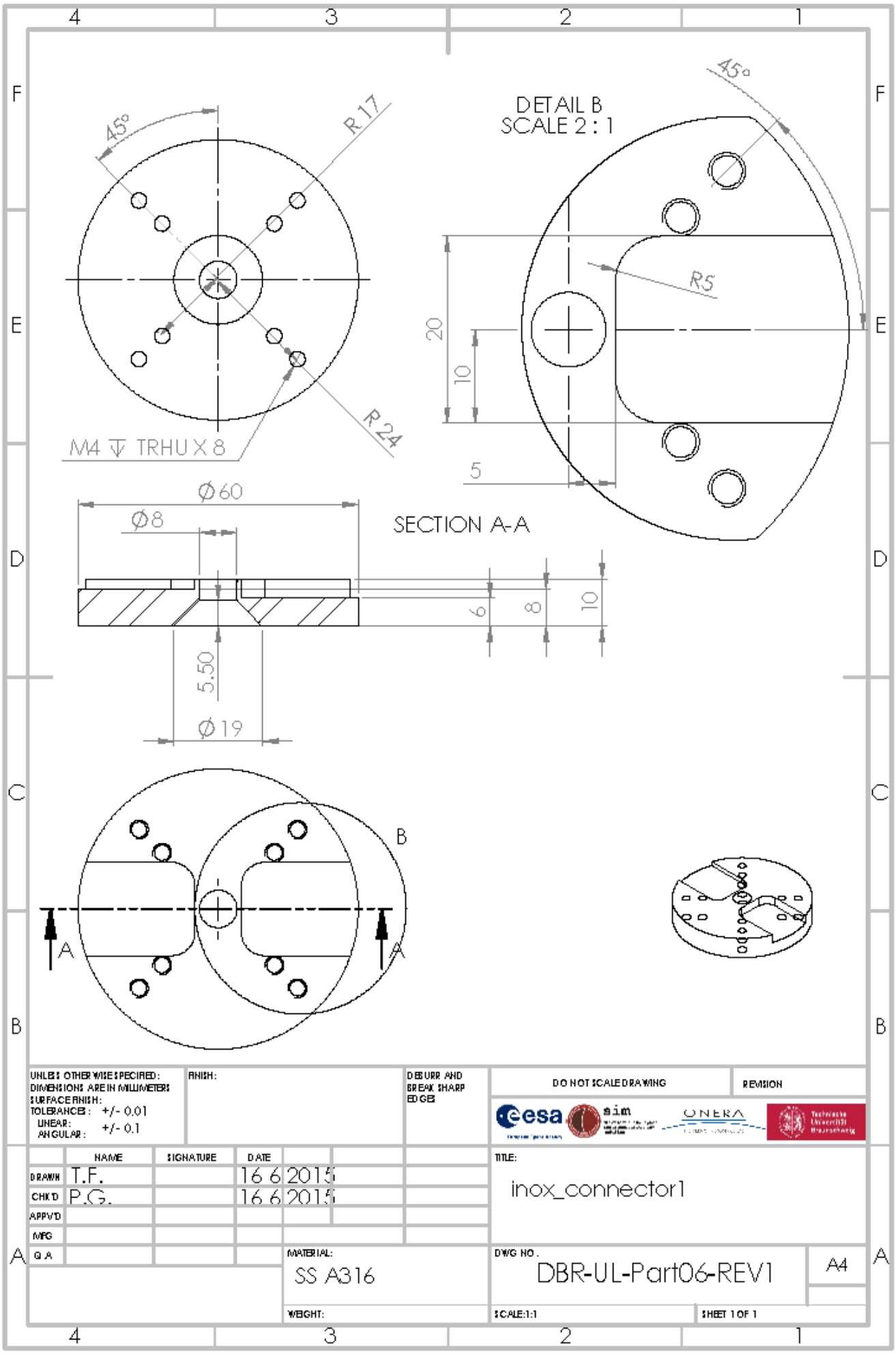

UNLESS OTHERWISE SPECIFIED: DIMENSIONS ARE IN MILLIMETERS SURFACE FINISH: TOLERANCES: LINEAR: +/- 0.01 ANGULAR: +/- 0.1	FINISH:	DEBURR AND BREAK SHARP EDGES	DO NOT SCALE DRAWING / REVISION

	NAME	SIGNATURE	DATE
DRAWN	T.F.		16 6 2015
CHK'D	P.G.		16 6 2015
APPV'D			
MFG			
Q.A			

TITLE: inox_connector1

MATERIAL: SS A316

DWG NO. DBR-UL-Part06-REV1

A4

WEIGHT:

SCALE:1:1

SHEET 1 OF 1

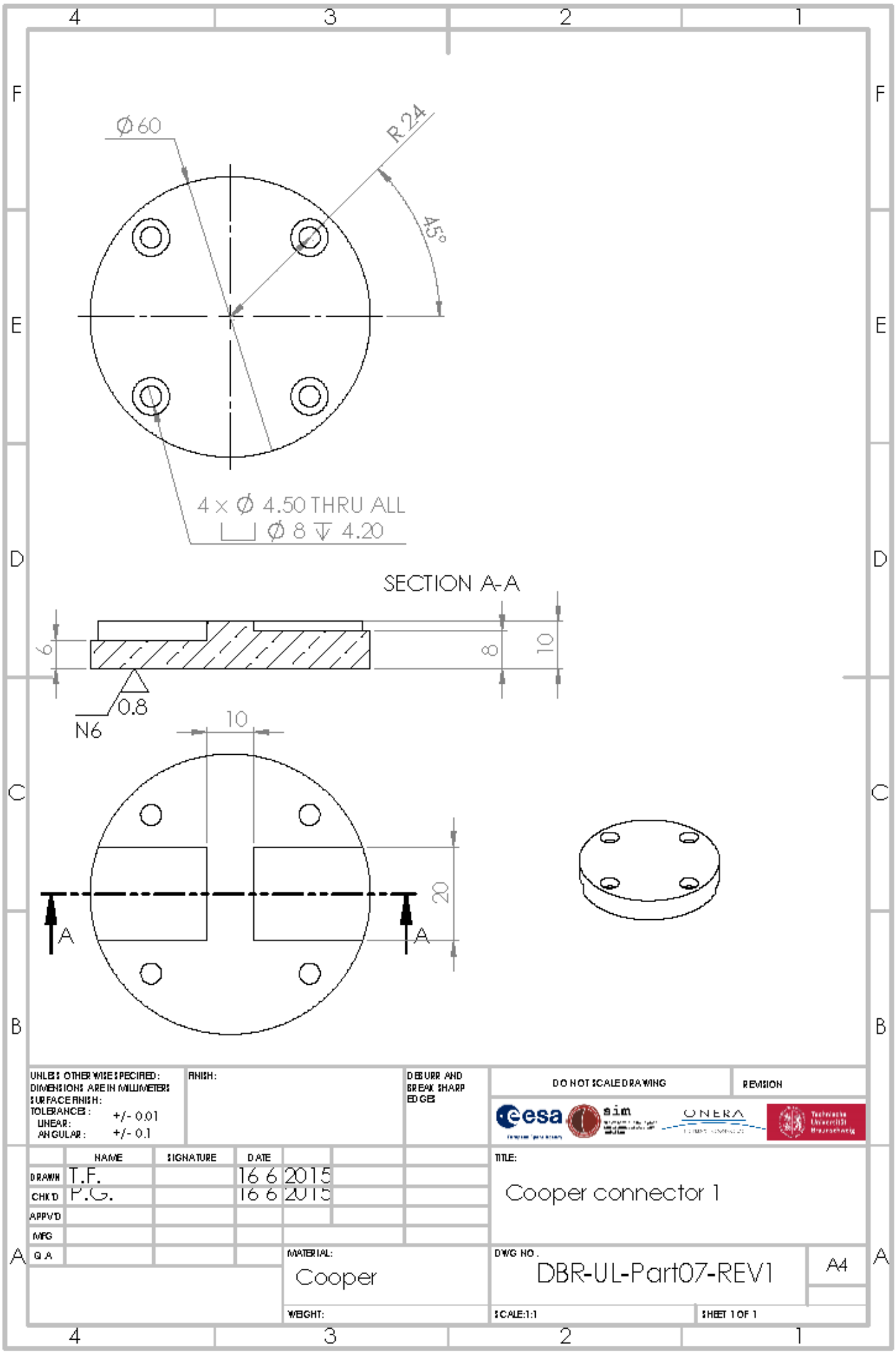

UNLESS OTHERWISE SPECIFIED: DIMENSIONS ARE IN MILLIMETERS SURFACE FINISH: TOLERANCES: LINEAR: +/- 0.01 ANGULAR: +/- 0.1	FINISH:
DEBURR AND BREAK SHARP EDGES	DO NOT SCALE DRAWING
REVISION	

	NAME	SIGNATURE	DATE
DRAWN	T.F.		16 6 2015
CHK'D	P.G.		16 6 2015
APPV'D			
MFG			
Q.A			

TITLE: Cooper connector 1

MATERIAL: Cooper

DWG NO. DBR-UL-Part07-REV1

A4

WEIGHT:

SCALE:1:1

SHEET 1 OF 1

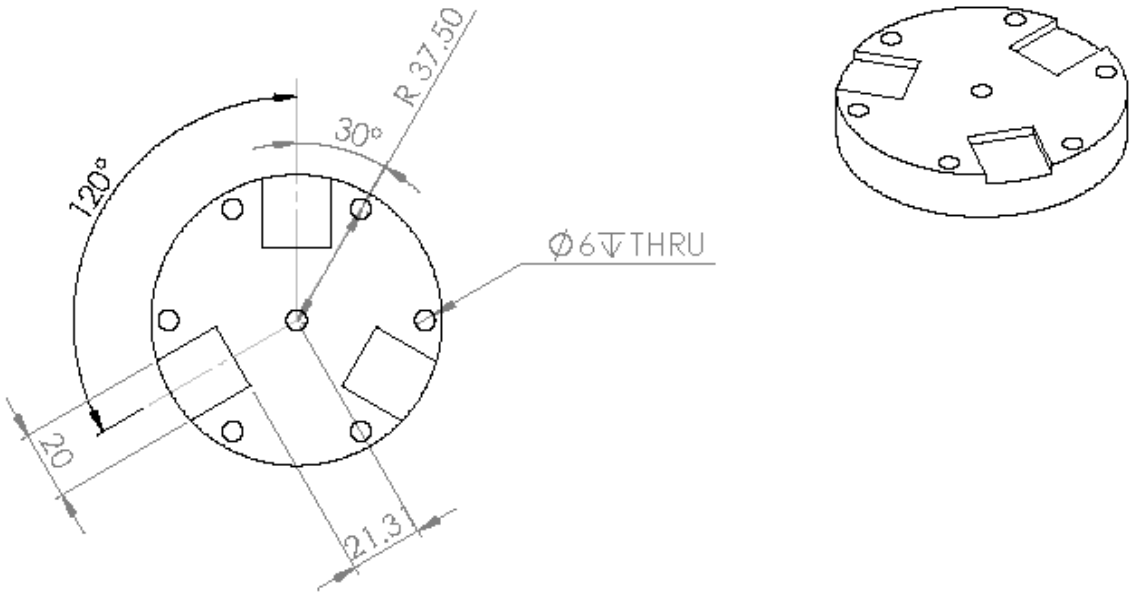

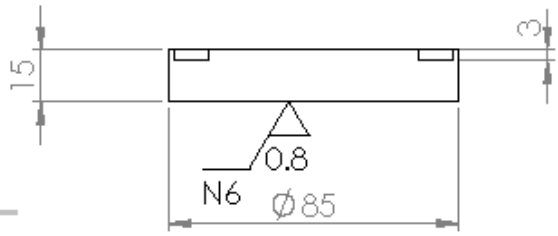

UNLESS OTHERWISE SPECIFIED: DIMENSIONS ARE IN MILLIMETERS SURFACE FINISH: TOLERANCES: LINEAR: +/- 0.01 ANGULAR: +/- 0.1	FINISH:		DEBURR AND BREAK SHARP EDGES	DO NOT SCALE DRAWING		REVISION
	NAME	SIGNATURE	DATE	TITLE:		
DRAWN	T.F.		16.6.2015	FINGER_COUPLE		
CHK'D	P.G.		16.6.2015			
APPV'D						
MFG						
Q.A						
			MATERIAL: Cooper	DWG NO. DBR-UL-Part08-REV1		A4
			WEIGHT:	SCALE:1:2	SHEET 1 OF 1	

Alteracao de peca:

A) alargameto de furo de passage (de 107 -> 153)

B) Adicional 8 furos M8

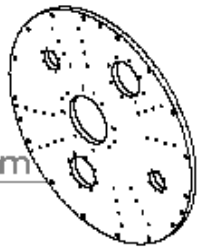

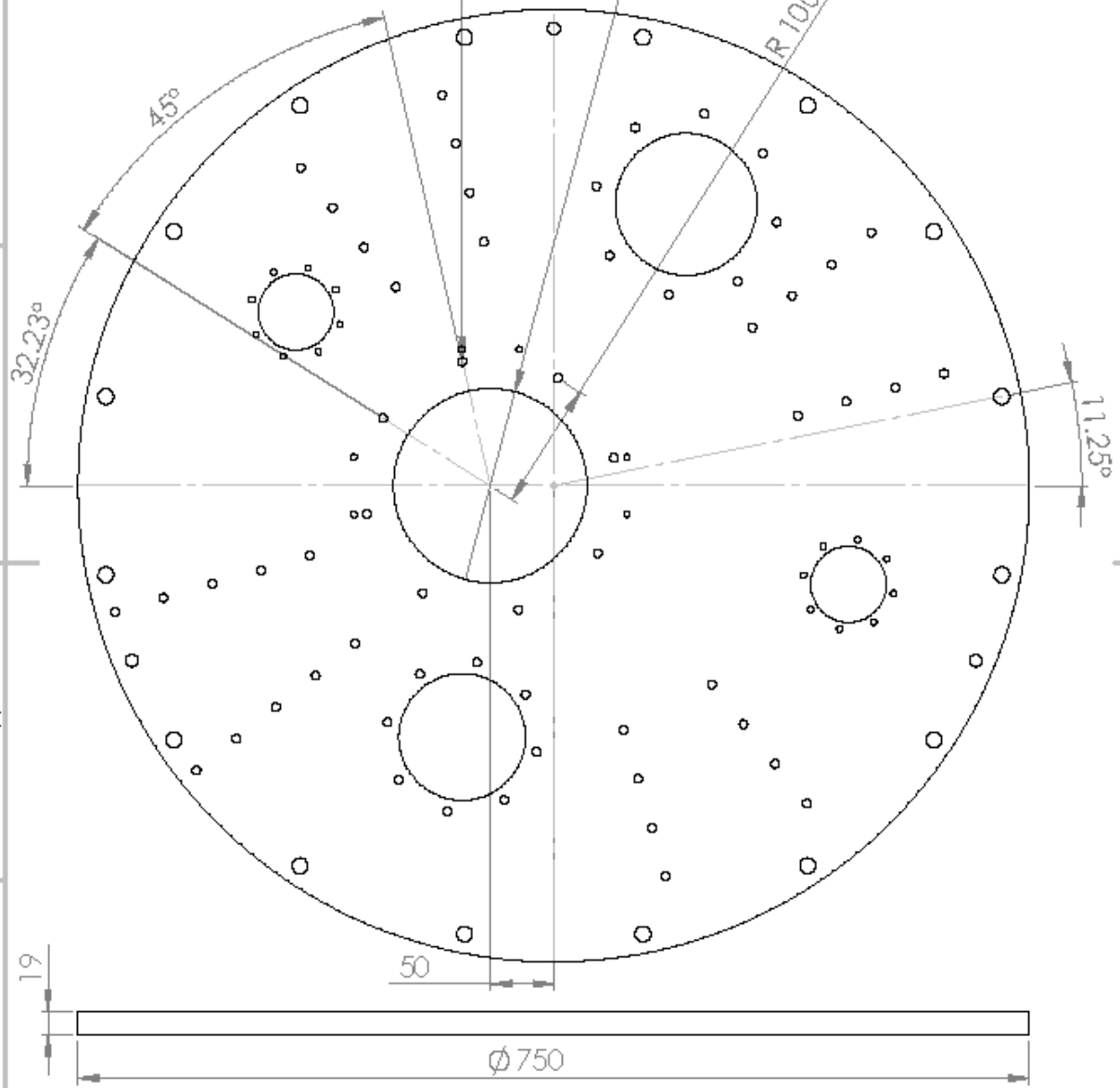

UNLESS OTHERWISE SPECIFIED: DIMENSIONS ARE IN MILLIMETERS SURFACE FINISH: TOLERANCES: LINEAR: +/- 0.01 ANGULAR: +/- 0.1	FINISH:	DEBURR AND BREAK SHARP EDGES	DO NOT SCALE DRAWING / REVISION

	NAME	SIGNATURE	DATE
DRAWN	P.G.	8 / 20	5
CHK'D			
APPV'D			
MFG			
Q.A			

TITLE:

Alteração de peca

Bottom flange

MATERIAL: SS A316	DWG NO. DBR-UL-Part15-REV1	A4
WEIGHT:	SCALE:1:20	SHEET 1 OF 1

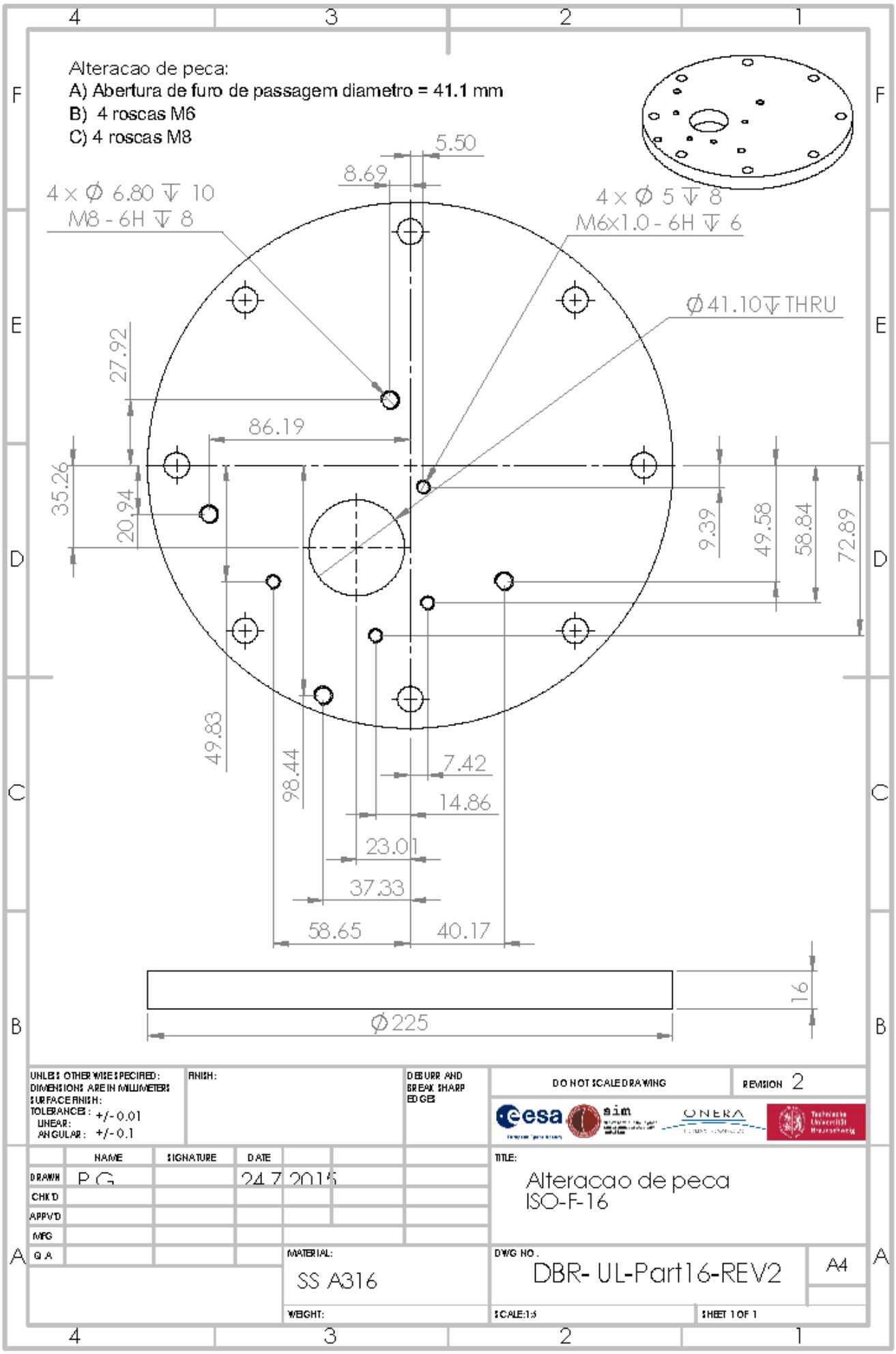
Alteracao de peca:
A) Abertura de furo de passagem diametro = 41.1 mm
B) 4 roscas M6
C) 4 roscas M8
5.50
8.69
4 x Ø 6.80 ↧ 10
M8 - 6H ↧ 8
4 x Ø 5 ↧ 8
M6x1.0 - 6H ↧ 6
Ø41.10↧THRU
27.92
86.19
35.26
20.94
9.39
49.58
58.84
72.89
49.83
98.44
7.42
14.86
23.01
37.33
58.65
40.17
16
Ø225
UNLESS OTHERWISE SPECIFIED:
DIMENSIONS ARE IN MILLIMETERS
SURFACE FINISH:
TOLERANCES:
LINEAR: +/- 0.01
ANGULAR: +/- 0.1
FINISH:
DEBURR AND BREAK SHARP EDGES
DO NOT SCALE DRAWING
REVISION 2
NAME
SIGNATURE
DATE
DRAWN P G 24.7.2014
CHK'D
APPV'D
MFG
Q.A
MATERIAL:
SS A316
WEIGHT:
TITLE:
Alteracao de peca
ISO-F-16
DWG NO.
DBR- UL-Part16-REV2
A4
SCALE:1:5
SHEET 1 OF 1

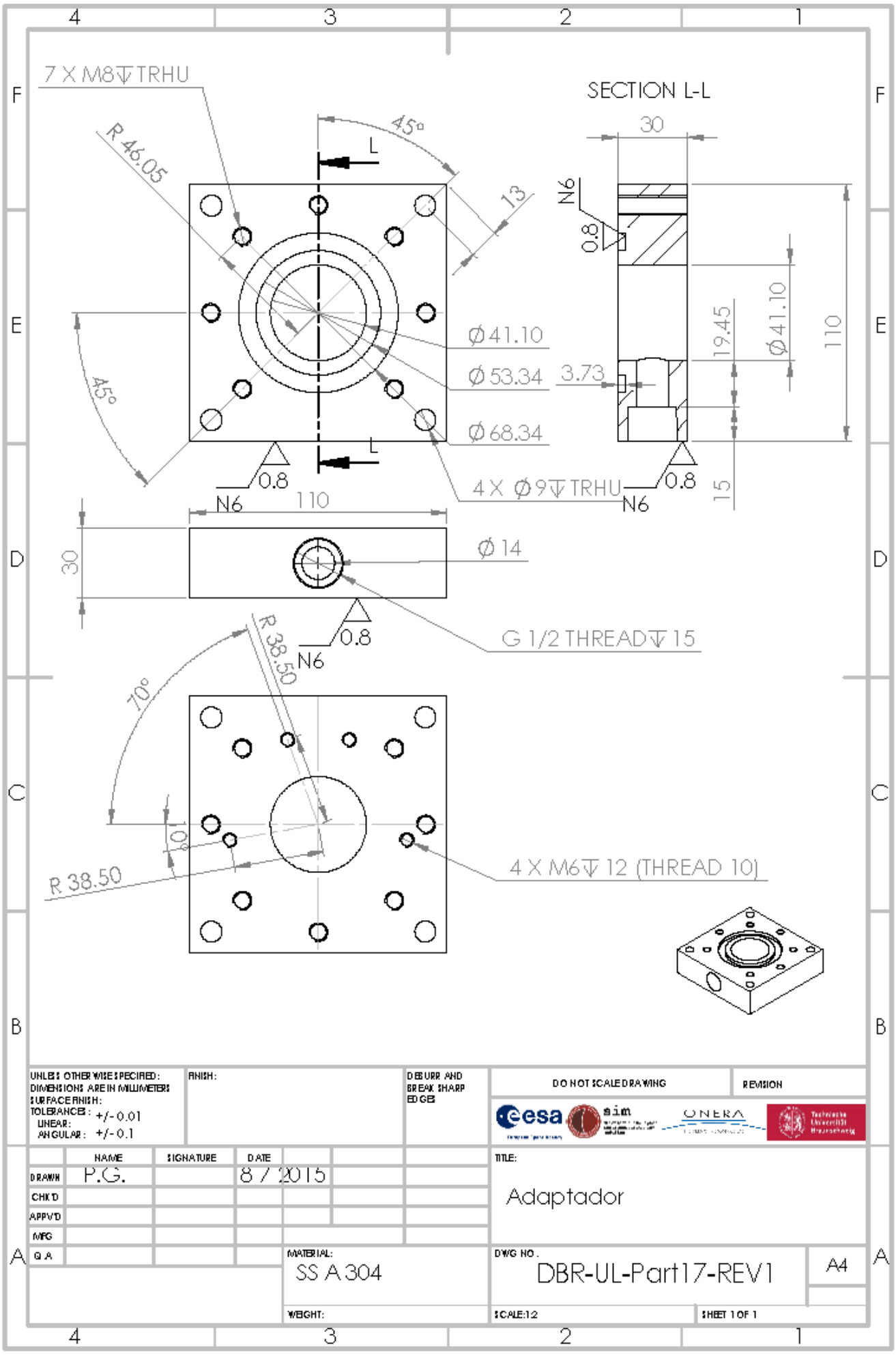
7 X M8↧TRHU
R 46.05
45°
L
13
SECTION L-L
30
N6
0.8
Ø41.10
Ø53.34
Ø68.34
3.73
19.45
Ø41.10
110
45°
4 X Ø9↧TRHU
0.8
N6
15
N6
110
30
Ø14
0.8
N6
G 1/2 THREAD↧15
R 38.50
70°
10
R 38.50
4 X M6↧12 (THREAD 10)
UNLESS OTHERWISE SPECIFIED:
DIMENSIONS ARE IN MILLIMETERS
SURFACE FINISH:
TOLERANCES: +/- 0.01
LINEAR:
ANGULAR: +/- 0.1
FINISH:
DEBURR AND BREAK SHARP EDGES
DO NOT SCALE DRAWING
REVISION
esa
sim
ONERA
NAME
SIGNATURE
DATE
DRAWN
P.G.
8 / 2015
CHK'D
APPV'D
MFG
Q.A
TITLE:
Adaptador
MATERIAL:
SS A 304
DWG NO.
DBR-UL-Part17-REV1
A4
WEIGHT:
SCALE:1:2
SHEET 1 OF 1

Appendix F – LabVIEW Block Diagrams

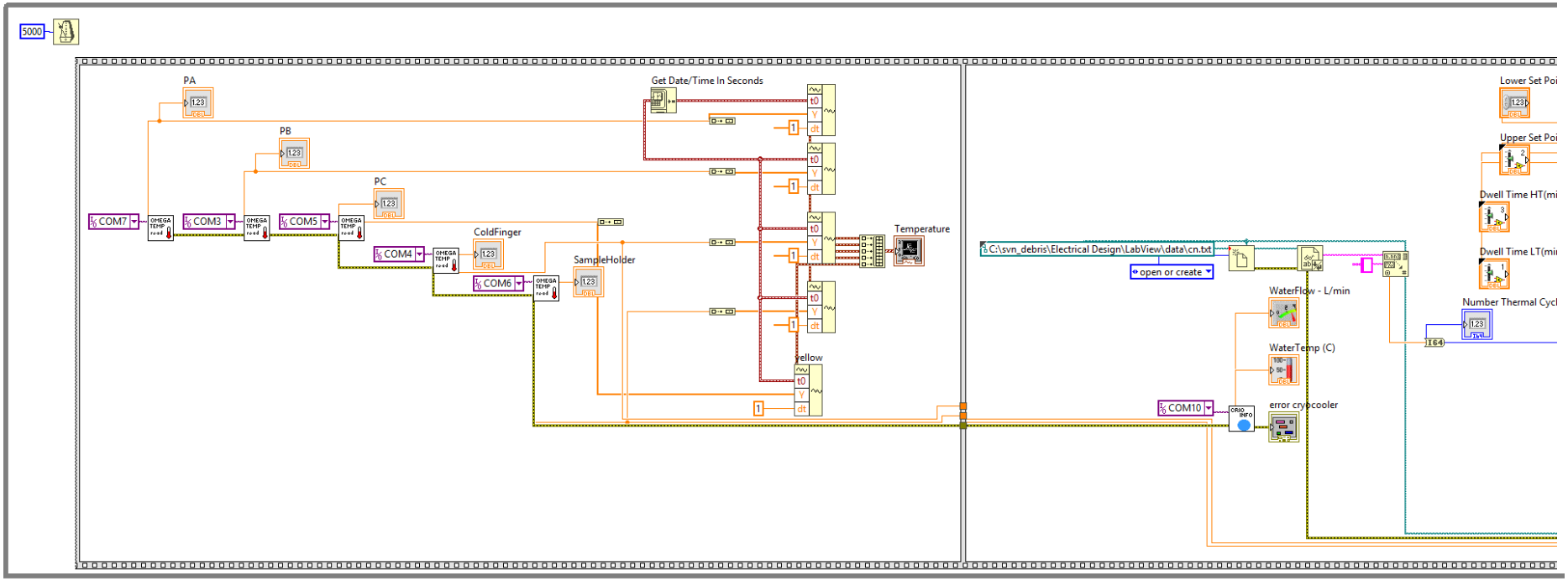
5000
PA
PB
PC
COM7
COM3
COM5
COM4
COM6
ColdFinger
SampleHolder
Get Date/Time In Seconds
Temperature
yellow
C:\svn_debris\Electrical Design\LabView\data\cn.txt
open or create
WaterFlow - L/min
WaterTemp (C)
COM10
error cryocooler
Lower Set Poi
Upper Set Poi
Dwell Time HT(mi
Dwell Time LT(mi
Number Thermal Cycl

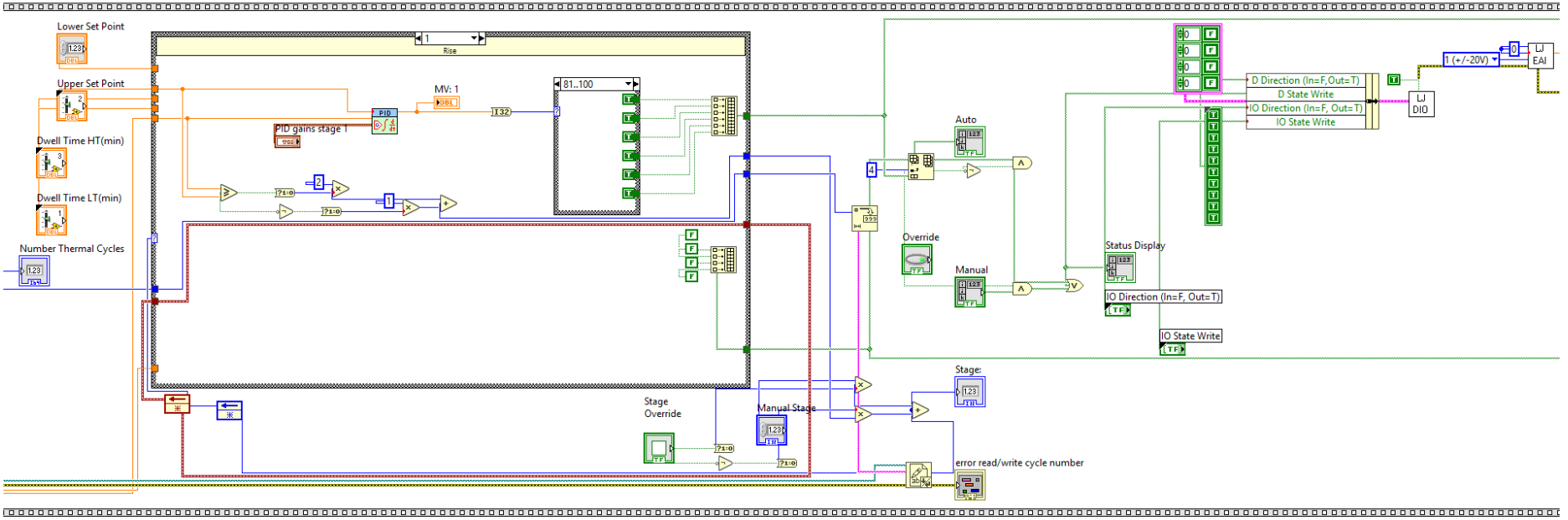
Lower Set Point
Upper Set Point
Dwell Time HT(min)
Dwell Time LT(min)
Number Thermal Cycles
Rise
PID gains stage 1
MV: 1
81..100
Auto
Override
Manual
Stage Override
Manual Stage
Stage:
error read/write cycle number
Status Display
IO Direction (In=F, Out=T)
IO State Write
D Direction (In=F,Out=T)
D State Write
LJ DIO
1 (+/-20V)
LJ EAI

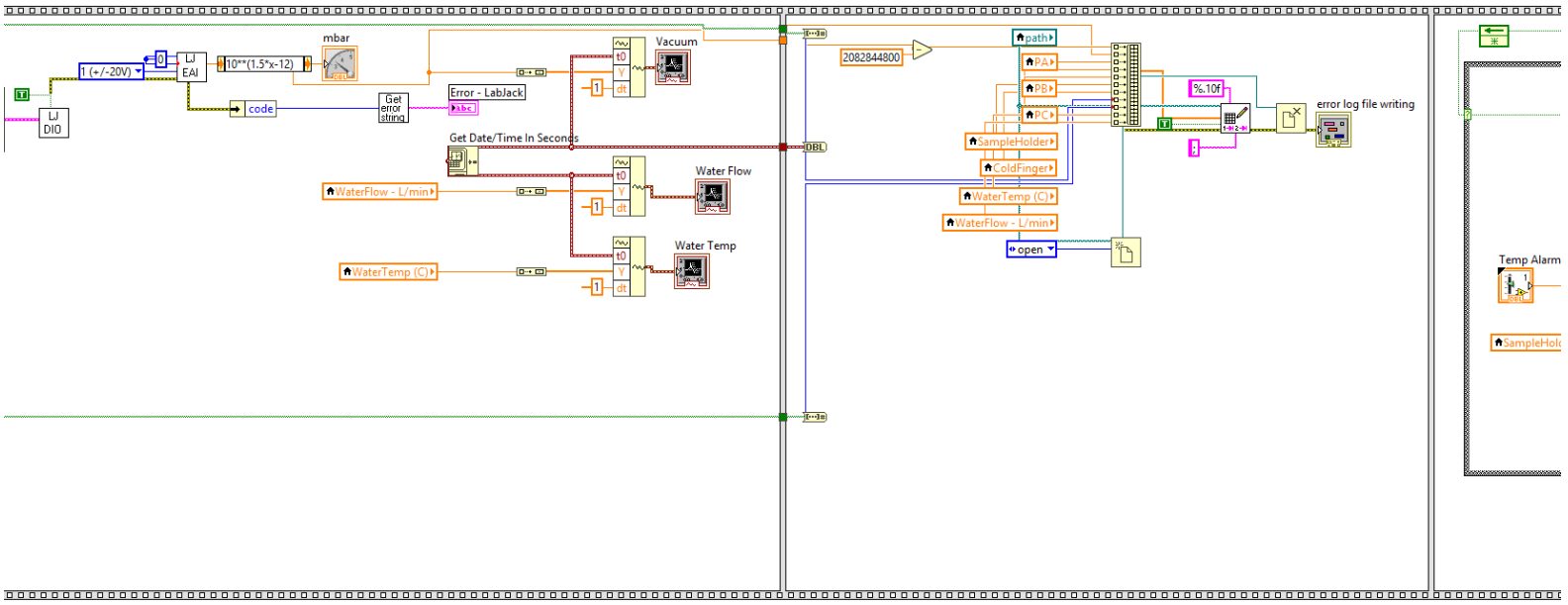
mbar
1 (+/-20V)
LJ EAI
10**(1.5*x-12)
code
LJ DIO
Get error string
Error - LabJack
Vacuum
Get Date/Time In Seconds
Water Flow
WaterFlow - L/min
Water Temp
WaterTemp (C)
2082844800
path
PA
PB
PC
SampleHolder
ColdFinger
WaterTemp (C)
WaterFlow - L/min
open
%.10f
error log file writing
DBL
Temp Alarm

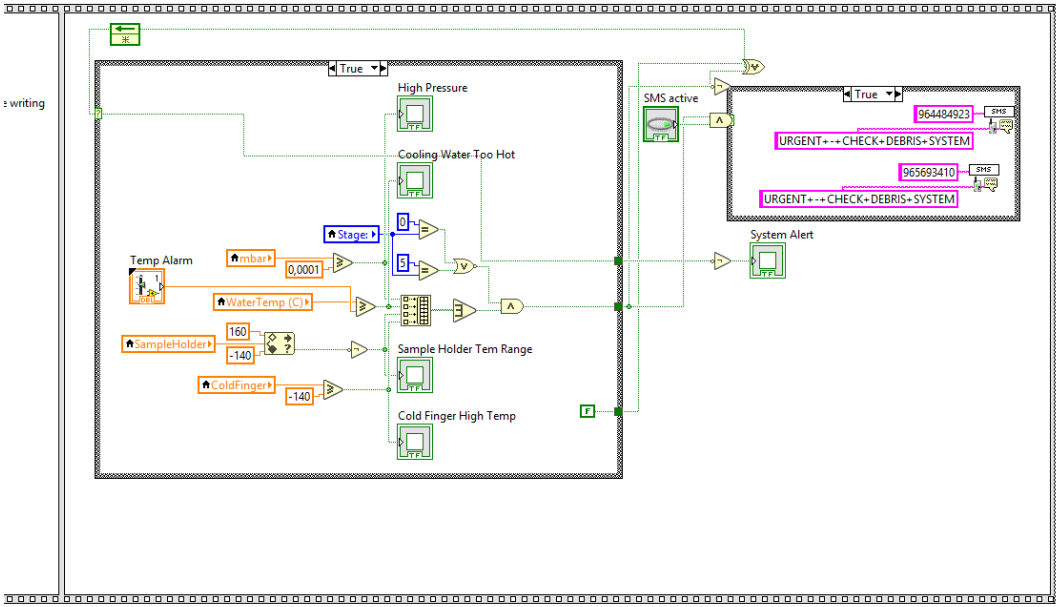
True
High Pressure
Cooling Water Too Hot
Stage:
Temp Alarm
mbar
0,0001
WaterTemp (C)
SampleHolder
160
-140
Sample Holder Tem Range
ColdFinger
-140
Cold Finger High Temp
SMS active
True
964484923
URGENT+-+CHECK+DEBRIS+SYSTEM
965693410
URGENT+-+CHECK+DEBRIS+SYSTEM
System Alert